Geophysics and geomatics methods for coastal monitoring and hazard evaluation

By: Emanuele Colica

Tutor: Prof. Sebastiano D'Amico

A thesis presented to the Department of Geosciences at the University of Malta in Fulfilment of the Requirements for the Degree of Doctor of Philosophy

2022

Abstract

The Maltese archipelago's northern region is experiencing a massive lateral spreading landslide. The region is distinguished by a coastal cliff environment with a hard coralline limestone outcropping layer sitting on a thick layer of clay. This geological formation causes coastal instability that results in rockfall and lateral spreading. This research has developed a methodology for high-precision monitoring of coastal cliff erosion using the integration of geomatics and geophysical techniques. From novel data collected by unmanned aerial vehicle (UAV) digital photogrammetry, a 3D digital model of the Selmun promontory was reconstructed and used to map and measure important geological features such as fractures, joints, and large boulders. Then, geophysical techniques such as electrical resistivity tomography and ground penetrating radar have been used for the identification and mapping of vertical fractures affecting the hard coralline limestone plateau and to validate the 3D geological model. In addition to this, high-precision orthophotos from UAV have been compared with aerial and satellite images captured between 1957 and 2021 and have been georeferenced into a GIS. The movement of boulders and cracks in rocks was then vectorised to highlight and quantify movement in time. The resulting data are then used to derive a qualitative assessment of the coastal variations in the geometric properties of the exposed discontinuity surfaces, to evaluate the volumes and the stop points of the observed rockfalls. Subsequently, a quantitative analysis was carried out through the use of the numerical simulation software RocPro 3D to reproduce the paths followed by the blocks and estimate different values such as speed, energy and stop points of the fallen blocks. Consequently, the source areas of past events were identified as well as potential source areas to simulate future events of unstable blocks on the cliff. The outcomes of this research were finally implemented in a GIS to offer a new approach for the collection and processing of coastal monitoring data which, ultimately, drives the local authorities to address social, economic and environmental issues of pressing importance and facilitates effective planning and mitigation of risks.

Contents

1. Introduction

In recent years, in-depth studies on the impact of coastal erosion have been closely linked to those determined by the scenarios hypothesized for climate change, which predict an extremity of natural events and a rise in sea level. These elements can work in "synergy" with erosion caused by anthropogenic causes. The coastal area, worldwide and especially in the Mediterranean area, is in itself an economic resource, as it represents the area with the highest density of settlements and human activities. The Maltese coast, the subject of this research, is a natural tourist destination that attracts many tourists to the islands and this leads to intense urbanization along these areas. Since the 1970s, in Malta, there has been an increase in coastal urban settlements, increasing the importance of the tourism sector, which thus becomes the pillar of the economy of the Maltese islands. It is essential to balance the promotion of tourism activities together with the defence of the cultural, historical and naturalistic heritage of the Maltese archipelago, and to remedy this, a set of multidisciplinary activities may be undertaken. These activities in the fields of engineering, geology, history and archaeology harmonize with each other to obtain techniques and procedures that help to achieve a balance between cultural and natural heritage (Magri et al., 2008).

Overall, the vulnerable assets in coastal areas are represented by protected areas or areas of high naturalistic value, infrastructures (often strategic like roads or industrial settlements), urban settlements, sites of cultural interest and economic activities related to tourism, from fish farms, often placed in transition environments whose particular characteristics can be put in crisis by coastal erosion.

The research on the coastal areas, of the Maltese archipelago and not only, is lacking and deserves more attention in view of the characteristics that make it individual environments. The geological context, the coastal configuration and the exposure to weathering phenomena are important components in the behaviour of the erosional processes.

Landslides and rockfalls affecting the high coasts present a significant geohazard and are generally classified into a range of landslide mechanisms, including translational and block sliding, rotational, rock toppling, lateral spreading, debris flow, etc. (see appendix I). The overlapping of rock strata with varying geomechanics properties and erosion characteristics is the common cause of several of these types of mechanisms (Gigli et

al., 2012; Galea et al., 2014). A rockfall is a type of fast-moving landslide that happens when a rock falls, bounces, or rolls freely from a cliff face or down a very steep slope and it is commonly triggered by severe rainfalls or earthquakes. In order to assess the danger due to these formations, and to prevent any human and economic losses, it is essential to understand the trigger mechanisms. For this reason, it is crucial to study these phenomena in areas increasingly exposed to heavy rainfall due to climate change and subject to seismic hazards such as the central Mediterranean (D'Amico et al., 2013). One of the main consequences due to the action of weathering on rock cliffs is rockfall fragmentation, which is the process by which the detached mass loses its integrity while falling from a steep slope and breaks up into smaller pieces (Corominas et al. 2017), i.e., a limited number of blocks, with volumes up to a few hundred thousand cubic metres, move downstream with little mutual interaction (Evans et al. 1993; Ruiz-Carulla et al. 2017).

This type of landslide is quite unpredictable and pose a significant threat to human lives and properties. Further studies related to the assessment and mapping of landslide hazards, as well as their vulnerability to seismic shaking, have been conducted by Jongmans et al., 2007; Vessia et al., 2013; Günther et al. 2013; Van Westen et al., 2008; Guzzetti et al., 1999).

In the last decade, along the north-western coast of the Island of Malta, in order to investigate the slow-moving coastal landslide, have been performed long-term GPS observations, over a 4.5-year period, and were installed two fissurometers to identify the displacement of the blocks (Mantovani et al. 2013). More recently, other results deriving from advanced Synthetic Aperture Radar (SAR) interferometric analysis made it possible to measure the speed (ranging from 1 to 7 mm/year) and trend of the deformations over a period of about 20 years (Mantovani et al. 2016).

In this thesis an area on the north-east coast of Malta will be investigated with an innovative multidisciplinary methodology which will examine a total period of 64 years in which several collapses have occurred.

1.1 Aim and objectives of the thesis

The geological and geomorphological characteristics of the Maltese archipelago expose the population to geological hazards, especially in the areas surrounding the cliffs subject to landslides. Therefore, to mitigate hazards, it is important to understand vulnerability and determine the dynamic properties of unstable cliffs. In this context, the value of this research is evident, which can be useful for outlining a methodology capable of monitoring and assessing hazards and which will make it possible to adopt adaptation policies capable of reducing coastal hazards. This research seeks to develop an integrated method, combining geophysics and geomatics techniques, aimed at monitoring and evaluating coastal hazards, such as cliff failures. To understand the extent and nature of the collapses, a detailed geomorphological mapping of the area will be reconstructed using geomatic techniques such as aerial drone photogrammetry (e.g. Jaboyedoff et al., 2012; Žabota et al., 2021).

Drone-based photogrammetry will be implemented in this study, to obtain textured three-dimensional models to allow detailed identification of the fractures in the rocky blocks of the cliffs. Then, geophysical investigations will provide useful information to identify not visible fractured areas contributing to landslides.

In rockfall prone areas, one of the most important tools for assessing the probability of rockfall events, the spatial probability and the intensity of impacts is numerical modelling (Agliardi et al., 2009; Sarro et al., 2014). In fact, in this thesis 3D simulations will be performed using the rockfall simulation software Rocpro 3D to predict the behaviour of unstable rocks and their trajectories. Furthermore, a series of geospatial datasets, captured by remote sensors and in situ measurements will be integrated into a Geographic Information System (GIS). The GIS will allow Maltese authorities to better address social, economic and environmental issues of pressing importance.

The following aim and objectives (Table 1) have directed the research:

- (Aim) Develop a reliable and integrated methodology using Geomatics and Geophysics techniques for high-precision monitoring of cliffs.

Table 1: *Description of research objectives.*

Objective	Description
1	3D digital model of study area
2	Identification and mapping of vertical fractures with geophysical techniques
3	Monitoring rock blocks displacements and quantification of volumes
4	Rockfall simulation and trajectories estimation
5	Implementation of a GIS containing all collected datasets and results

2. Location and geological setting of the Maltese archipelago

The Maltese archipelago, made up of the islands of Malta, Gozo, Comino, Cominotto and Filfla, is located in the Sicilian Channel and has a total area of approximately 316 km^2. It is connected to Sicily through a shallow depth area called "The Malta Plateau" (Pedley et al., 2002) (Fig. 1). The Maltese islands are placed in the shallow depths of the central Mediterranean on a plateau known as the "Pelagian platform" at about 90 km south of Sicily and 290 km northeast of Tunisia.

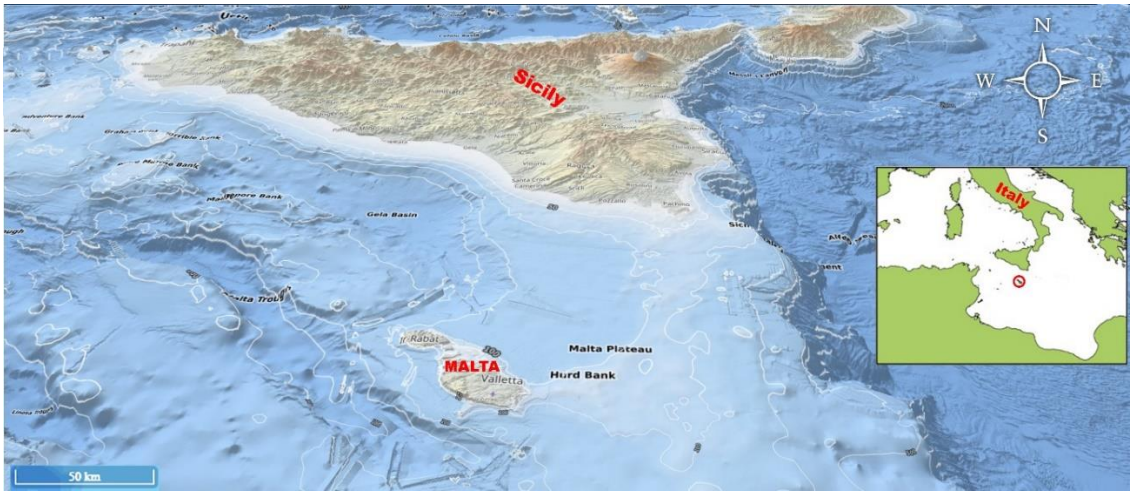

Figure 1: *3D view of the Maltese archipelago and the bathymetry that surrounds it. (Derived product from the GEBCO 2020 Grid). The position of the Maltese islands within the central Mediterranean is shown in the red circle in the inset on the right.*

During the Oligocene and Miocene eras, continuous pressures from tectonic plates originated the separation process of the European continent from the African continent, and consequently, the 'Pelagian Platform' remained covered by waters below the shallow sea.

The Maltese archipelago, as we can see in fig. 2, was quite remote from the rest of the continents. Researchers have observed the different origins of the seabed deposits in this archipelago, highlighting that they have not been obtained from the land of the continents but directly from the sea (Pedley et al., 1976; Felix, 1973). Having said that, the seabed is mainly constituted by remains of flora and fauna which lived under the sea. Thus, the sediments on the Maltese islands have a high percentage of lime, as a consequence of the strong presence of calcium carbonate cumulated on the seabed during the geological epochs. Calcium carbonate can be found in fragments of seashells and for this reason, the islands are full of this element, given that the seabed is formed mainly of remains of animals and plants that lived under the sea. According to the depth of the sea in the period in which the sediments are deposited, a different composition of each layer is obtained, also considering the granulometry and stratification (Pedley et al., 2002). The structure of the underlying layers massively determined the description of the land of the Maltese islands.

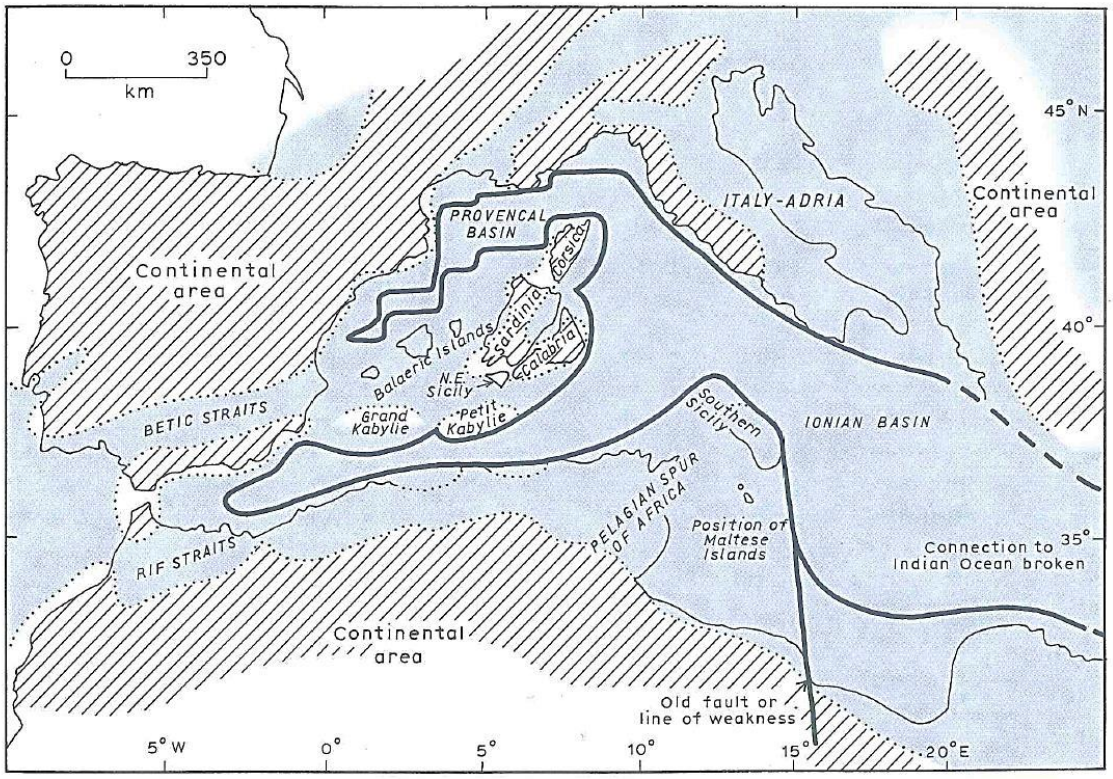

Figure 2: *Between 30 and 5 million years ago, continuous tectonic stresses separated Europe from Africa, and the Maltese archipelago moved away from the rest of the continent (Pedley et al., 2002).*

2.1 Geology of the Maltese islands

The rocky sequence of which the Maltese archipelago is formed consists of five overlapping geological formations laid on top of each other. In some areas, because of the uplift of the rock sequence, we can see the formation of Quaternary deposits made up of sediments deriving from aeolian, alluvial and terrestrial phenomena. The Maltese islands are made up of five limestone and clay formations (Fig. 3). In particular, in the central and south-eastern areas of Malta, we can observe the presence of globigerina limestone, while in the south-western is visible an outcrop of Lower Coralline Limestone Formations. In the northern and north-western areas of Malta, there is an abundant presence of Upper Coralline Limestone Formations and blue clays. On the island of Gozo, we can observe more differentiated geology, with a greater presence of blue clay.

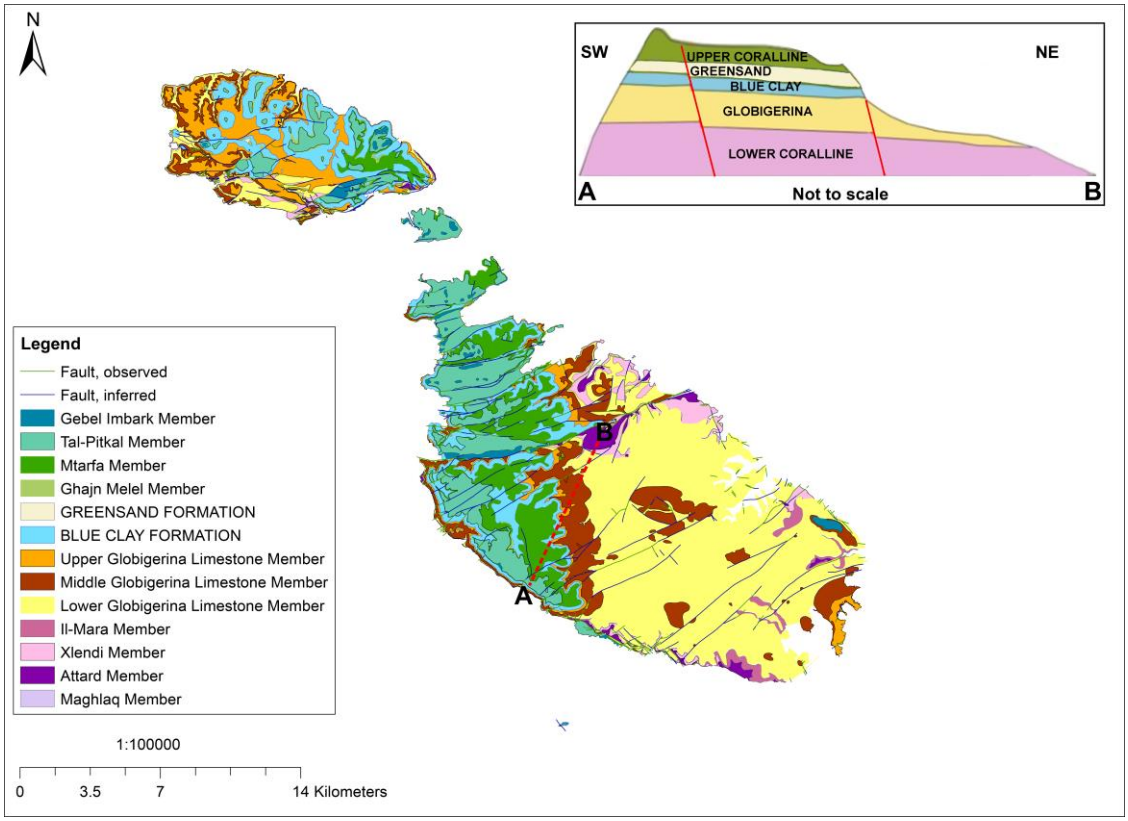

Figure 3: *Geology of the Maltese archipelago based on a map published by the Oil Exploration Directorate (Office of the Prime Minister) in 1993. In the upper right inset, there is a simplified geological section with five geological formations.*

2.1.1 The Lower Coralline Limestone formation

Lower coral limestone (LCL) is the oldest rock layer of the Maltese archipelago and is visible in the areas of Xlendi (Gozo) and Dingli Cliffs (Malta). It is also visible at Fomm ir-Riħ along the Victoria Line Fault (Pedley et al., 2002) (Fig. 4) and in inland outcrops due to faults. This layer was formed during the Oligocene in a shallow gulf-type sea (Magri, 2006) and has a maximum thickness of 140 m. Thanks to this condition, the sunlight was able to reach the seabed, allowing the proliferation of fauna and flora. The fossils of algae and coral are still visible on this layer, thus giving rise to the very name of this layer (Pedley, 1976).

The hardest limestone of all the layers is the light grey one, and it is also the most resistant to the natural phenomenon of erosion. The Lower Coralline Limestone is composed of four members as follows, from the oldest to the most recent:

- Magħlaq member,
- the Attard member,

- Xlendi member
- Il-Mara member.

This rock formation, although coarse and hard, is not homogeneous. In fact, it presents five different facies which indicate the type of depositional environment (Pedley et al. 2002).

The facies include barrier limestones made up of coral algae, shallow limestone muds sheltered by reefs containing fossils of foraminifera and bivalve shells and crisscross layers of sediment accumulated from coarse material that constitute dunes.

The foraminiferal limestones, which developed in deep seas with enough sunshine to allow for the survival and proliferation of foraminifera and bryozoans, are then formed. In the end, we find the formation of the Scutella bed with fossils of sea urchins. However, we can see that the fossils of sea urchins can be found because of a shallower sea depth during that time, which deepened afterwards.

Figure 4: *The Lower Coralline Limestone cliffs at Fomm ir-Rih (Northwestern coast of Malta).*

2.1.2 The Globigerina Limestone formation

The Globigerina limestone formation (GL) sits above the lower coral limestone formation and has some unique peculiarities. Unlike the Lower Coralline Limestone, which is thick-grained and has a greyish colour, GL has a finer grain and a yellowish colour. We can notice a variation in thickness according to the area in which it is found. For example, in the north-western area of Gozo the thickness is 20 metres, while in the south-eastern area of Malta the thickness reaches 207 metres (Pedley et al., 2002; Baldassini et al., 2013).

This layer has homogeneous characteristics because, during the period of formation, the sea level has risen, giving space to the formation of this layer in deep waters and with greater tranquillity. The presence of planktonic foraminifera gives rise to the name of this type of limestone. Globigerina is widespread in the Maltese archipelago but is scarcely visible as it is covered by infrastructures and houses (Pedley et al., 1976). We can see in figure 5 yellow, dark brown and light brown layers in the map indicating Globigerina, which we can further divide into three layers, lower, middle and upper Globigerina limestone respectively.

The lower layer has a solid texture, which makes it easily used for construction sites and the colour is a brownish darker tone of yellow. The middle layer (Fig. 5) cannot be utilised as the previous one in construction because the texture is more fragmented. It has a colour closer to greyish-white. The last upper layer is made of fossils.

Figure 5: *Aerial drone image depicting the stratigraphic contact between Upper and Middle Globigerina Limestone members at Xrobb L-Ghagin, Malta.*

2.1.3 The Blue Clay formation

The Blue Clay formation (BC) is located above the Globigerina Limestone and also varies in thickness according to the area of the island, resulting therefore not being homogeneous. The BC layer has an overall maximum thickness of 75m in Xaghra (island of Gozo) and on the west coast of the island of Malta, where it can reach 70 metres while, in the eastern and southern parts of the island, we do not find this layer. It has a formation similar to globigerina, considering that it is deposited in deep water and consists of fine grains of sediment with an abundance of planktonic organisms. Blue Clay owes its name to the presence of clay which has a colour tending to blue and grey. Depending on the amount of clay and carbonate present, we can observe lighter or darker streaks (Pedley et al., 1978). This layer has also terrigenous sediment a mountainous origin, that comes from the erosion process of the mountains of Sicily that have risen following the movements of the continental plates of Africa and Europe. The clayey material could be of volcanic origin, as a result of volcanic eruptions in Sicily. This formation is very soft and the presence of Kaolinite makes it highly prone to erosion which commonly forms low/rounded slopes (Fig. 6) (Pedley et al., 2002).

Figure 6: *Aerial drone image of the Blue Clay formation at Qarraba Bay, Malta.*

2.1.4 The Greensand formation

Between UCL and BC layers, we can find the Greensand formation (GS). This layer has a reduced thickness compared to the other rocky and massive layers, and for this reason, it is not considered suitable to have an influence on the geology of the island and therefore also the topography of the Maltese archipelago. We can observe the maximum thickness of this layer at Il-Gelmus in Gozo (Fig. 7), as it reaches 11 metres, with a minimum thickness of 1 metre (Pedley et al., 2002). This limestone formation has a dark green colour tending to grey, given by the presence of the mineral Glauconite which was deposited in a relatively warmer and shallow marine environment during the late Miocene epoch (Pedley et al., 1976). As a consequence of atmospheric agents, we can observe that this limestone varies its colour, observing colour tending to brown and orange.

Figure 7: *Greensand outcrop at Il-Gelmus mesa (Gozo). The lower hill slopes are composed of softer Blue Clay*.

2.1.5 The Upper Coralline Limestone formation

The Upper Coralline Limestone (UCL) is the most superficial layer and consequently also the layer that was formed after the others and is therefore more recent. It is widely visible on the island of Malta (Fig. 8) and is particularly present in the areas west of Malta and Gozo. The maximum thickness that has been observed is 140 metres. The UCL was formed in shallow marine environments and consists mainly of several intertidal / marine deposits (Pedley et al., 2002). The various grey shades of this material are given by the presence of various fossils, including coral, algae and also different sand deposits based on the current. This layer is divided into 4 members listed below from oldest to newest (Pedley, 1976):

- the member of Għajn Melel
- the member Mtarfa
- the member Tal-Pitkal
- the member of Ġebel Imbark.

Figure 8: *Upper Coralline Limestone plateau at Selmun promontory (Malta).*

2.1.6 Quaternary deposits

Following the uplift of the Maltese Islands, which dates from the late Miocene to the Pliocene, the islands were raised from the surface of the water and were never submerged again.

The Quaternary period is the youngest in terms of geological time, which extends up to the present day (Hunt, 1999). As classified by geologists (Trechmann, 1938), various quaternary deposits have been identified including valley deposits, coastal conglomerates and breccias, as well as bone deposits of Pleistocene animal remains (Hunt, 1997), which have been found in caves like the example of the Għar Dalam Cave (Fig. 9). The discovery of such animal remains provides evidence that during the last glacial maximum the Maltese islands were physically connected to Sicily by an isthmus (Pedley, 1976).

Figure 9: *Quaternary deposits containing remains of prehistoric animals in the Ghar Dalam cave in Birzebbuga, Malta.*

2.2 The geomorphology of the Maltese islands

As for the geomorphological aspects of the Maltese islands, the landscape shapes are closely connected to geological-structural factors, karst processes and intense gravitational phenomena, as evidenced by the numerous landslides of different types present (Mantovani et al., 2013). During the Miocene epoch, the opening of the Pantelleria Rift system caused several faults, developing Horsts and Grabens and tilting the islands towards the north-east, and causing the western parts of Malta and Gozo to rise. At this time, during the formation of the GL layer, layers of conglomerate were deposited indicating a seabed uplift that continued even after the end of the stratigraphic formation of the Maltese archipelago (Pedley et al., 2002). The tensions generated in the rocks by this uplift gave rise to several faults tending to SW-NE. The island of Malta is crossed by two major fault systems, the main of which is named the Great Fault, also known as the Victoria Lines Fault, which is the oldest with a trend from SW to NE. The second and younger main fault system is known as the Mghalaq Fault and extends NW to SE where the island of Malta has been tilted and where vertical heights

reach about 250 m (Fig. 10). A major fault with orientation SW-NE is also present in the south-east of Gozo and takes the name of South Gozo Fault.

These set of extensive faults mentioned above, together with atmospheric agents, have shaped the Maltese landscape and coast. We observe a lifting and lowering of the rocky layers along the islands where the first results in limestone plateaus (Horst) and the second forms parallel valleys and bays (Graben) which consequently form the characteristic pocket beaches (Devoto, et al., 2012; Magri, 2006; Vella et al., 2013).

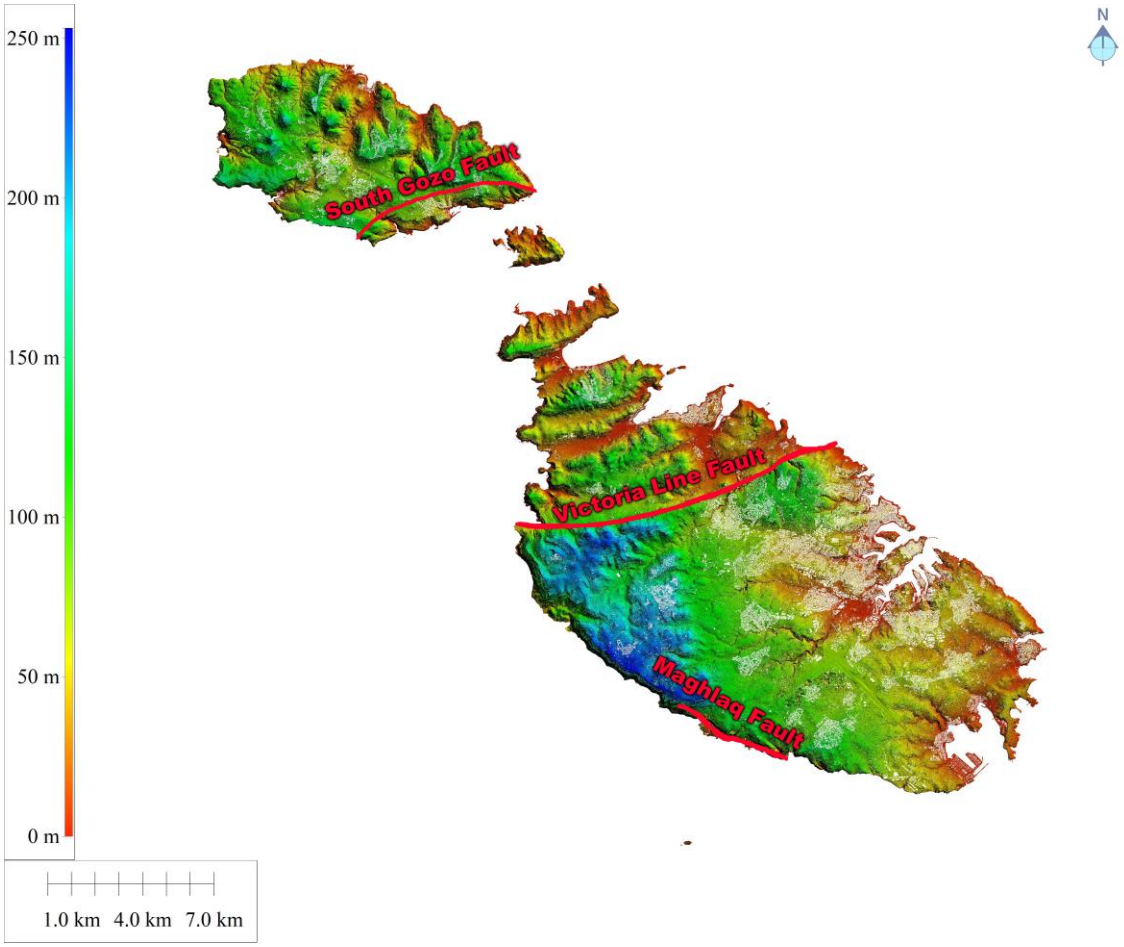

Figure 10: *Digital Terrain Model of Maltese archipelago (ERDF156 MEPA Data) with the main fault systems. The bar on the left indicates the ground altitude above sea level. The DTM highlights the SW-NE tilt of the islands.*

2.2.1 Coastal geomorphology and erosional processes of the Maltese islands

The coastal zone of the Maltese archipelago, which extends for about 200 km for Malta and for about 60 km for Gozo, is dominated by vertical cliffs, rocky coves, indented bays and inlets developed on limestone formations, caves, natural arches and dolines (Furlani et al., 2014; Biolchi et al, 2016). These coastal geomorphological features are the result of the action of the sea that inundates the land due to the action of the wind and waves. Maltese coasts have been classified as seven geomorphotypes (Paskoff et al., 1978; Magri, 2006; Said & Schembri, 2010; Devoto et al., 2012; Biolchi et al., 2016):

- Pocket beach: beaches composed of sand, gravel or pebble deposits included within bays whose headlands that delimit them influence the internal wave climate and consequently the dynamics of sediments and the evolution of the shoreline.
- Cliffs: vertical or sub-vertical steep slope that descends to the sea and ends at the base with a concave ramp. These cliffs are formed into the soft Globigerina Limestone.
- Plunging cliff: vertical or sub-vertical cliff that dips well below water level and without a shore platform at the bottom. This kind of cliff is generally cut into the hard Upper or Lower Coralline Limestone formations and is associated with faults.
- Screes: located between the coasts and the plateaus and characterized by large deposits of slope-failure consisting of heterogeneous limestone blocks lying on clayey slopes and mainly moved by extremely slow-moving landslides.
- Sloping coast: low rocky coast with slopes between 5° and 45°.
- Shore platform: rocky surface along a shore with an inclination between 0° and 5°. This is generated by the erosive action of the waves and other weathering processes.
- Built-up coast: anthropic coast where the landscape is significantly modified by human constructions.

2.2.2 Maltese Pocket Beaches

Maltese Pocket beaches (PBs) cover only 2.4% of the Maltese coast (Deidun et al., 2003; Gauci & Scerri, 2019) and are mostly found in sheltered areas between rocky headlands,

where sea currents along the coast deposit enough material to form sandy or pebble beaches. In the north-east of Malta, the presence of a graben contributed to the formation of the shallow bay of Ghadira (Fig. 11A) bounded by promontories corresponding to the horsts. The sequence of horsts and grabens in the northern area of Malta exposed BC to wave action, producing different fine silted sandy bays. In some PBs, mainly in northern Malta (Golden Bay, Ghajn Tuffieha Bay, Gnejna bay and Mellieha bay), Comino (Santa Maria Bay) and Gozo (Ramla l-Hamra Bay) (Fig. 11B) remnants of aeolian landforms such as sand dunes may be found.

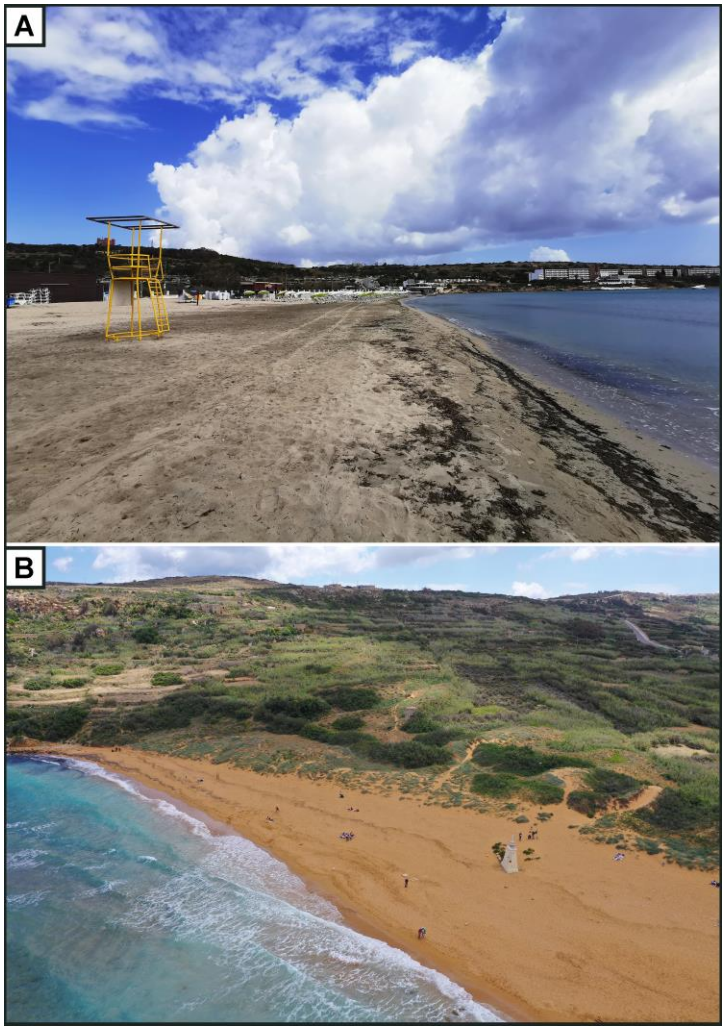

Figure 11: (**A**) *Pocket beach of Mellieha Bay also known as Ghadira Bay in the northwest of Malta.* (**B**) The p*ocket beach* of *Ramla l-Hamra Bay observed from an aerial drone at Xaghra, in the north of the Gozo island.*

2.2.3 Maltese limestone cliffs

Horsts exposed parts of geology to weathering, accelerating erosion processes.

Blue Clay is the softest layer of geological formations found in the Maltese Islands and can be eroded quickly by rain or sea, while the Upper Coralline Limestone overlying is hard, brittle and more resistant to erosion. However, the upper part of the UCL is not covered with soil and is exposed to the erosive action of rain, wind and sun.

The water that infiltrates the porous rock layer of the UCL meets at the base of the impermeable BC layer that holds it back, making it then emerge at the point of contact between the two formations as springs. As the BC layer is eroded by water, the overlying UCL layer becomes unstable, fracturing and causing lateral spreading, topple and fall phenomena (Fig. 12) (Magri, 2008).

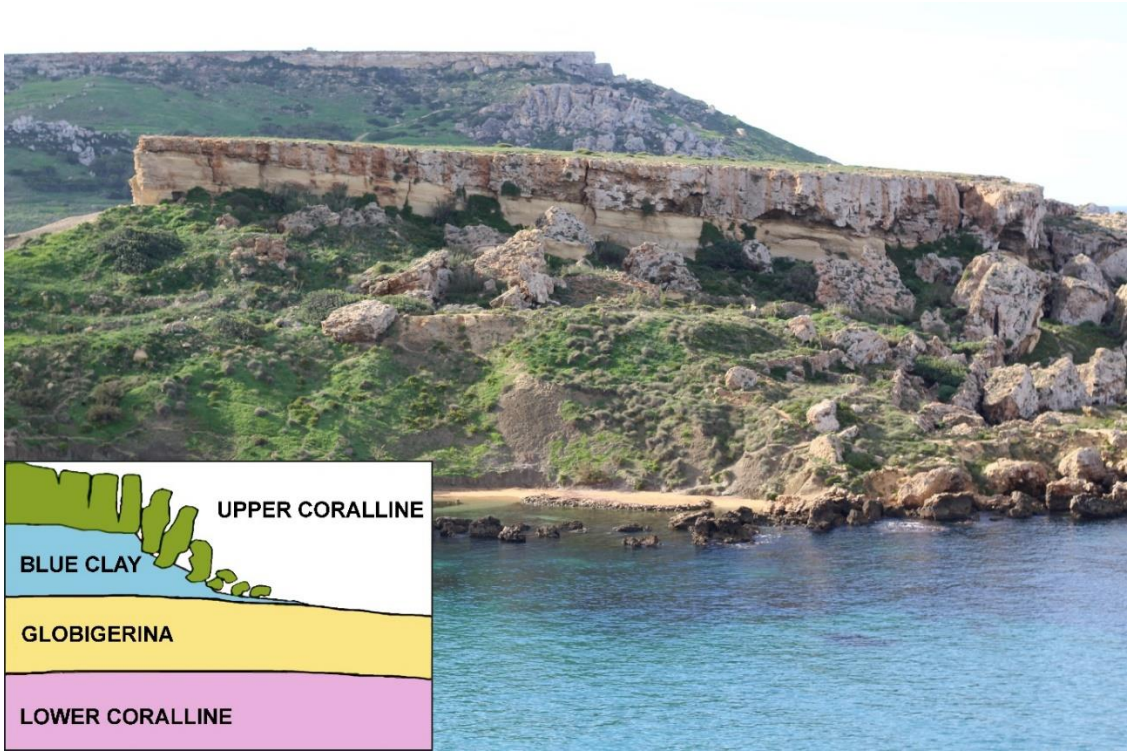

Figure 12: *UCL plateau on top of a sloping BC hill in Il-Qarraba, Mgarr (Malta). The inset on the bottom left shows a graphical representation of the lateral spreading phenomenon affecting the unstable UCL over the soft BC layer, forming boulders along the base of the layer, which slide down over the clay slope.*

This erosive phenomenon is absent in the south-east of the island of Malta, mainly due to a complete erosion of the UCL formation, which is associated with the north-eastern tilting of the archipelago (Pedley et al., 2002). In this area are visible outcrops of Globigerina Limestone which is chalky and fairly soft, but has several harder bands

(phosphatic-conglomeratic beds). It weathers into flat-lying layers which form steps in the landscape at each band.

The hard, impermeable layers of this formation generate minor springs, which help to erode the rock. Finally, under the GL we find the hard Upper Coralline Limestone. This layer is mostly at sea level, which breaking on it shapes steep cliffs, sea caves and natural arches. (Pedley et al., 2002)

2.2.4 Maltese caves, arches and stacks

Many caves, arches and stacks also characterize the coastal scenery of the Maltese archipelago. The constant mechanical and chemical action of sea waves on limestone rocks, near or at sea level, favours the widening of cracks in the cliffs cut along lines of weakness that present abundant joints or faults (Bird, 2008). The positioning of caves above the current sea level suggests the variation over time of the latter.

The action of the waves on the promontories, digs through the vertical joints at sea level, first creating caves and then, when caves break through the headland, natural arches (Fig. 13). Subsequently, as the waves continue the physical and chemical weathering of rocks, over time the volume of the void under the arch increases until the slab collapses. The pillar of the arch, once disconnected from the cliff, takes the name of "stack" (a vertical column of rock) and, as the face of the cliff recedes by erosion, the stack marks the position where the arch stood. These stacks can be eroded or partially collapse to leave a low-lying rock stump. However, the aforementioned evolutionary phases do not always follow the described temporal sequence, as, for example, in the case of the collapse of the Azure Window in Gozo (Fig. 14B), which, on 8th March 2017, after a few days of stormy weather conditions, collapsed and disappeared below the sea surface (Galea et al., 2018) without leaving a stack. Rather, a platform that supported the base of the pillar, which was attached on its southern side, collapsed under the stormy conditions and the fragments deposited in shallow water close to the shore.

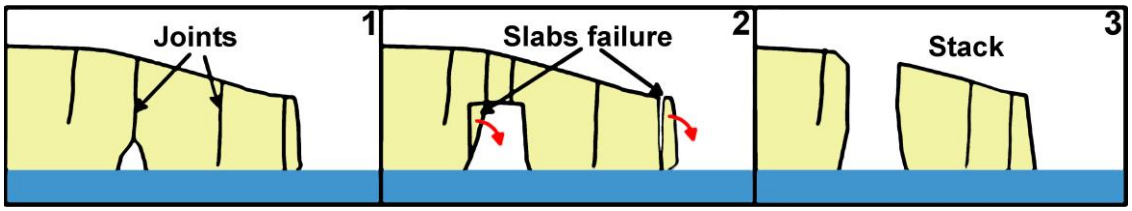

Figure 13: *Evolutionary lifecycle of a natural arch.*

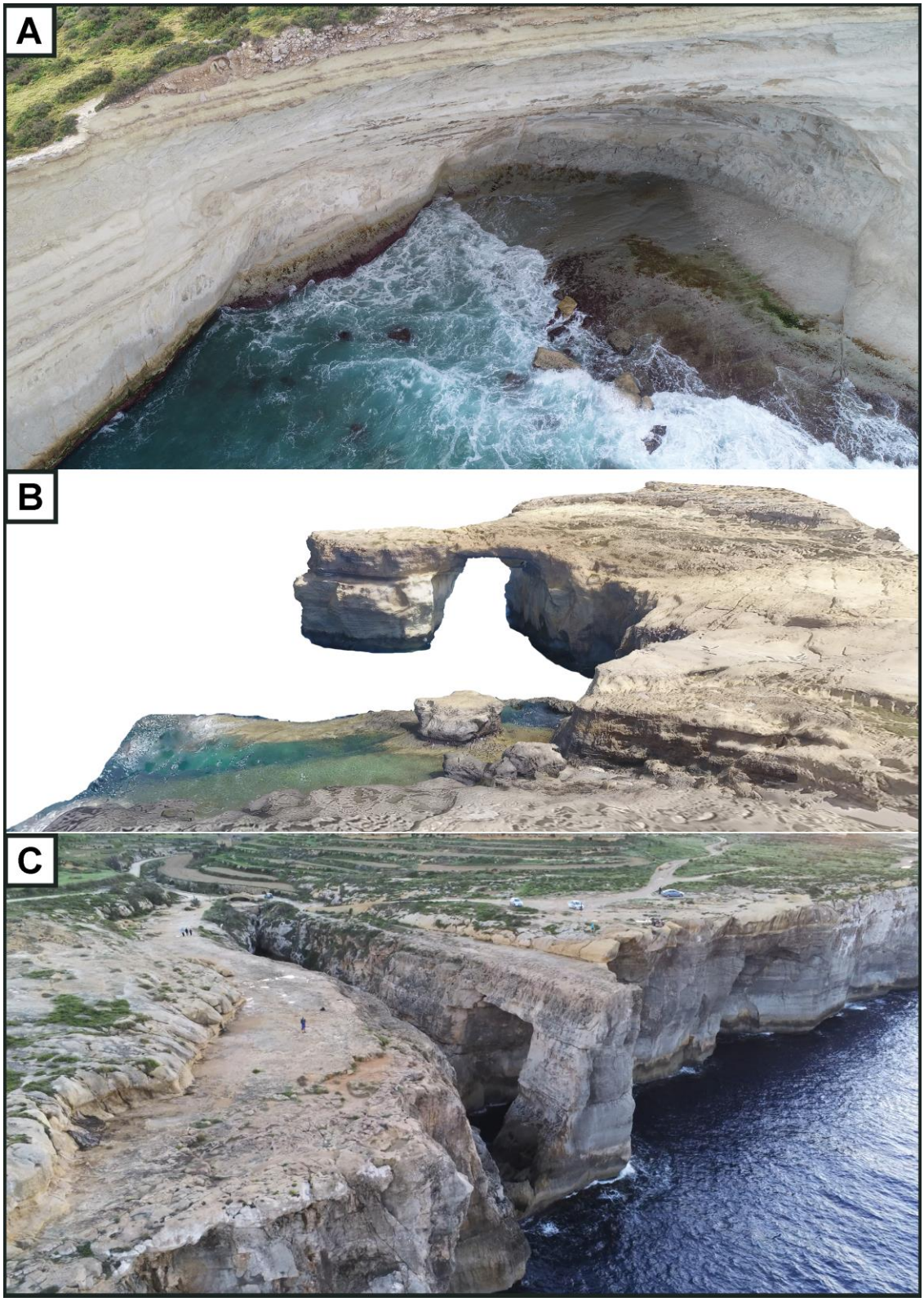

Figure 14: (**A**) *Image of a cave taken by an aerial drone at Xrobb L-Ghagin, southeast of Malta.* (**B**) *High-resolution 3D photogrammetric reconstruction of the Azure Window natural arch in Gozo. This 3D model was used to estimate the volume of rock above sea level that collapsed in 2017* (Galea et al., 2018). (**C**) *Aerial drone picture of the Wied il-Mielah arch on the north-western coast of the island of Gozo.*

2.2.5 Maltese Sinkholes

In the past, acidified rains that penetrated the limestone, following the dissolution of calcium carbonate, formed a complex network of underground channels (Pedley et al., 2002). In this karst landscape, as the underground channels are eroded by the action of water, sinkholes (or dolines) are formed by the collapse of overlying rock (Williams, 2003)

The dolines have a diameter ranging from a few metres to more than 100 m in width (Mantovani et al., 2013; Biolchi et al., 2016). Some examples of sinkholes are found in the north-east of Malta, near Għadira Bay (Devoto et al. 2012) and in the south-west of Malta, near Qrendi and known as Il-Maqluba (Fig. 15A). Another example of a sinkhole on the island of Gozo is represented by the Dwejra Inland Sea (Fig. 15B).

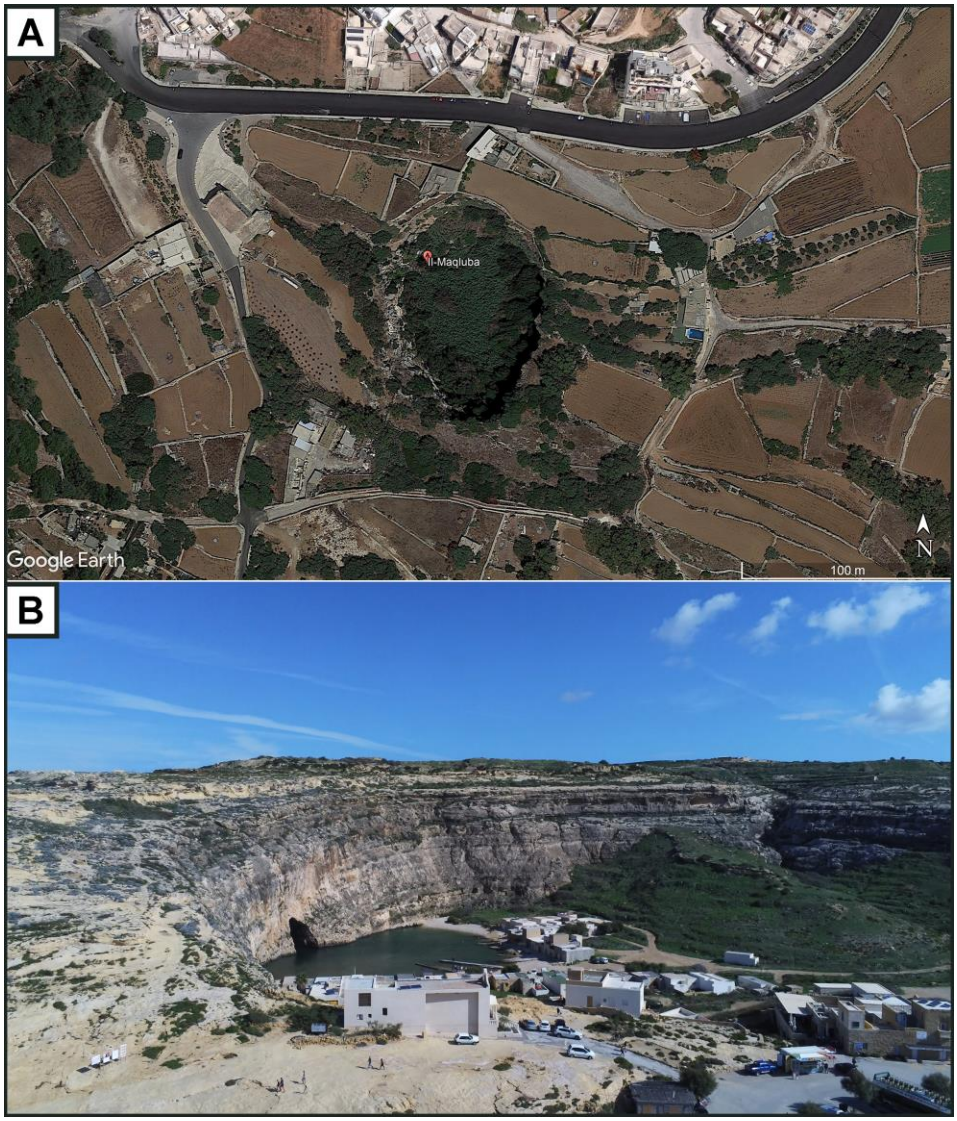

Figure 15: (**A**) *Satellite image of a sinkhole known as Il-Maqluba in Qrendi, south-west of Malta.* (**B**) *A sinkhole observed from an aerial drone at Qawra, in western Gozo.*

3. Methodologies and tools for coastal monitoring

3.1 Geomatics

In recent decades, there has been a progressive expansion of scientific study in the field of earth sciences, with an increasing number of industries studying the Earth using data obtained from global satellite positioning systems, conventional and digital photogrammetry, multispectral and hyperspectral data from aircraft and satellites. Despite this, there is limited awareness of how to properly use this data and make the most of the potential they offer (Gomarasca, 2010).

The term Geomatics (geo: Earth, matics: informatics) is a neologism, which is increasingly widespread in recent years, although it is not yet universally accepted. It is also known as Geospatial Information or Geoinformation and can be defined as the discipline concerned with the collection, analysis, processing and presentation of geographic data.

Geomatics incorporates tools and techniques used in Cartography, Topography, Geodesy, Photogrammetry, Remote sensing, Geographic Information Systems (GIS), Computer Science, etc. Through the integration of these disciplines and techniques, it allows us to build a highly accurate digital profile of our environment. To date, many Nations of the world are using this multidisciplinary discipline to build a Spatial Data Infrastructure (SDI) that enables the sharing and effective usage of geographic information by standardizing formats and protocols for access and interoperability (Budhathoki et al., 2008).

One practical example is represented by the SIntegraM project which aims to develop the integration of spatial data for the Maltese Islands (Formosa, 2017). The implementation and sharing of these databases offer the use of operational information for the monitoring and management of the environment and civil security. An example of geospatial database implementation at the European level is represented by the initiative GMES (Global Monitoring for Environment and Security), which aims to establish international cooperation for the provision and use of operational information for monitoring and management of the environment and civil security. It addresses the main policy issues associated with Earth observation data, as well as with other types of environmental data (Harris & Browning, 2003).

Geomatics is constituted by the following multiple techniques and fields of study:

- Information technology: representing the data and information through the use of hardware devices and operating systems;
- Geodesy: determining the Earth's aspect and dimension (Vermeer, 2019);
- Topography: it is aggregating different methodologies and equipment to meticulously measure and illustrate every detail of the Earth's surface, through the use of planimetry and land surveying for example.
- Cartography: describing the aspect and measuring the Earth including all the natural and artificial features, by representing ample territories using graphical or numerical illustrations applying defined rules.
- Photogrammetry: to establish the characteristics of the objects by measuring them from photographic images without actually being physically in contact with the object (Imam, 2018).
- Remote sensing: the data of the environment is obtained remotely, combining procedures and methodologies for consequent processing and analysis.
- Global positioning system (GPS): it is composed of various satellites in orbit around the Globe; observation stations on the Earth; and lastly the singular GPS devices (Upreti & Kumar, 2008).
- Laser scanning system: it is a survey method for obtaining three-dimensional data for aggregated systems (Kukko, 2013).
- Geographical information system (GIS): it is an electronic system for the obtaining, depository, scrutiny and presenting of geographical data of a specific geographic area, describing the Earth's surface features and environmental characteristics (Ali, 2020).
- Decision support system (DSS): management and presentation of data creating solutions for the final decision maker of the process (Gomarasca, 2010).

3.1.1 The key role of UAVs in geomatics and scientific research

Unmanned aerial vehicles (UAVs), commonly called drones, are defined as aircrafts without a human pilot on board (Bento, 2008). Albeit unmanned aerial vehicles (UAVs) are extensively known for their utilization in military operations, they are used for scientific research and business applications in situations where it is necessary to obtain

images of geographic areas where there has been a natural disaster or data necessary to construction sites (Bento, 2008).

UAVs are a component of an Unmanned Aerial System (UAS), which includes: UAV, Control Station (CS) and a communication system between these two. The UAVs can be remotely controlled by a human operator or be completely autonomous thanks to on-board computers and the Global Navigation Satellite System (GNSS). Remotely controlled UAVs have existed since the early 1900s, when they were only used in military operations. The first true unmanned aircraft was developed in 1916, immediately after the outbreak of the First World War (Mátyás & Máté, 2019). The name of the project, as well as the aircraft, was Ruston Proctor Aerial Target: an unmanned military aircraft, piloted via an innovative radio wave guidance system, developed by the visionary British engineer Archibald Montgomery Low (Jeler, 2020).

Until 1960, UAVs saw their development only in the war field, but from this moment on, thanks to the innovations in transistor technology, miniaturized components for radio control transmission were available to customers at a reasonable cost. A boom in the popularity of radio-controlled aeroplanes in the United States followed, from models for indoor use to more elaborated ones for flying in larger spaces (Mátyás & Máté, 2019). Recognizing the potential of drone applications in many industries, the Federal Aviation Administration (FAA) in 2006 issued the first permits for commercial drones. Thus, it was possible to think about the new possibilities of using UAVs for companies and professionals, from the world of photography to that of scientific research. As electronic technology has become smaller, cheaper and more efficient, in 2010 we witnessed the widespread diffusion of commercial UAVs for amateur and professional use, capable of flying with complete autonomy carrying various types of sensors (Mátyás & Máté, 2019). Furthermore, the UAVs are generally less expensive than ordinary aeroplanes and the absence of a human being on board provides various benefits such as an increase in time duration and increased effectiveness in covertness (Mátyás & Máté, 2019).

The world of UAVs is revolutionizing the concept of remote sensing, setting new frontiers both in terms of data quality on the ground and for the great versatility of the method. There are numerous types of UAVs, not only the aerial ones that, however, are divided into multirotor, such as drones equipped with rotors that guarantee the lift of the vehicle, and fixed-wing that base their lift mainly on the wing which therefore

guarantees to glide (Šulyová, 2021). The multirotor types are able to perform a hovering flight and have the advantage of being able to manoeuvre in tight spaces and also do not require large areas for take-off and landing. The fixed-wing UAVs, on the other hand, have an advantage in flight autonomy that allows coverage of larger areas. Among the air vehicles, there are the least used airships and helicopters (Šulyová, 2021). However, the term drone can also include marine ones, which can be divided into surface vehicles (ASV: Autonomous Surface Vehicle or USV: Unmanned Surface Vehicle) or underwater (AUV: Autonomous Underwater Vehicle and ROV: Remotely Operated Vehicle). The Vessel drones allow, among other things, to detect the surface of the seabed using a sonar, which can be in single beam configuration (sonar that sends punctual pulses) and Multibeam (sonar that sends pulse beams) (Trasviña-Moreno et al., 2017).

Terrestrial drones, the so-called Rover, used for example for the transport of materials and for land operations difficult to access for humans can be mentioned (Arfaoui, 2017). Aerial drones are means capable of hosting a large range of sensors that are used in various sectors (Arfaoui, 2017). Among the most common sensors are:

Camera, this is a passive sensor capable of capturing the light passing through the lens and impressing the photosensitive sensor. The camera processor based on light intensity and hue, in terms of RGB, is able to reconstruct an image by associating each pixel with a colour with a different gradation. The photographic sensor is generally applied to the drone via a 2 or 3-axis drone camera stabilizer which eliminates vibrations and wobble. This stabilizer is called gimbal and can use brushless motors to adjust the camera according to the movements of the drone (Arfaoui, 2017). A stabilized camera allows to acquire photogrammetric datasets which, processed with the Structure from Motion technique, will allow to extract a photogrammetric output. The main application fields of photogrammetry concern the geological field such as for example 3d reconstruction of a slope or a quarry, the engineering field, such as the reconstruction of infrastructures and the environmental field such as monitoring the state of health of a landfill (Arfaoui, 2017).

A thermal imaging camera is a sensor sensitive to infrared radiation with wavelengths from about 1,000 nm (1 µm) to about 14,000 nm (14 µm). The use of this sensor allows to detect the emissivity of a body and therefore the heat that is released. Thermography allows you to acquire data sets that may or may not indicate absolute body temperature.

Thermal imaging cameras can be radiometric or non-radiometric (Arfaoui, 2017). The former is in turn divided into central radiometric, if only the temperature in the central point of the photo is detected, or total radiometric, which detects the temperature in all pixels of the photo (or thermogram). Instead, non-radiometric thermal imaging cameras only display temperature fields without the possibility of correction and allow the determination of the temperature relationships between different points in the thermogram. The main applications of thermography are found in the fields of geology, archaeology, engineering and agronomy (Arfaoui, 2017).

A multispectral sensor is a sensor capable of acquiring data in RGB and near-infrared (4 bands) and is also sensitive to RedEdge (5 bands), which is a wavelength between near-infrared and red. This sensor is used in precision agriculture for the calculation of the vegetative state index, and in particular for the Normalized Vegetation Difference Index (NDVI). It is therefore used to determine the health of plants (Balestrieri et al., 2021).

The hyper-spectral sensor is a sensor capable of acquiring data over a wide range of wavelengths. The number of spectral intervals divided is defined by the number of channels of the hyperspectral chamber. This sensor is generally used to determine the spectral signature of objects and thus discriminate one material from another. The hyperspectral chamber is generally used in geology to determine the geological nature of a given material, and in the agricultural sector to distinguish plant varieties (Balestrieri et al., 2021).

LiDAR sensor, which stands for “Light Detection and Ranging”, is an active sensor capable of launching a pulse towards the ground that will bounce in any direction for scattering once it hits the surface. Some of these impulses return to the emitter, which will also play the role of receiver and allow the reconstruction of the surface both in terms of the Digital Terrain Model (DTM) corresponding to the last return and the Digital Surface Model (DSM) corresponding to the first return. The application sector concerns the geological field for the reconstruction of the ground surface (Schulz, 2007), the engineering field and the environmental sector (Balestrieri et al., 2021). While once scientists could only observe the Earth from above using manned aircraft or satellites, today they are expanding, developing and perfecting their research with drones. UAVs in the civil sector are already a key component in commercial activities, industrial activities, entertainment and emergency services (Šulyová, 2021).

3.1.2 Anatomy of a UAV

Modern UAVs consist of a series of electronic components integrated and mounted in a frame, which varies its structure according to the number of rotors. A drone can have four propellers (quadcopter), six propellers (hexacopter) (Fig. 16), eight propellers (octocopter) or even more (Chen et al.,2016). The frame material can be different, such as wood, plastic, aluminium, and carbon fibre and this choice determines the flight of the drone, its weight, the duration of the flight and its impact resistance. The main component, that can be defined as the brain of the drone, is the Flight controller (FC), which controls most of the electrical components on board with the assistance of a microprocessor. It mainly deals with keeping the UAV "in balance" during the flight (Chen et al., 2016). The FC interfaces (or integrates) the Inertial Measurement Unit (IMU), consisting of an electronic device that measures linear acceleration using an accelerometer, rotational rate using a gyroscope, heading orientation using a magnetometer and altitude using a barometer. All this information is crucial for the stabilization and movement of the drone. In addition, the FC interfaces with the GNSS system and obstacle detection sensors if the UAV is equipped with them (Mogili & Deepak, 2018). The radio control system (RC), in most cases, consists of a transmitter and a special receiver that interfaces with the Flight Controller, which sends inputs to the engines. On professional UAVs we generally find brushless electric motors that work without the need for sliding electrical contacts on the motor shaft and have reduced mechanical resistance and no risk of sparks. The Flight Controller is connected to the brushless motors through small electronic boards called Electronic Speed Control (ESC) which allow the propellers to turn at variable speeds suggested by the FC. Propellers can be made of plastic or carbon fibre, for optimal weight and safety characteristics (Mogili & Deepak, 2018). Finally, the energy that powers the whole system described above is given by one or more batteries. Typically, lithium-polymer batteries are widely used on modern drones due to their efficiency and light weight.

Figure 16: *H*exacopter *DJI M600 Pro equipped with LiDAR, thermal camera and RGB camera.*

3.1.3 Structure-from-motion (SfM) photogrammetry

Photogrammetry can be described as a science to obtain reliable information about the spatial properties of land surfaces and objects, without physical contact (Schenk, 2005) and therefore allows to determine metrically the shape and position of objects, starting from at least two distinct frames showing the same object (stereo-pair).

In recent years, the development of computers capable of handling a large amount of data and computerized graphics has made it possible to use digital photogrammetry simpler and faster and with lower costs. The advent of these technologies, in fact, has made the old analogue metric cameras obsolete in favour of digital cameras. Developed in the 1990s, this method is suitable for a set of images representing the three-dimensional structure of the scene, which derive from a moving sensor (Spetsakis & Aloimonos, 1991).

Digital photogrammetry or Structure from Motion (SfM) photogrammetry currently represents one of the most reliable, economical and precise data acquisition techniques of the territory as it is very useful in the analysis of morphological changes. This is a valid

technique in the study and analysis of geographical data, mainly because of reduced costs, accessible and quick use, and precision of spatial and temporal frequency (Eltner & Sofia, 2020). Digital photogrammetry operates under the same basic tenets as stereoscopic photogrammetry, i.e., that a 3D model can be reconstructed starting from a series of overlapping, offset images and it differs because the geometry of the scene, camera positions and orientation are solved automatically without the need to specify a priori, a network of targets which have known 3-D positions (Westoby et al., 2012). Common points are identified on each image and a so-called “lines of sight" (or ray) can be developed from each camera that is pointed at the object. These lines of sight are mathematically intersected to produce the three-dimensional coordinates of the points of interest (Peterson et al., 2015). The possibilities of SfM appear boundless and it can be applied to different fields such as topographic mapping, architecture, engineering, manufacturing, police investigation, geology, archaeology and many other fields (Eltner & Sofia, 2020). There are several software options for processing photographs to obtain 3D point clouds with XYZ coordinates and RGB colour values. Among the most popular software for SfM processing we can find Agisoft Metashape (Agisoft, 2021), Pix4D (Pix4D mapper, 2021), 3DF Zephyr (3DFlow, 2021), VisualSFM (Wu, 2011) and Autodesk ReCap Photo (Autodesk ReCap Photo, 2021).

The Structure from Motion processing of the images takes place through four distinct and successive phases (Figure 17):

1. Based on Computer Vision algorithms, SfM extracts the notable points from individual photos, and crosses them, finding their coordinates in space. In order to reconstruct the three-dimensionality of a scene, it is necessary to reconstruct the shooting position of the individual photographs, the so-called gripping geometry. The scenario object of interest must be taken with at least a pair of overlapping photographs, obtained by positioning the camera at approximately the same distance from the object and with the same orientation (Martínez-Espejo Zaragoza et al., 2017). The software compares the pairs of frames and searches for similarities between the pairs. By refining its analysis, it then finds the coordinates of all the visible points that define the surface of the object, corresponding to the pixels of the photographs, projecting them into 3D space. If the object to be filmed has a considerable length or has several faces, several

pairs of frames will be required (Eltner & Sofia, 2020). Starting from the key points, through a bundle adjustment process, the camera is automatically calibrated and the shooting position of the individual photographs is reconstructed and, for each key point, the real coordinates x, y, and z are obtained which are materialized three-dimensionally in a sparse points cloud, i.e. in a low-density point cloud. This first phase is called camera alignment: it allows the automatic orientation of the cameras and images in space. A "sparse" point cloud is then created, forming a sort of spatial model of "solid" photos of the captured objects (Eltner & Sofia, 2020).

2. In the next step, the low-density point cloud is thickened by increasing the number of points (dense point cloud).
3. Starting from a dense point cloud, a continuous surface is reconstructed with polygons whose vertices are the points of the dense cloud. This first phase is called mesh reconstruction and the colour is applied to this mesh, in two alternative ways: colour-per-vertex or texture mapping (Martínez-Espejo Zaragoza et al., 2017).
4. The textured 3D model must be scaled across a reference distance, as the software cannot automatically size objects that appear in photos. The software has tools that allow you to edit the point cloud and the mesh and export the model obtained in CAD or other software where it will be subject to further processing (Martínez-Espejo Zaragoza et al., 2017).

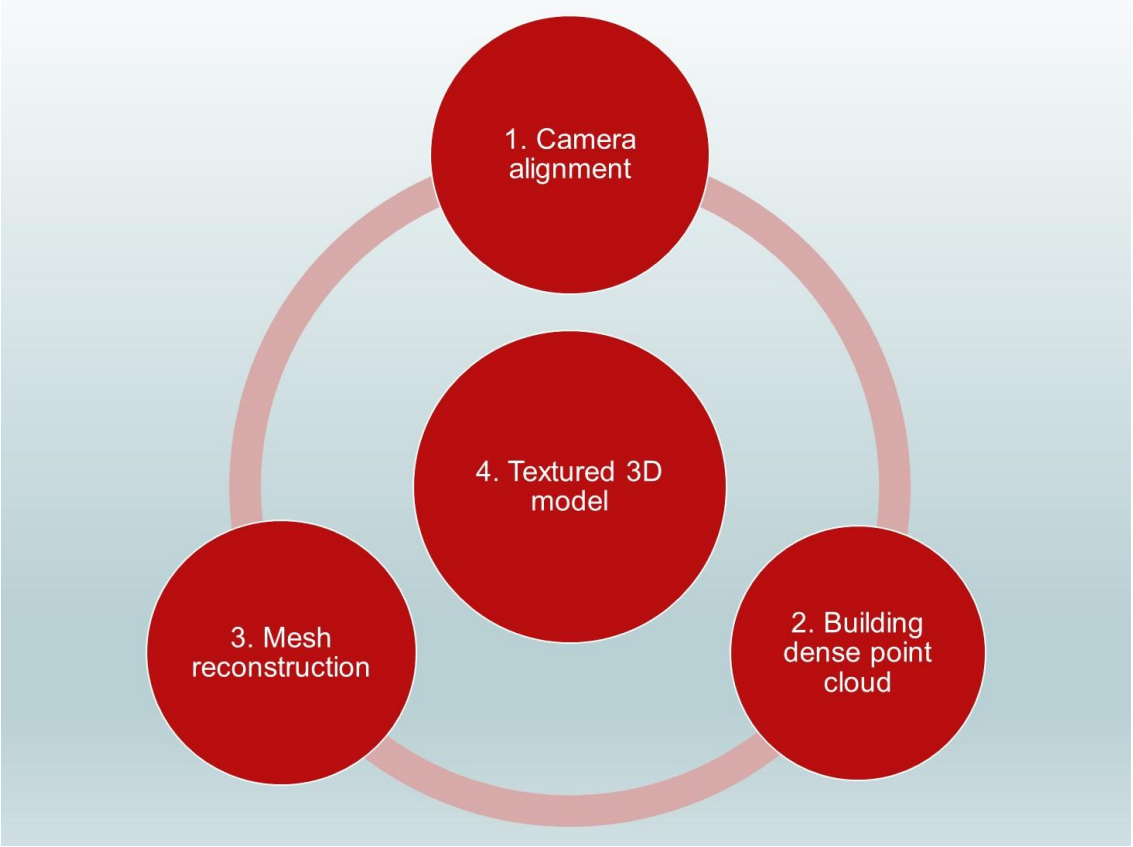

Figure 17: *Photogrammetric processing workflow scheme.*

3.2 Geophysics

Geophysics is the science that studies the physical phenomena that take place in the atmosphere, on the surface and in the interior of the Earth (Sharma, 1985). It has an interdisciplinary structure, as it uses the observations and results of numerous disciplines that study the Earth, such as astronomy, geodesy, geology, geochemistry, physical geography, and physics that provide the general laws, methods and tools for the analysis and interpretation of different phenomena (Sharma, 1985). Geophysics is traditionally divided into three major branches: the geophysics of the solid Earth, the geophysics of the atmosphere and the geophysics of the hydrosphere. Regarding the methods of investigation and the purpose of the research, geophysics is usually divided into pure and applied (Mulet-Forteza et al., 2020).

Pure geophysics studies the properties and physical conditions of the Earth in order to reach an in-depth description of physical phenomena in their general aspects and to interpret the causes that produce them (Mulet-Forteza et al., 2020). In geophysics, unlike what happens in other physical disciplines, observation data prevail over

experimental data: it is in fact difficult, if not practically impossible, to reproduce the natural phenomena that affect geophysics on the same spatial and temporal scale in which they manifest themselves; moreover, many and changing environmental elements intervene in natural phenomena, not always known or repeatable in the laboratory (Mulet-Forteza et al., 2020).

The method of investigation of pure geophysics is therefore essentially that of collecting as many elements as possible, mathematically elaborating them and constructing models that, by successive approximations, account for the observed phenomena. It can therefore be understood how geophysics benefits when the researches and data observed are very numerous and extended to the entire earth's surface (Mussett & Khan, 2000).

Applied geophysics aims to use the physical properties and phenomena studied by pure geophysics for practical purposes; its fields of application are many; just think of the possibility of exploiting the terrestrial thermal energy or converting the dynamic energy of the tides into electrical energy, investigations on the nature of the subsoil, studies on the stability of soils, archaeological research, etc (Ahmed, 2014). The field of research in which applied geophysics offers the best results is currently that of subsurface prospecting (Mussett & Khan, 2000). In these researches, methods are used that make it possible to eliminate, as far as possible, subjective evaluations, actions at a distance, selectivity of the results, that is, a significant variation of the observed values according to the medium in which the properties are manifested. These methods are gravimetric, magnetic, seismic, electrical, radioactive, geothermal and electromagnetic methods (Ahmed, 2014).

3.2.1 Ground penetrating radar (GPR)

Ground Penetrating Radar (GPR) or georadar is a non-invasive methodology used in geophysics and many other fields, such as geology, hydrogeology, civil engineering, cultural heritage, archaeology and environmental monitoring (Annan, 2002).

The theory on which the georadar technology is based developed in the second half of the 19th century with the Maxwell and Hertz equations describing the propagation of electromagnetic waves in a medium (Baker et al., 2007). The four equations of Maxwell

(1867), which relate the vectors of electric and magnetic fields with their sources, are reported with the following equations:

$$\nabla \cdot D = \rho \qquad (1)$$

$$\nabla \cdot B = 0 \qquad (2)$$

$$\nabla \cdot E = -\frac{\partial B}{\partial t} + M \qquad (3)$$

$$\nabla \cdot H = -\frac{\partial D}{\partial t} + J \qquad (4)$$

The so-called constitutive equations relate the strengths of the electric and magnetic fields, E and H, with the vectors of electric displacement and magnetic induction D and B, respectively; J and M, are the electric and magnetic current density vectors, ρ is the density of electric charge, and t is the time (Xu & McMechan, 1997).

In a homogeneous and isotropic medium, the constitutive equations take on a simple expression

$$D = \varepsilon E \qquad (5)$$

$$B = \mu H \qquad (6)$$

$$J = \sigma E \qquad (7)$$

$$M = \chi H \qquad (8)$$

by relating these quantities through the four electromagnetic parameters that describe the electromagnetic properties of materials and that can characterize a soil or a ground:

the relative permittivity ε, conductivity σ, magnetic permeability μ and magnetic susceptibility χ (it is however necessary to note that some of them are interrelated) (Xu & McMechan, 1997).

The dielectric constant k of a material is the ratio of its permittivity ε to the permittivity of vacuum ε 0, so:

$$\mathrm{k} = \frac{\varepsilon}{\varepsilon o} \qquad (9)$$

The dielectric constant is therefore also known as the relative permittivity of the material. Since the dielectric constant is just a ratio of two similar quantities, it is dimensionless.

Taking into account that, in most soils, polarization phenomena dominate over electrical conduction phenomena, and that in reality it is unusual to find soils with magnetic characteristics, we can focus our attention only on the EE parameter, which describes the capacity of a material to be electrically polarized in the presence of an external electric field (Matthew, 2015).

These properties are intrinsic to the georadar method which operates at frequencies ranging from a few MHz to a few GHz and the depth of penetration depends on the electrical properties of the ground. It produces a beam of electromagnetic waves that travels through the ground at a speed that varies according to the properties of the ground and the amount of water present (Halliday et al., 2013).

$$v = \frac{1}{\sqrt{\varepsilon\mu}} \sim \frac{c}{\sqrt{\varepsilon_r}} \qquad (10)$$

The last expression of (9), in which *c*, the speed of light and ε_r, the dielectric constant of the material, is valid in the case of materials that are good dielectrics and the magnetic properties are close to those of vacuum ($\mu = \mu_0$), i.e. propagation occurs essentially without dispersion (Baker et al., 2007).

The technique on which the georadar is based consists of sending electromagnetic pulses of short duration (1-10 ns) at high frequency (MHz or GHz) in the investigated medium. By introducing electromagnetic waves into a non-homogeneous medium, the known reflection and refraction effects known in optics will be obtained (Meles et al., 2010). With each change in the refractive index linked to the wavelength λ of the radiation, there will be a partial reflection of the electromagnetic waves. These can be intercepted and analysed by means of special equipment, of which the georadar is provided; in fact, it allows to acquire waveforms, or traces, on which the position on the

time scale (abscissa) and the intensity (ordinate) of the reflected or refracted impulses can be identified (Annan, 2003).

$$n(\lambda) = \frac{c}{v(\lambda)} \qquad (11)$$

The position on the time scale of a peak determines the distance between the antennas and the object that produces the diffusion (Meles et al., 2010). In the hypothesis that the investigated medium is homogeneous, the propagation speed v can be considered constant, so that the depth of the target is calculated as:

$$P = \frac{t_b v}{2} \qquad (12)$$

Where t_b is the return time of the signal (TWT - Two Way Travel time). The intensity of the reflection will be influenced both by the attenuation that the waves undergo, and by the coefficient of reflection R, which mainly depends on the contrast between the different dielectric properties of a propagation medium, the ground and the investigated object, or the layer with different physical properties (Jol, 2008).

The instrumentation used to carry out georadar measurements consists of a control unit, which is generally connected to two or more antennas (Daniels, 2000). It contains both the electronics that generate the electrical impulse, which is transformed into electromagnetic oscillation in the transmitting antenna (Tx) and the instrumentation designed to sample and store the data from the receiving antenna (Rx). This apparatus is moved along the surface of the vehicle to be investigated (whether it is a ground, a floor, a block of rock, a wall, etc.), along straight lines called profiles (Daniels, 2000). From the measurements, a so-called radargram will then be obtained, that is a two-dimensional reconstruction of the medium as if it were seen at different radio frequencies, the result of the envelope of the individual traces acquired along the profile being investigated. The reflections that the signal undergoes will be identifiable on each trace, which may be due both to the different stratification present in the soil and to well-defined objects (Solla & Pérez-Gracia, 2016). In both cases, there is a variation of the electromagnetic parameters, but the reflections produced will be different. In the first case, a sub-horizontal reflector will be obtained, while in the second a reflection hyperbola will be displayed (Daniels, 2000). This is due to the fact that as the radar is

moved horizontally, the round trip time of the signal diffused by the same reflector has a first decreasing trend, up to the vertex, when the antennas are above the target, and then increases (Solla & Pérez-Gracia, 2016). If it is assumed that the distance between the georadar and the diffuser object is much larger than the size of the latter, so that it can be considered point-like, on the plane (x, t) the points where the reflection is identified will follow the equation:

$$t = \frac{\sqrt{(x_b - x)^2 + P^2}}{v} \qquad (13)$$

$$\frac{t^2}{P^2} = -\frac{(x_b - x)^2}{P^2} = 1 \qquad (14)$$

where, as defined in the previous equations, P is the depth at which the object is placed, v is the speed of propagation, x_b the horizontal position of the target on the profile (Meles et al., 2010). As can be seen from the second equation, we obtain a hyperbola with the vertex in (x_b; t_b), with $t_b = P/v$.

The major difference between GPR and common radars used in the atmosphere is that of having one or more directional antennas: in fact, they are shielded in such a way as to give a privileged direction to the waves emitted, namely that of the ground. Among the construction features, the disturbance effects due to the proximity of the source of the EM waves with the air and ground interface must also be taken into account (Koppenjan, 2009). The antennas that are used have peculiarities that distinguish them based on the use to be made of them. It is possible to have antennas in both monostatic and bistatic modes. In the first, the antenna incorporates Tx and Rx in a single structure, while in the bistatic mode there are physically separate transmitter and receiver (Ali et al., 2017). The first configuration usually investigates more or less large areas to understand the conformation of the subsoil, while the second, which has a higher minimum depth of investigation, is used to obtain more detailed information on non-superficial targets. Furthermore, the bistatic mode allows the investigation of a single area both with a simple scan (single folding) and by scanning the same point from different angles (multi-folding) (Ali et al., 2017). In the second case, the Tx and Rx antennas can be moved by the same distance, starting from a central point (Common

Mid-Point), or only the receiver can be moved (Wide Angle Reflection and Refraction) (Annan, 2005).

The depth and vertical resolution that can be obtained are directly dependent on the frequency at which the antenna operates. A higher frequency corresponds to a better spatial resolution, but also a greater attenuation of the waves, and therefore a lower depth of investigation (Ali et al., 2017). The frequency depends on the size of the antenna from which the pulse was generated, and is not in any case unique. The frequency spectrum of the generated pulses is designed to have a Gaussian shape, centred around the central or dominant frequency, and a bandwidth whose value is comparable to that of the central frequency (Ali et al., 2017). The graphical representation of the georadar data is a fundamental step for understanding and interpreting the results. The final report of each survey should present the data in a way that is understandable to both industry experts and non-expert clients, in order to produce robust and easy-to-learn interpretations for all. In most cases, the reports show radargrams in different colour scales and modern software allows a very visual resolution and high definition (Rial et al., 2011). Furthermore, if the acquisitions have foreseen parallel profiles within an x, y grid, it is possible to obtain and, therefore, display maps (or floor plans) of the investigated area which represent, at various depths, not only geometric of the buried objects but also the dimensions, usually using an average envelope algorithm, also known as average envelope amplitude. Finally, if the quality of the data allows, it is possible to produce a 3D representation of the data (Rial et al., 2011). This representation is also called pseudo as it is the result of a false perspective section model (or isosurface), in which a threshold value is established on the basis of the average envelope algorithm. This method of processing georadar data is held in great consideration thanks to the fact that it allows to better interpret the spatial relationships between anomalies (Figure 18) (Annan, 2005).

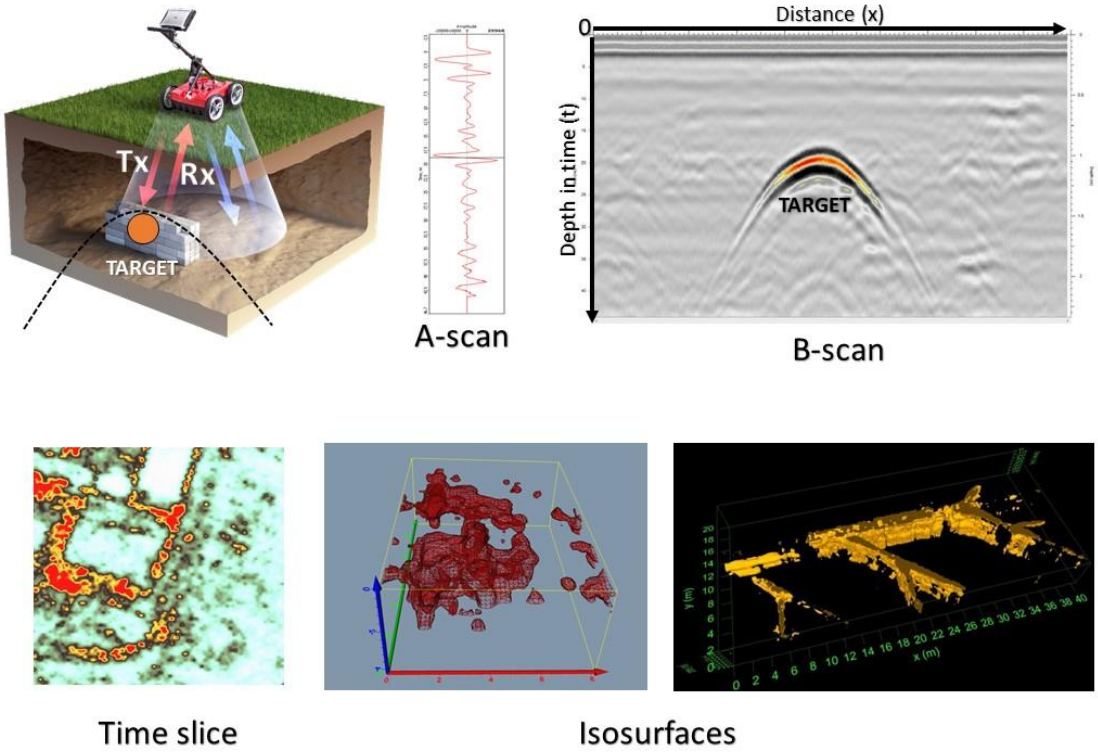

Figure 18: *Schematic of the georadar operation with the four typical representations of a detected anomaly: a single A-scan georadar trace in correspondence with the anomaly (top centre), the B-scan or radargram (top right), the time slice (bottom left) and 3D reconstructions of the isosurfaces (bottom centre and right). It should be noted that in the radargram only the apex of the reflection hyperbola identifies the correct position of the buried object (or target).*

3.2.2 Electrical resistivity tomography (ERT)

The geophysical technique of electrical resistivity tomography (ERT) or electrical resistivity imaging (ERI) is a geophysical technique for imaging sub-surface structures (Sudha et al., 2009). This technique is useful for the detection of vertical and / or lateral changes in electrical resistivity, which translates into the possibility of detecting faults, fractures, cavities, areas of intrusion of pollutants, lateral contacts between geological formations with sufficient resistivity contrast, etc. (Perrone et al., 2014). The rock, as a mixture of minerals, is generally a bad conductor and its electrical conductivity depends on its degree of fracturing or porosity and the amount of water that permeates it (Tso et al., 2017). The conductivity of water is in fact higher than in the rock and depends on the temperature and the salts dissolved in it (which in turn depend on the permeated

rock). The electrical resistivity method can be used in mineral exploration to map massive ores (Daniels & Dyck, 1984), in groundwater exploration to delineate aquifers (Riwayat et al., 2018), in geothermal exploration to locate geothermal fields (Kana et al., 2015), in engineering site investigation to determine the depth to bedrock (Syukri et al., 2021), and in environmental studies for environmental assessment (Carrière et al., 2013). In ERT surveys, the electrical resistivity (ρ) is measured, which is the inverse of conductivity and therefore counts high values. The equipment that carries out this measurement is the resistivity meter also known as georesistivimeter (Perrone et al., 2014). The measurement is obtained through a quadrupole (four electrodes inserted in the ground with a suitable geometry) divided into a pair AB of current electrodes (also called energizers) and a pair MN of voltage (or measurement) electrodes. After a series of quadrupolar measurements, the result is an electrostratigraphic profile of the subsoil which must be interpreted to derive a geostratigraphic profile (Parsekian et al., 2017). The resistivity of the ground is called apparent resistivity (ρa). This parameter, expressed in [Ω · m], indicates the ability of a material to resist the passage of electrical charges. The resistivity, measured as a voltage drop [mV] at the ends of the measuring electrodes MN following the injection of a current [mA] from the electrodes AB, is representative of the lithology of the rock crossed by virtue of Archie's law and as a function of a geometric factor k [m] which depends on the arrangement of the quadrupole on the ground (Tso et al., 2017). To understand the active resistivity method, it is important to consider Ohm's law, which describes the electrical properties of any medium (Uhlenbrook & Wenninger, 2006). Starting from Ohm's laws [$V = IR$] we know that current (I) is directly proportional to voltage (V) but inversely proportional to resistance (R):

$$I = \frac{V}{R} \qquad (15)$$

Rearranging the above relation, the resistance R (measured in ohms) is given by:

$$R = \frac{V}{I} \qquad (16)$$

The resistance of a cylindrical segment of a conductor is equal to the resistivity (ρ) of the material times the length (L) divided by the area (A):

$$R = \frac{\rho\ L}{A} \qquad (17)$$

In a conductor cable we will have:

$$\rho = R\left(\frac{A}{L}\right) = \left(\frac{V}{I}\right)\left(\frac{A}{L}\right) \qquad (18)$$

In the ground instead:

$$\rho = \left(\frac{\Delta V}{I}\right)k \qquad (19)$$

Where “ΔV” is the measured potential difference (MN), “I” is the current injected (AB) and “K” is the geometric factor dependent on electrode arrangement (ABMN) (Meyerhoff et al., 2014).

In the single rock (Archie's law):

$$\rho = F\ \rho W \qquad (20)$$

Where “F” Formation Factor (lithology) and “ρW” resistivity of water in pores or fractures

Therefore:

$$\rho = \left(\frac{VMN}{IAB}\right)k = F\ \rho W \qquad (21)$$

This is why the electrical method is affected by the lithology and the fracturing and / or imbibition conditions of the rock.

The resistivity meter acts as both a voltmeter (measuring V) and an ammeter (measuring I) and records resistance values (V/I). These resistance values are converted to apparent resistivity values using the formula:

$$\rho a = \frac{kV}{I} \qquad (22)$$

where “ρa” is the apparent resistivity and “k” is the geometric factor which varies based on the geometry of each electrode spacing setup (Alisiobi et al., 2012).

In typical fieldwork, data is acquired as an apparent resistivity value and later, by inversion procedure techniques, interpreted to obtain true resistivity. Before carrying out the electrical resistivity measurement it is important to know the aims and objectives to be achieved through the survey so as to set the choice of the type of configuration to be used in an appropriate manner, obviously also depending on the working context such as the space available and the logistics (Meyerhoff et al., 2014).

The most common configurations in electrical resistivity tomography are generally: Wenner, Schlumberger, Dipole – Dipole and Pole – Dipole (Zhou et al, 2002). Each type of array has its own optimal use in certain geological conditions, based on its sensitivity. Sensitivity is an index of how much a change in the resistivity of the ground affects the measurement of potential and results with this in a relationship of direct proportionality (Zhou et al, 2002). Generally, the Wenner configuration is more suitable for highlighting vertical variations, the dipole-dipole configuration is more suitable for highlighting lateral variations but has a more unfavourable signal / noise ratio, the Schlumberger configuration is a compromise between the previous two and the pole-dipole configuration has a better signal / noise ratio compared to the Dipole - Dipole and also allows to go deeper (Berge & Drahor, 2011).

As shown in figures 19 and 20, in the different configurations A and B are current electrodes and M and N are potential electrodes. The constant “a” is the distance in metres between the potential electrodes and the parameter “n” is the factor which multiplies “a” in the current-to-potential electrode distance. In the pole-dipole device, the current electrode designated as ∞ means that the electrode B is located very far

from the dipole MN (at least a distance equivalent to 3 times the largest size of the device and perpendicular to it) (Tsourlos et al., 2011).

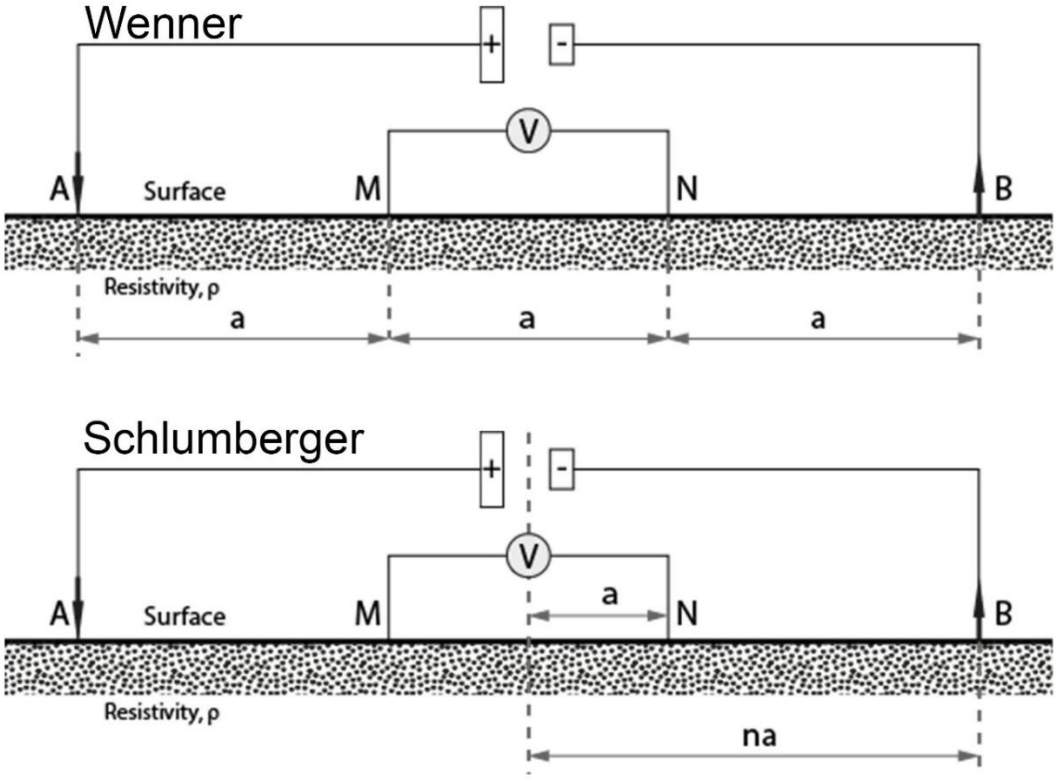

Figure 19: *Most common configurations (Wenner and Schlumberger) in electrical resistivity tomography. "AB" is the electrode pair of current, "MN" is the electrode pair of potential, "I" is the intensity of the current introduced and V is the potential difference (Musset & Khan, 2003).*

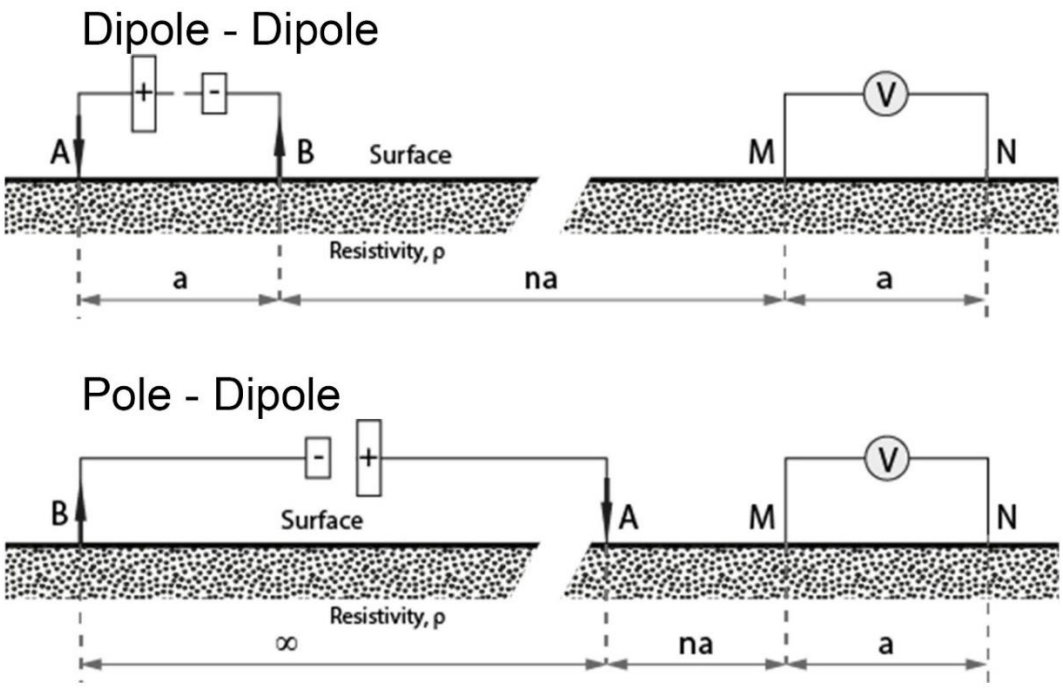

Figure 20: *Representation of the less common dipole-dipole and pole-dipole configurations.*

4. Combining geomatics and geophysical methods for monitoring coastal cliff retreatment in the Selmun promontory (north-eastern coast of Malta)

The content of paragraphs 4.1 to 4.3 has been published in a peer review journal. The full paper is available at this link: https://link.springer.com/article/10.1007/s12665-021-09846-6 (Colica et al., 2021).

4.1 Geological and geomorphological setting of the study area of Selmun

The Maltese archipelago is situated in the Central Mediterranean and it is composed of three main islands (Malta, Gozo, and Comino). It is located about 300 km north of the African coast and about 100 km south of Sicily, in the Sicily channel, which is characterized generally by sea depths of not more than 200 m. The islands are formed of a sequence of five main geological marine sedimentary formations consisting of a sequence of limestones, marls and clays ranging from Oligocene to the Pleistocene in age (Fig. 21A, B) (Hyde 1955; Pedley et al. 1976, 1978, 2011; Scerri 2019). The oldest outcropping unit in the islands is the Lower Coralline Limestone (LCL, Oligocene), which consists of biomicrites, coralline and coarse bioclastic sediments with a maximum thickness of 140 m. Overlying this unit is the Globigerina Limestone (GL, Aquitanian-Serravallian), consisting of biomicrite wackestones and marls with a thickness which can locally exceed 200 m. The Blue Clay (BC, Serravallian) covers the GL and is made of grey-green clays with thicknesses up to 65 m. The Greensand is a glauconitic limestone 1 m thick which is only locally present over the BC (Greensand Formation, not reported in the map of Fig. 21). The Upper Coralline Limestone (UCL, Late Tortonian—Early Messinian) is the youngest lithological unit and is made of the coral-algal patch reef.

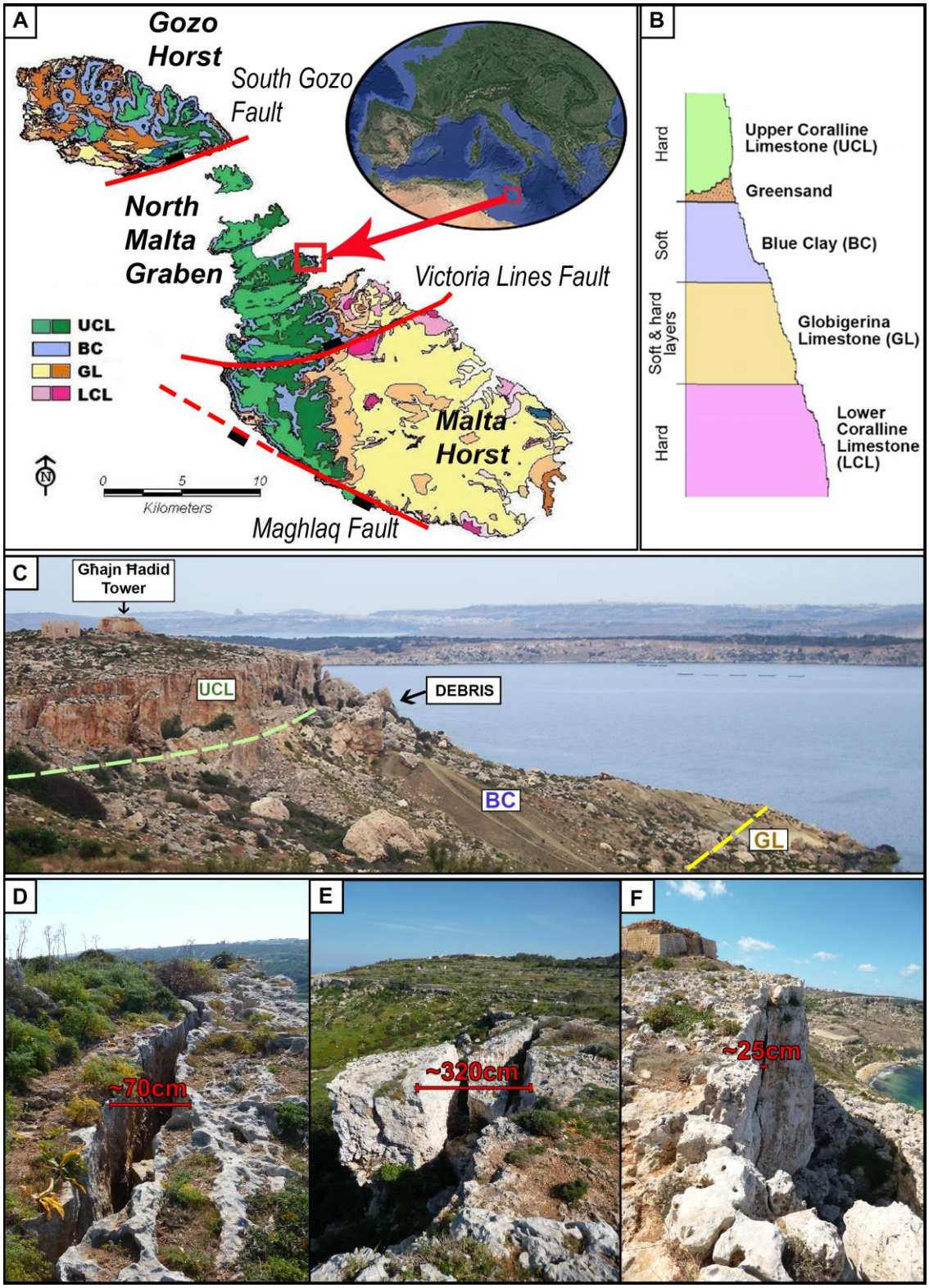

Figure 21: *(A) The position of the Maltese islands in the Mediterranean Sea and the location of the Selmun Promontory (red square) on the Geological map (modified from Oil Exploration Directorate 1993); (B) the sedimentary sequence in the Maltese archipelago; (C) photograph showing the Upper Coralline Limestone cliff, the Upper Coralline-Blue Clay and Blue Clay-Globigerina geological contacts and the UCL debris covering the BC slope; (D–F) images of Selmun fractures and their size (Colica et al., 2021).*

Tectonically, the archipelago forms part of an intensely faulted platform stretching to eastern Sicily, which also represents an important benchmark separating the western and eastern Mediterranean basin (Pedley 2011). In such a context, the islands of Malta can be divided into three main structural regions (Pedley et al. 1976, 1978; Scerri 2019): the Malta Horst, the North Malta Graben and, in the island of Gozo, the Gozo Horst (Fig. 21A). The Malta Horst and the North Malta Graben are separated by the WSW-trending Victoria Lines Fault (also known as Great Fault), a 14-km-long escarpment in the central part of Malta which represents the most prominent morphotectonic lineament. While to the south of this fault the landscape is relatively flat and the outcrops are dominated by the deeper lithological units, in the northern part the structural setting is characterized by a distinctive sequence of ridge-trough morphology where the entire sedimentary sequence is outcropping. This morphology is controlled by an ENE-trending horst and graben structural style which also has a strong influence on coastal landforms. Grabens form valleys which end in bays and coves, while horsts form plateaus ending on lowland coasts or in cliffs, where the different geomechanical and hydrogeological properties of the hard limestones (UCL) overlying the clays (BC) favour the occurrence of a series of geomorphological processes. Particularly impressive are the lateral spreading phenomena, which may evolve into block sliding, rock falls and topples (Devoto et al. 2012, 2013, Mantovani et al. 2013). This thesis investigates the Selmun area which is located along the north-eastern coast of Malta where the geological succession is characterized by the overlapping of the stiff UCL on the soft BC. The stratigraphic succession of the Selmun promontory (Iannucci et al. 2017, 2018) consists of about 20–30 m of the UCL and about 50 m of the BC overlying the GL formation (Fig. 21C) with slightly NE-dipping strata (< 5°). On the gentle slope, the observed debris is mainly composed of detached UCL clasts with diverse sizes ranging from centimetre-scale clasts up to metre-size blocks which are embedded in weathered BC and residual material of limestone dissolution. The largest blocks are generally distributed in the region close to the UCL and deposits can reach several metres of thickness. The Selmun promontory can be considered as a coastal slope in general not directly affected by sea erosion, the instability being mainly controlled by gravitational processes (Martino & Mazzanti 2014). The overlying UCL limestone on the BC formation leads to a lateral spreading phenomenon (Goudie 2004; Panzera et al. 2012; Galea et al. 2014) which

shapes a plateau of stiff rock bordered by jointed unstable cliffs, favouring the detachment of rock blocks and boulders mainly controlled by gravity-induced instability mechanisms (Fig. 21C). This process is accelerated along the coast by weathering effects and marine processes. This landslide process can be defined as a complex phenomenon (e.g.,Varnes 1978; Hutchinson 1988). As shown in the Figs. 21D–F, in the Selmun area, fractures in the topmost part of the plateau range from a few to tens of centimetres wide, depending on the stage of their evolution.

4.2 Introduction to the digital geological survey

Photogrammetry is the technique to build measurable three-dimensional models by using a large number of photographs acquired through a single (or multiple) standard camera for close-range targets. We can refer to digital photogrammetry as Structure from Motion (SfM), which is based on Computer Vision (CV) algorithms that extract the significant points from individual photos, deduces the photographic parameters and matches the recognizable points on multiple photos, detecting the coordinates in the space of the points themselves (Westoby et al., 2012). The SfM only concerns the first part of the image processing methodology (image matching and sparse reconstruction), while in the second phase, which is called Multi-view Stereo Reconstruction (MVS), the low-density point cloud is thickened by increasing the number of points (dense reconstruction) (Wenzel et al., 2013). In aerial digital photogrammetry, the camera is generally installed on Unmanned Aerial Vehicles (UAVs), aeroplanes, or satellites (Li et al., 2003). The recent advancements both in terms of technology and software developments have given a boost to such applications in several fields (e.g. Colica et al., 2017; D'Amico et al., 2017; Galea et al., 2018; Remondino et al., 2011; Casella et al., 2017; Menegoni et al., 2019; Westoby et al., 2012). Primarily, photogrammetry has been used in geosciences for the reconstruction of landforms; for example, digital elevation models (Fonstad et al., 2013), topographic and surface models (Heng et al., 2010), and geomorphological investigations (Chandler, 1999; Lane, 2000; Grosse et al., 2012; Menegoni et al., 2019; Wu et al., 2018).

In the last few years, the use of photographic data acquired by UAV has grown significantly. This is not surprising, since UAVs equipped with a photographic sensor are

relatively low-cost, especially when compared to Lidar equipment and/or aircraft photogrammetry. UAV investigations coupled with a Differential *Global Navigation Satellite System* (DGNSS) and a powerful computer can produce an output with an average accuracy better than 2 cm (Gonçalves et al., 2015) and they allow rapid investigations on large areas. UAV photogrammetry also has some limitations such as: (i) accessibility to the areas in which to place the markers to be measured with the DGNSS; (ii) visibility, as photography records everything visible from the camera lens in the visible and near infrared spectrum; (iii) weather conditions, as it is not possible to fly the drone in strong winds or thunderstorms. Engineering geologists generally utilize expertise that requires knowledge in soil and rock mechanics, groundwater, and surface water hydrology. This expertise can be certainly complemented by photogrammetry and remote sensing techniques which are relatively low-cost and allow the collection of a large amount of valuable data in a small amount of time. Digital photogrammetry, if combined with geological and geotechnical data, can improve the characterization and understanding of landslide mechanisms, which affect, for example, coastal areas (Fazio et al., 2019), urban areas (Laribi et al., 2015) and quarries (Francioni et al., 2014), and therefore help to define mitigation solutions. In this work, we have experimented with UAV photogrammetry to investigate whether it could be accurate enough to replace and/or implement current in-situ engineering-geological surveys. In particular, in this research, it was used an alternative approach that combines photogrammetric models to perform three-dimensional fracture trace and conventional two-dimensional fracture trace mapping in a semi-automatic way.

The traditional engineering-geological rock mass characterization (Barton, 1978), with the stereographic projection of the spatial geometry of the main structures, is often laborious because data are collected manually and sometimes one finds oneself working in dangerous environments. Moreover, the completeness of the acquired data often depends on the time spent in the survey and on the accessibility to the outcrops.

In this study, results from the digital photogrammetry approach are discussed and compared with findings from a traditional engineering-geological survey conducted in the Selmun Promontory area by Iannucci et al. (2017, 2018). In the near future, thanks to the improvement of both technology and processing techniques, the application of

UAV photogrammetry will enhance geological surveying in terms of noticeably reducing data acquisition times, while increasing data quality and completeness.

4.3 Structure from Motion data collection, processing and digital geological survey method

In recent years we have been witnessing the widespread use of low-cost, increasingly high-performance Unmanned Aerial Vehicles, or UAVs, equipped with a large number of sensors capable of extracting detailed information on several scales and in an immediate manner. This study was motivated by the need to perform a geological survey in an area with difficult physical access, and to compare the results with those from conventional surveys. Here we used a Multirotor UAV equipped with a high-definition RGB camera and the Structure from Motion digital photogrammetry technique to reconstruct a three-dimensional model of the Selmun Promontory, located in the northern part of the island of Malta (central Mediterranean Sea). In this area, the evident cliff retreat is linked to landslide processes involving the outcropping geological succession, characterized by the over position of stiff limestones on ductile clays. Such an instability process consists of a lateral spreading associated with toppling and fall of different-size rock blocks.

Starting from the 3D model obtained from the UAV - Photogrammetry, a digital geological-structural survey was performed in which we identified the spatial geometry of the fractures that characterize the area of the Selmun Promontory by measuring strike, dip and dip direction of the fractures with semi-automatic digital tools. Furthermore, we were able to measure the size and volume of singularized rock masses as well as cracks, and their sizes were mapped in a GIS environment that contains a large number of digital structural measures. It is the first application of this type for the Maltese islands and the results obtained with this innovative digital methodology were then compared with those of the traditional field survey of the same area acquired during a previous campaign.

This study demonstrated how the innovation of digital geological surveying lies in the possibility of mapping areas and geological features not detectable with traditional methods, mainly due to the high risk associated with the stability of the cliff or, more

generally, the inaccessibility of some sites, therefore allowing the user to operate in safety and to detect in detail the most remote rocky outcrops.

4.3.1 UAV mission planning and image acquisition

Photogrammetry data were collected using a UAV Phantom 4 Pro equipped with autonomous flight modes, terrain follow mode, obstacle avoidance sensors in 5 directions and 30 minutes flight time. This UAV has a new 3-axis stabilization system for an integrated professional camera with a 1'' Exmor R CMOS image sensor (El Gamal & Eltoukhy, 2005) and a resolution of 20 Megapixels. The first phase of the fieldwork was that of the survey planning which consists of the choice of flight area, flight altitude, camera settings, positioning of the markers on the ground, and topographic measurements to support the aerial-photogrammetric survey.

The final resolution of the model depends upon the overall quality of the acquired images, while the metric accuracy depends on the positioning of the Ground Control Points (GCPs). For this reason, we have carefully designed the GCPs with high-contrast pattern shapes (Fig. 22) that have allowed us to precisely locate the central points seen in the photos.

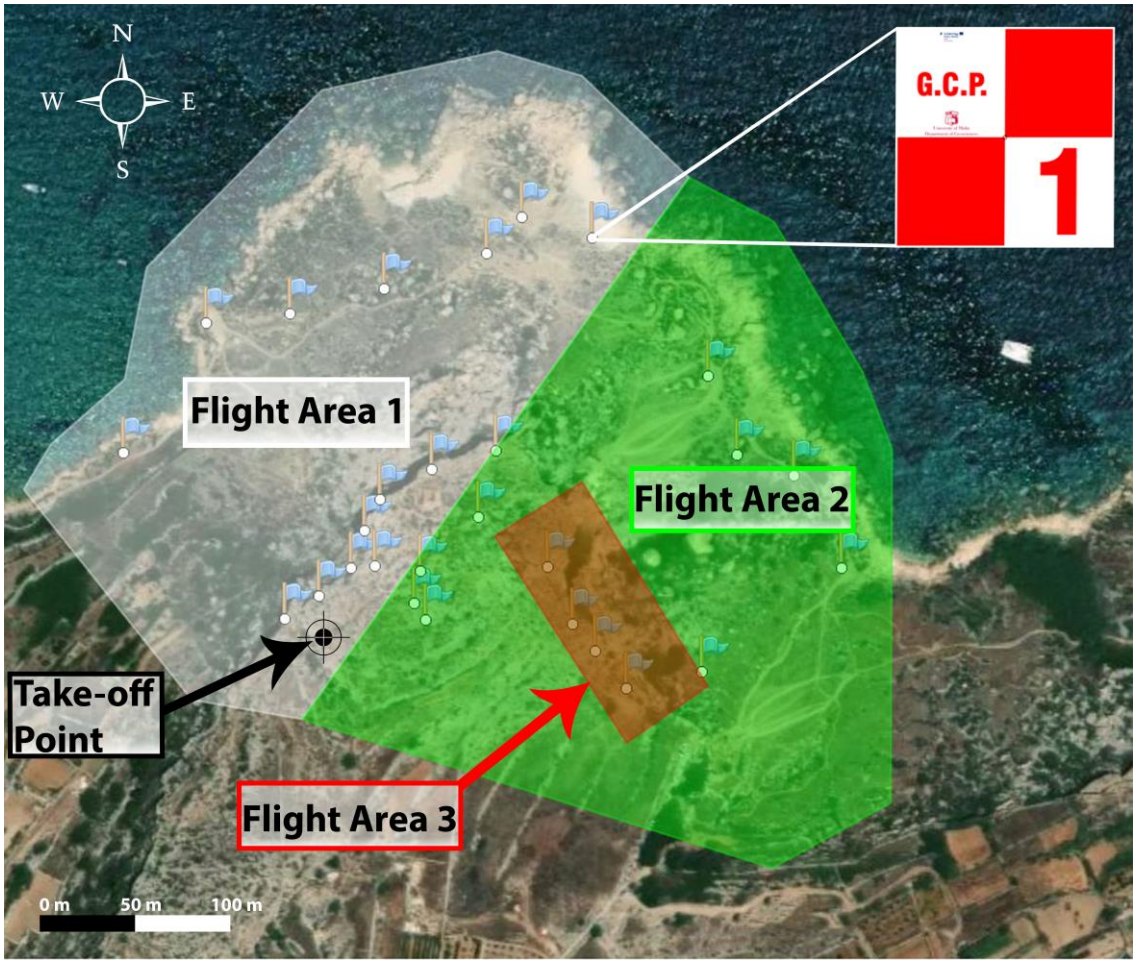

Figure 22: *Satellite image (Retrieved from https://planet.openstreetmap.org) of the Selmun promontory showing areas of the two flight plans in autonomous mode (flight 1 white area and flight 2 green area) and area 3 (in red) detected in manual flight mode 15 m from the target surface. The take-off point is indicated by a black crosshair and the locations of the Ground Control Points (detailed in the upper right corner) are represented by the blue flags (Colica et al., 2021).*

In the planning phase, it is very important to define the Ground Sample Distance (GSD) which represents the distance between the centres of two consecutive pixels expressed in territorial units (Leachtenauer, 2001). The GSD depends on the geometric characteristics of the camera (sensor size and focal length used) as well as the height of flight. For autonomous flight planning, the free app Pix4D Capture (Pix4Dcapture, 2018) was used and, considering the extension of the promontory, it was decided to divide the mission into two flights with a height of 30 m above the take-off point on the plateau (Fig. 22).

The recommended overlap values for aerial photogrammetry are at least 80% forward overlap and at least 70% for side overlap (Agisoft, 2021). In our survey, to obtain high

accuracy, the images were taken from a nadir-looking direction with a 90% forward overlap and 70% side overlap.

The GSD has been automatically calculated by the app because it contains in its database all the technical data related to the camera of the UAV. At 30 m of distance, this resulted in an estimated GSD of 0.87 cm per pixel. A third flight was also carried out in manual mode on the area already covered by the first flight but in this case, we acquired images with more detail on the cliff and on the large block of rock located southeast of the study area (Fig. 2) obtaining an estimated GSD of 0.44 cm per pixel. This was possible by using the proximity sensors of the Phantom 4Pro that allowed us to maintain a constant distance of 15 m from the framed subject and the images were acquired at an angle of 45° to avoid the systematic distortions which can occur with a fixed camera orientation (James and Robson, 2014). The averaged GSD of the orthomosaic is finally estimated within the photogrammetric software, where the average distance from the cameras to the sparse cloud points is calculated.

For the whole flight area of 132,575 m², 28 markers were placed on the ground at different altitudes and the relative spatial coordinates were detected through the use of two Topcon HiPer HR DGNSS receivers in Base + Rover configuration capable of horizontal accuracy of 3 mm $\pm$ 0.1 part per million and a vertical accuracy of 3.5 mm $\pm$ 0.4 part per million. This was done to ensure a high-quality output model with accurate georeferencing. In total over 1677 photos were acquired during the three flights and more details are reported in Table 2.

Table 2: *Summary of some fundamental parameters defined in the planning phase of the three flights aimed at the photogrammetric survey (Colica et al., 2021).*

	Flight height in meters from the take-off point	Distance in meters between the camera and the target	Number of images taken	Area covered per scene in square meters	Images resolution in pixels	Main images overlap
Automatic Flight 1	30	30 to 100	670	65603.5	5472 x 3648	90% forward and 70% side
Automatic Flight 2	30	30 to 100	689	66971.5	5472 x 3648	90% forward and 70% side
Manual Flight 3	5 to 30	15	318	6705.7	5472 x 3648	About 90% forward and 90% side

4.3.2 Structure from Motion processing

Modern photogrammetric software packages implement the Structure from Motion (SfM) algorithms, which arise from traditional photogrammetry and have evolved thanks to the implementation of Computer Vision algorithms (Ma Y. et al., 2012).

The theoretical principles of collinearity, the intersection of projective rays and calibration of the camera, are flanked by the typical algorithms of computer vision that allow to analyse and correlate digital images in a fast and automatic way (Szeliski, 2010).

There are many Structure from Motion (SfM) software packages, one of the most popular being Agisoft Metashape Professional (Agisoft, 2021), which was used in this study.

The preliminary phase of image processing is the creation of the project in Agisoft Metashape and the import of photographs. Within the same project, we created 2 chunks of images: the first with the images acquired at 30 m above the take-off point during flights 1 and 2, and the second chunk with the images acquired at a distance of about 15 m from the target area of the cliff face during flight 3 in manual mode. The processing procedure includes four main steps before obtaining a complete 3D model (Fig. 23).

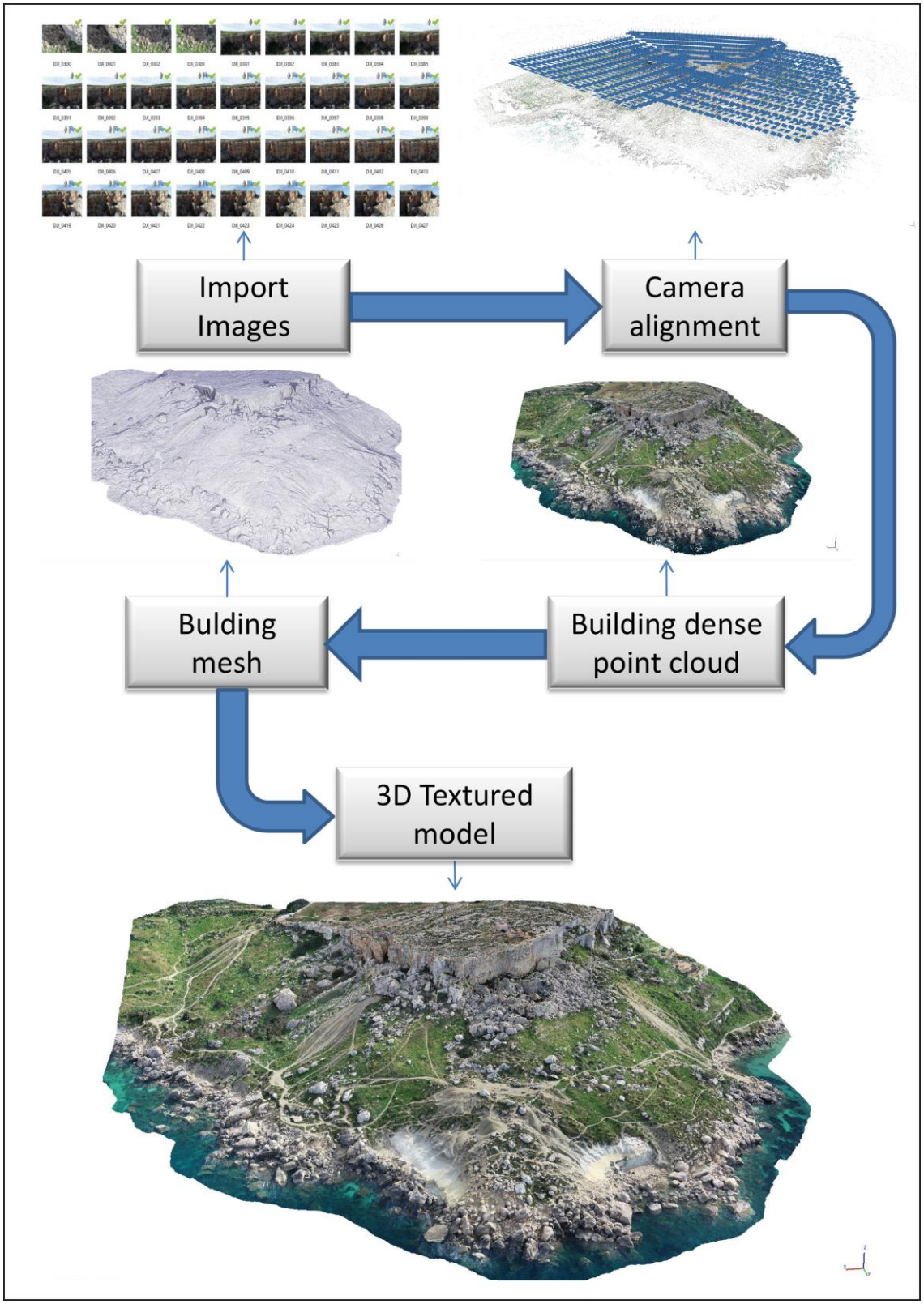

Figure 23: *Photogrammetric workflow using Agisoft Metashape software (Agisoft 2021) (Colica et al., 2021).*

The first phase of processing is the alignment of the camera which serves to correctly position the images with respect to each other or, if they are already geolocated, to

calculate the exact position in real space. At this stage, the software generates a sparse point cloud and it is possible to insert the GNSS coordinate on the ground control points visible in the pictures to improve the accuracy of the model. In our case, very high accuracy was reached, with an estimated Root Mean Square Error (RMSE) at the check points of 1.14 cm.

The second phase involves the building of a dense point cloud on the estimated camera positions. The dense cloud of points can be modified and classified before proceeding to the generation of the 3D mesh model.

The third stage is the reconstruction of a 3D polygonal mesh representing the object's surface based on the dense point cloud. After the mesh geometry is reconstructed, it is textured and used for georeferenced orthomosaic and DEM generation (Table 3).

Table 3: *Summary of the parameters related to orthomosaic and DEM generated by the image processing in Agisoft Metashape (Colica et al., 2021).*

	Resolution	**Point density**	**Size in pixels**	**Coordinate system**
Digital Elevation Model	5 cm/pix	400 points/m²	18,741 x 12,862	WGS 84 / UTM zone 33N (EPSG::32633)
Orthomosaic	1.3 cm/pix*	N/A	36,127 x 34,047	WGS 84 / UTM zone 33N (EPSG::32633)
*averaged Ground Sampling Distance of the orthomosaic estimated within the photogrammetric software in which the average distance from the cameras to the sparse cloud points was calculated				

4.3.3 Digital geological survey method

The progress made in the last years in the development of the UAVs and the implementation of the SfM algorithms in the new software allows us to acquire detailed multiscale information, such as the semi-automatic joint sets identification (Buyer et al., 2020; Li et al., 2019), at low cost and in a reasonable processing time. In this study, it was used open-source software with plugins specially designed to quickly interpolate the structural features between the points, defined manually, in the dataset of the 3D model, orthomosaic, and DEM.

Starting from the 3D model of the Selmun promontory, in order to decrease the computation time during the post-processing analysis, we divided it into three smaller models. From now on, these models will be referred to as Digital Outcrop Models (DOMs).

To analyse the DOMs we used the structural geology "Compass" plugin (Thiele et al., 2017) installed in the 2.10 version (CloudCompare, 2018) of the open-source software CloudCompare (Girardeau-Montaut, 2015). It combines a set of flexible tools for geological interpretation that enable computerized digitization and measurement. The tools contained in the Compass plugin and used in this study are two: "Plane" and "Trace".

The Plane tool serves to measure the orientations of outcropping planar structures, such as joint surfaces. With this tool, it was possible to adapt a plane to a minimum of 3 points (with x, y, and z coordinates), and automatically determine the orientation of the surface. This was done using the least squares method (Fernández, 2005) in which the Plane tool calculates a better fit plan through a planar regression of data that provides a medium orientation for sets of more than three points. In the 3D point clouds of the Selmun Promontory, we selected over 80 sets of points, corresponding to the fractures (e.g. Sturzenegger and Stead, 2009; Menegoni et al., 2019), on which a plane was constructed that gave us the surface orientations (dip / dip direction). The Trace tool allows to digitize and measure traces and contacts. The operation of this tool is very intuitive. Selecting a start and end point along a fracture, the tool reconstructs the path, finding the trace that connects these points and reconstructing the best-fit plane to estimate the orientation. The reconstruction of the fracture path depends on the cost function used by the least-cost path algorithm (Collischonn & Pilar, 2000). The cost

function called Darkness was the most effective for the construction of tracks in our 3D point cloud, as they follow the dark points representing the shadows present in the fractures.

Other cost features that can be selected in this tool are lightness (the traces follow the light points in the cloud), RGB (the traces avoid colour contrasts, following points with a colour similar to the initial and final points), curvature (the tracks follow the points on ridges and valleys), gradient (traces follow colour limits such as lithological contacts), distance (the tracks follow the shortest route), scalar field (the tracks follow the low values in the active scalar field), and reverse scalar field (the traces follow high values in the active scalar field) (Thiele et al., 2017).

Another useful tool for semi-automatic fracture digitization is the GeoTrace plugin that we installed in the free and open-source geographic information system QGIS (QGIS, 2015). GeoTrace allows to analyse and extract the orientations of geological structures and can be used to quickly digitize structural traces in raster data, estimate their 3D orientations using an associated DEM and then display the results on stereonets and rose diagrams (Thiele et al., 2017). The high-resolution georeferenced orthomosaic (1.3 cm / pixel) obtained from the photogrammetric process was imported into QGIS and transformed into a single-channel cost raster. This operation is fundamental because the plugin uses a least-cost path algorithm to follow the linear features present in the orthomosaic. Thanks to these semi-automatic systems we were able to trace and extract all the fracture models visible both from a 3D model and from orthomosaic in much less time than we would have used with a manual operation.

4.3.4 Digital geological survey results

The Selmun case study highlights the potential of the Digital Geological Survey to provide quantitative measurements starting from a 3D model by aerial photogrammetry. The outputs obtained from the photogrammetric survey are summarized in Figure 24, where a three-dimensional digital model of the entire study area is shown from different viewpoints and represents the basis on which the digital geo-structural analysis took place. From the 3D model, it was created a Digital Elevation Model (DEM), in which it was possible to identify the variation in altitude between 0 and 70 metres through the scalar field with colour bar (Fig. 24E) and georeferenced

orthomosaic (Fig. 24F) in which the joints were digitalized in a semi-automatic way and plotted in terms of strikes on a rose diagram (Fig. 25A). From the 3D digital photogrammetric model, it is possible to measure the thickness of the UCL, which in the area has an average value of 25-30 m. Furthermore, the overall thickness for the BC formation was estimated in about 50 m. From a Digital Geological Survey, performed on the DOMs, traces, contacts and orientations of joint surfaces were measured (Fig. 25B). The results of the joint attitude at the Selmun Promontory were plotted to identify the main joint systems (Fig. 25C).

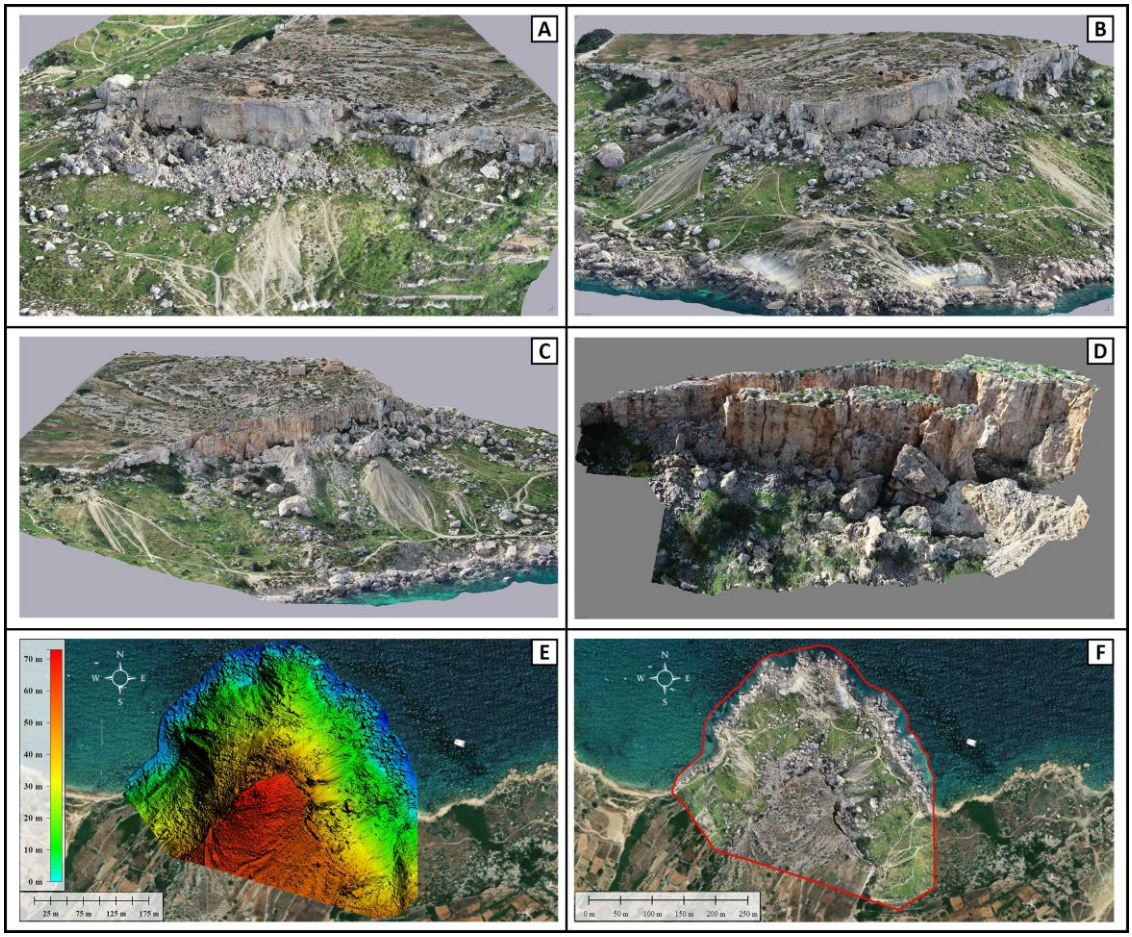

Figure 24: *Screenshots of the 3D model with exposure to North-West **A**, North **B**, North-East **C**, and detail of the east area **D** of Selmun promontory reconstructed with drone's images acquired in manual flight mode. **E** Digital Elevation Model and F Orthomosaic of the Selmun promontory obtained from the photogrammetric process and overlapped in Google Earth Pro™ map (Colica et al., 2021).*

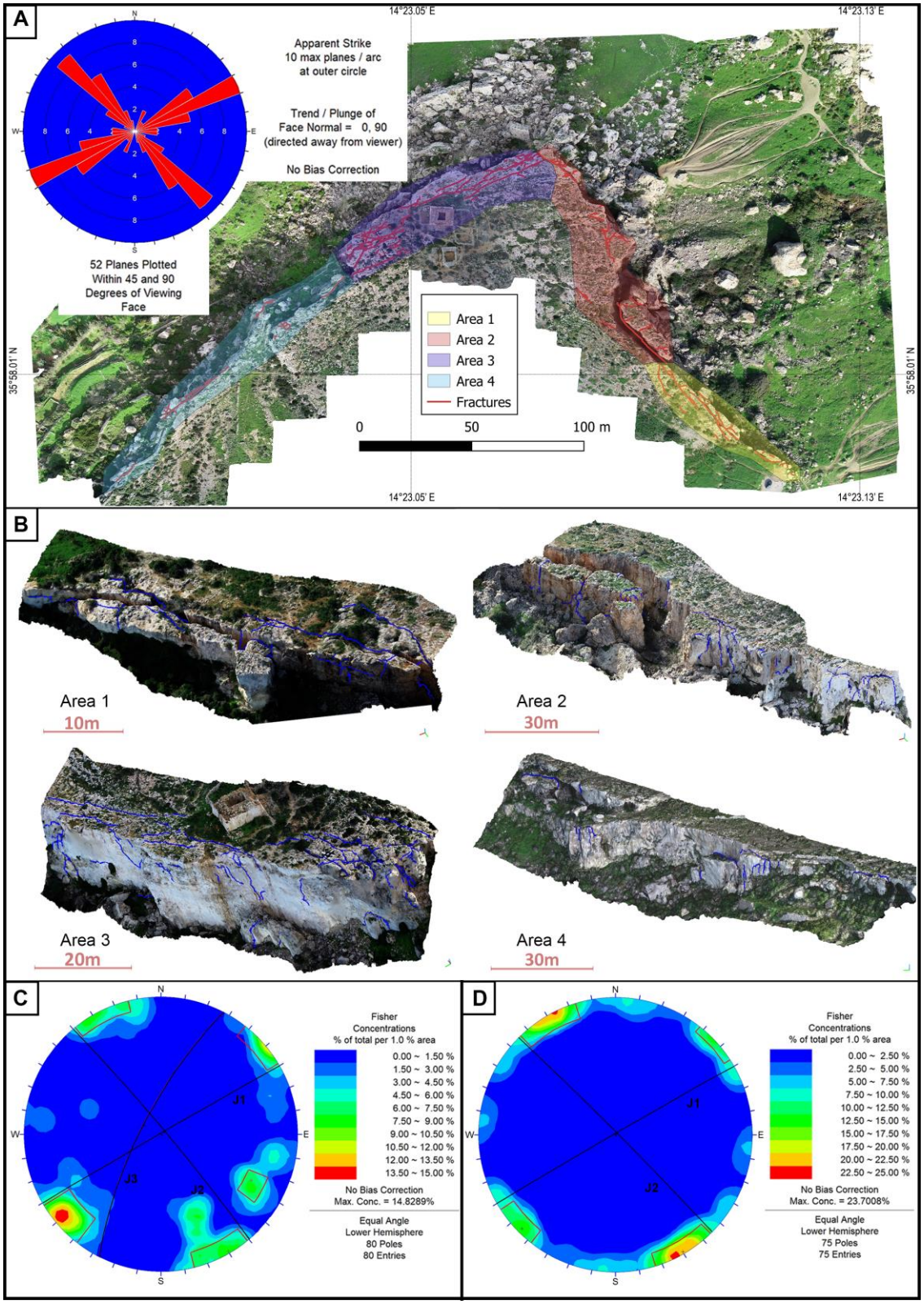

Figure 25: ***A*** *Georeferenced UAV-based orthomosaic of Selmun promontory (Malta) with semi-automatic digitized fractures map derived in a standard GIS environment. A rose diagram of joint planes (in the upper left corner) was extracted from the fractures traced in red on the orthomosaic. Areas highlighted by polygons show the positions of the four Digital Outcrop Models (DOMs).* ***B*** *Oblique view of DOMs constructed from aerial-photogrammetry in which fractures, highlighted in blue, have been digitized in 3D.*

Comparison of joint survey results on the Selmun promontory: ***C*** *Stereographic projection (equal-angle lower-hemisphere) of joint poles obtained by the raster and 3D model analysis and planes of the three main systems;* ***D*** *Stereographic projection (equal-angle lower-hemisphere) of joint poles obtained by in situ engineering-geological surveys (Iannucci et al. 2018) and planes of the two main systems (Colica et al., 2021).*

The high number of measurements of the joint orientations in the DOMs provides a much more reliable description of the geometry of the fractures than the orientation at a point traditionally measured with the compass in the field. This is likely to occur because the point orientation estimates acquired with a compass are not representative of large-scale orientation. On the 3D dense cloud, the orientation of the structure on large areas can be averaged, and this is difficult to obtain using traditional methods. In fact, most of the measurements made on the DOMs of the Selmun Promontory are in places with reduced accessibility or even totally inaccessible. Computer-assisted digitization, able to speed up the digitization process up to 69% compared to traditional manual methods (Thiele et al., 2017), was fundamental in this study to manage the large number of measurements performed on the 3D model. Using this technique, it was also possible to measure and analyse parts of the cliff otherwise impossible to reach by an operator. The results of the joint attitude at the Selmun Promontory obtained by the two different approaches [i.e. digital with orthomosaic and DOMs analysis (Fig. 25C), and manual with in-situ engineering-geological surveys (Fig. 25D)], were plotted separately so that any differences in the identified main joint systems could be observed. As already noted by Iannucci et al. (2018), the stereographic projection (equal-angle lower-hemisphere) of the joint poles surveyed by in-situ engineering-geological investigations defines two main systems of sub-vertical joints at the Selmun Promontory (Fig. 25D): J1 with a mean dip direction of 330° (strike 60° or 240°) and mean dip of 89°, prevalent in the NW zone, and J2 with mean dip direction 45° (strike 135° or 315°) and mean dip of 88°, prevalent in the SE zone. A similar result can be observed by studying the stereographic projection of the joint poles identified by the raster and DOMs analysis (Fig. 25C). This analysis confirmed the presence of the two above-mentioned main systems of sub-vertical joints: J1 having mean dip direction of 330° (strike of 60° or 240°) with mean dip of 89° and J2 having mean dip direction of 50° (strike 140° or 320°) and mean dip of 86°. The difference of 5° in the dip direction of J2

is not significant and could be attributed to the different datasets of joints analysed. In addition, a third joint system resulted from studying the pole distribution: J3, with a mean dip direction of 297° (strike 27° or 207°) and a mean dip of 73°, therefore not sub-vertical as the other two joint systems. The failure to detect this joint system by the in situ engineering-geological surveys could be explained by the inability to investigate the UCL cliff walls, which was only possible through analysis of the UAV-photogrammetric model. The diagram obtained by the plotting of DOMs measurement (Fig. 25C) confirmed the results of the in situ engineering-geological surveys. In fact, it was observed the presence of two main joint systems on the Selmun Promontory: a first system (31% of frequency) having a strike of 50°-70° (or 230°-250°), that has an attitude similar to the previously-defined system J1, and a second system (29% of frequency) with a strike of 130°-150° (or 310°-330°), that can be referred to the system J2.

Finally, as a further output, a high-resolution geomorphological map (Fig. 26) was created, starting from DEM and orthomosaic generated by aerial photogrammetry. This map illustrates the geology of the study area and contains a digital repository of main geomorphological features such as the main fractures and boulders.

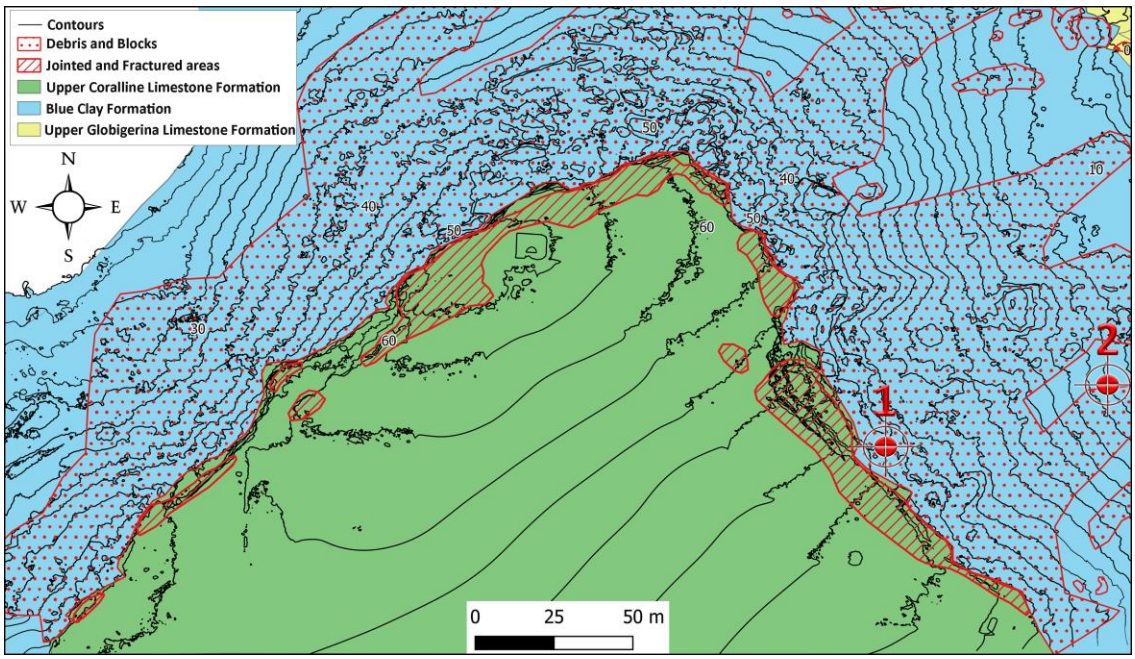

Figure 26: *Geomorphological map of the Selmun Area (Malta) in GIS platform (scale 1:2500) and the two points where ambient noise measurements were recorded (red dots 1 and 2) (Colica et al., 2021).*

4.4 Electrical Resistivity Tomography (ERT) investigations

In Selmun it was used digital photogrammetry technique to reconstruct a 3D digital model of the area with the main goal of monitoring and studying the retreating process of the cliff and the landslide phenomena which are closely linked to the local geological and geomorphological conditions. In order to identify the vertical fractures not visible from the surface affecting the Selmun plateau have been performed electrical resistivity tomography (ERT) which is an active geophysical method capable of measuring both lateral and vertical variation in ground resistivity. In general, the measure of resistivity of the ground is affected by several factors such as pore spaces in rock particles, joints or fracture openings etc. The degree of water saturation and content can also influence the resistivity of rocks.

In this technique, a high number of electrodes are used which are used each time as A, B, M and N, creating a large dataset of quadripole measurements, in a large number of possible configurations, varying the depth of investigation without moving the electrodes. This type of geoelectric prospecting leads to the construction of an image of the subsoil in terms of electrical resistivity which is obtained by means of an operation called tomographic inversion.

The analysis of the geoelectric characteristics of the subsoil of the Selmun promontory, in correspondence with two profiles, was carried out by ERT prospecting with the multi-electrode method. This methodology makes it possible to identify the type of materials investigated as a function of the difference in resistance opposed by them to the passage of the electrical flow lines. The acquisition and consequent inversion can be two-dimensional or even three-dimensional (Loke, 2000).

This method is advantageous compared to others because it uses controlled sources but is essentially limited by two factors: a) the penetration depends on the distance between the current electrodes (indicatively between a quarter and a fifth), therefore it is strongly conditioned by the length of the cables, the power of the battery and the conformation of the investigated terrain; b) the resolution is very good near the electrodes and decreases rapidly with the distance from them. In relation to the mutual position of the current electrodes with respect to the potential ones, it is possible to create different types of electrode configurations, among which the most used are the Wenner, Dipole-Dipole and Schlumberger devices (Fig. 20). Of course, the geoelectric

responses of the various configurations are different and can be compared with each other.

The main goals of the electrical tomography studies can be linked to the identification of subsurface fractures and voids and the validation of the geological model of the Selmun promontory that was built using a photogrammetric 3D model. This is expressed, in particular, in the determination of thicknesses and stratigraphic limits of the geological formations involved and in the identification of the contact between the portion of softened clay and the intact one in which it is plausible to expect different resistivity values.

4.4.1 ERT data acquisition

In order to constrain some geological features in the Selmun promontory, and to demonstrate the feasibility of this technique in similar case studies, we performed two electrical resistivity tomography surveys on the promontory.

For this purpose, it was used the multichannel digital georesistivimeter Electra model, from Moho Srl (Fig. 27). This equipment has the particularity of working with alternating current, which gives it a series of its own characteristics, such as its low weight and high portability.

The ERTs were carried out in two different sectors, on the slope of the promontory (S-T profile), almost from sea level to the plateau, and on the plateau (U-V profile) (Fig. 28). The spacing chosen was 5 metres, using 32 electrodes in both cases. The total length of both scans was 155m.

Figure 27: *ERT data acquisition in Selmun (Malta) using a georesistivimeter model ELECTRA, from Moho Srl.*

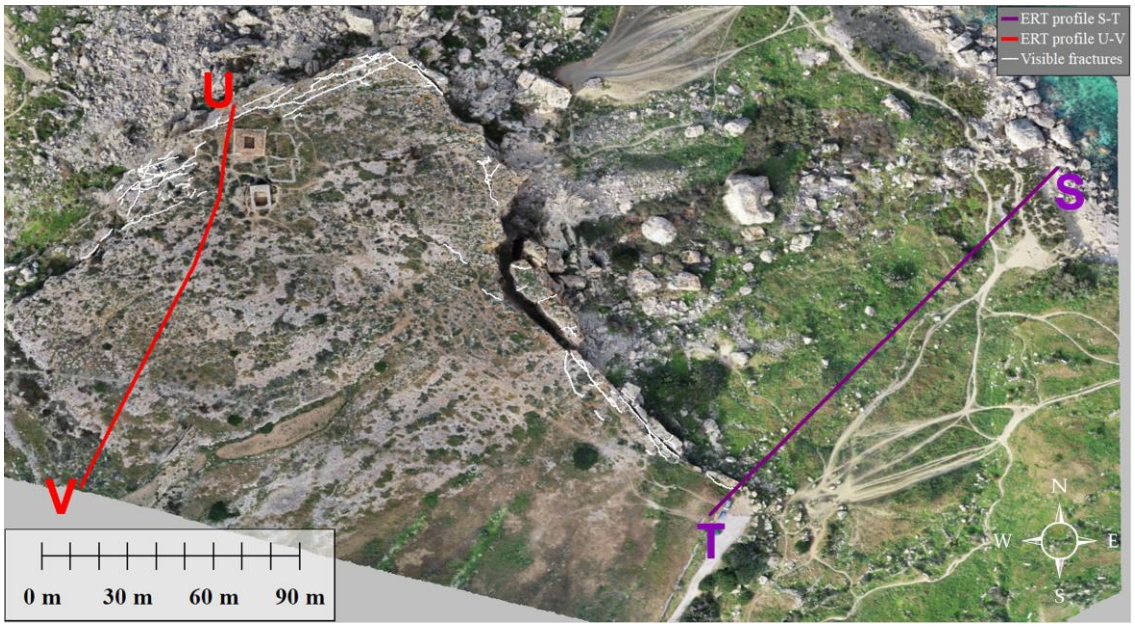

Figure 28: *GIS project with the ERT surveys localization carried out on the Selmun promontory. The fractures visible from the surface are highlighted in white.*

The U-V array was provided with an additional 32 electrodes which, due to a malfunction, did not allow data acquisition. This length would have allowed the achievement of a greater depth of investigation. To check the quality of the coupling between the electrodes and the substrate, impedance measurements were performed on each profile. This measurement is performed between pairs of electrodes. High local

values compared to the average of the pairs indicate a weak coupling of one or both electrodes of the pair. In cases where the impedance values indicated poor coupling, the coupling was improved by means of a salt and water solution, or possibly by replacing the electrodes. The unit of measure for impedance is the ohm (Ω). Correctly coupled electrodes account for a few hundred to a few thousand Ω. Outliers, which require verification of the electrode-soil contact, are greater than a few tens of kΩ (1 kΩ = 1000 Ω). Impedance values measured in the Blue Clay Formation were less than 100 Ohm, while those measured between electrodes arranged in the UCL were a few kOhm (Fig. 29). These differences are to be expected due to the higher resistivity of the limestones compared to the clays.

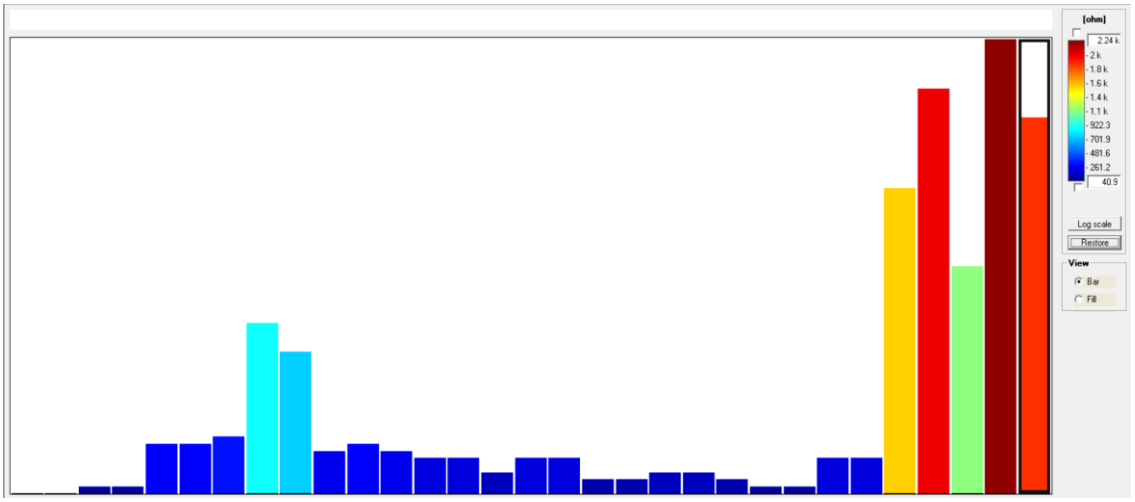

Figure 29: *Impedance values measured in an impedance test on the U-V profile. The pairs of electrodes placed on the Blue Clay Formation show low impedance values (below 100 Ohm), whereas those electrodes placed on the limestones of the UCL Formation show relatively higher values (between 1.15 and 2.24 kOhm), expected for their lithology.*

In each profile, three different configurations were acquired: Wenner alpha, Wenner-Schlumberger and Dipole-Dipole. Due to the different relative positions of the current and potential electrodes in the different arrays, each array is more or less sensitive to the different geometries of the geoelectrical discontinuities in the subsurface.

Since the apparent resistivity values, Rho of the materials are calculated using geometrical factors of the array (K value in equation Rho=R.K), it is important to perform during the data processing a correction of the K factor when the topography is not flat, in order to recalculate the interelectrode distance.

Although the U-V profile was carried out on terrain without major topographic changes, the S-T profile was carried out on a steep slope with a topographic break, so this correction was essential. For this, the position of the electrodes was measured using high-precision differential GNSS (model Topcon Hiperh HR) equipment.

4.4.2 ERT data processing

The acquired data were exported in text format and pre-processed using Prosys III software (IRIS Instruments). In the case of profile S-T, topographic information was added and apparent resistivity values were recalculated (Fig. 30).

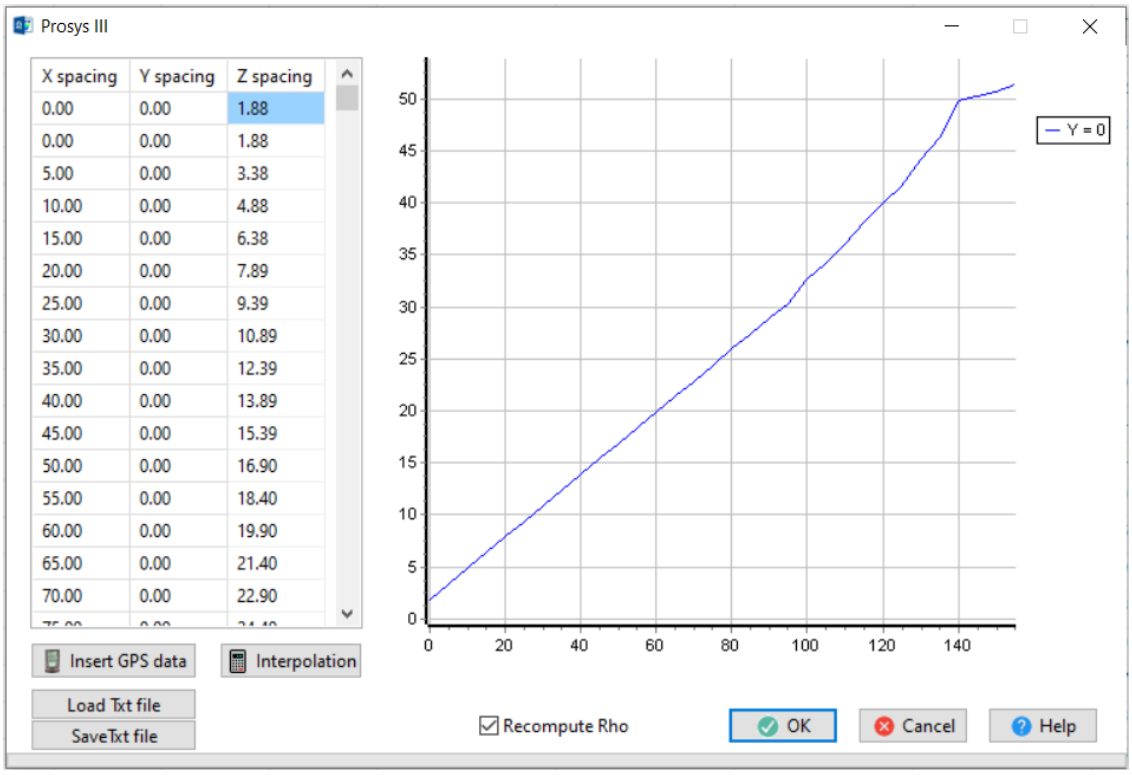

Figure 30: *Adding topography in Prosys software.*

Next, the raw data were displayed and peak points were determined using different display modes offered by the software. Outliers are not uncommon in electrical tomography and can be relays failing at one of the electrodes, insufficient electrode ground contact from dry soil, or cable shorting from extremely wet ground conditions. It is desirable to eliminate them so as not to introduce errors in the calculation of the resistivity model (Fig. 31).

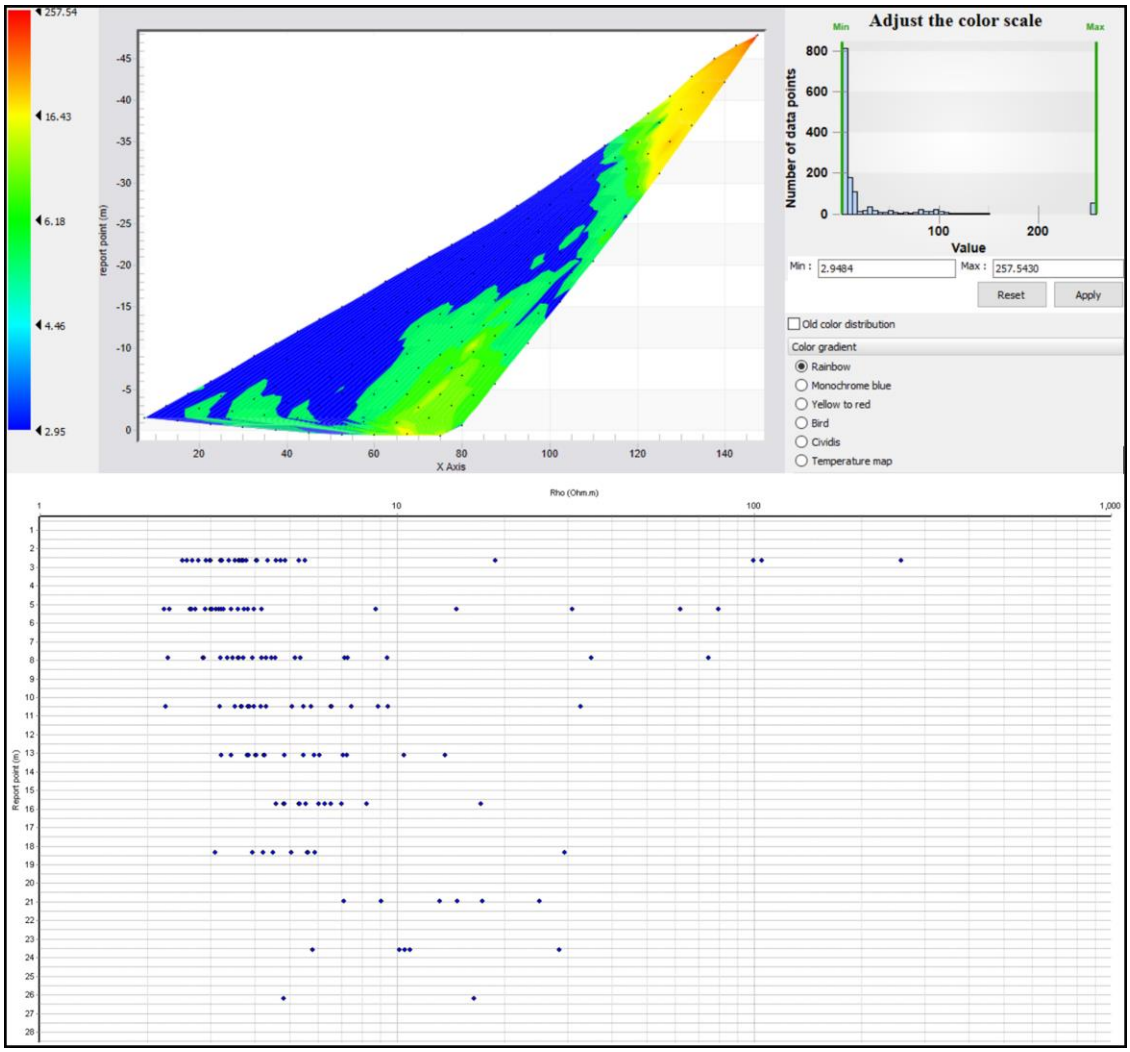

Figure 31: *Display of raw data in Prosys III. Note the possible outlier with Rho value 257 Ohm.m in both representations.*

The resistivity calculated in the field will correspond to the apparent resistivity of the ground and not to the real resistivity. This is due to the fact that the subsoil is generally composed of different materials, so that, the electric field introduced into the ground will affect several layers simultaneously, and the measured resistivity will correspond to an intermediate value of all of them. To obtain a 2-D model of real resistivities from the pseudo section of apparent resistivities calculated with the field data, an inversion program is necessary. An inversion algorithm is required to convert the pseudo section of apparent resistivity derived using the field data into a 2-D model of real resistivity. The foundation of inversion techniques is an iterative process to create a real resistivity model, with the goal of making the generated apparent resistivity model as close as feasible to the pseudo section of apparent resistivity measured in the field.

The inversion of the apparent resistivity data was performed with the aid of the Res2DInv software (Loke, 2018), which applies an inversion algorithm based on the least squares method to produce a 2D resistivity model (Loke & Barker, 1996).

Within this software, it is also possible to pre-process the data and delete outliers values using the “Exterminate bad data points” command in the Res2DInv software. The apparent resistivity data values are shown as profiles for each data level when the "Exterminate bad data points" option is selected Fig. 32. These problematic data points typically have apparent resistivity values that are clearly out of range in relation to the nearby data points and is recommended to delete them before the inversion.

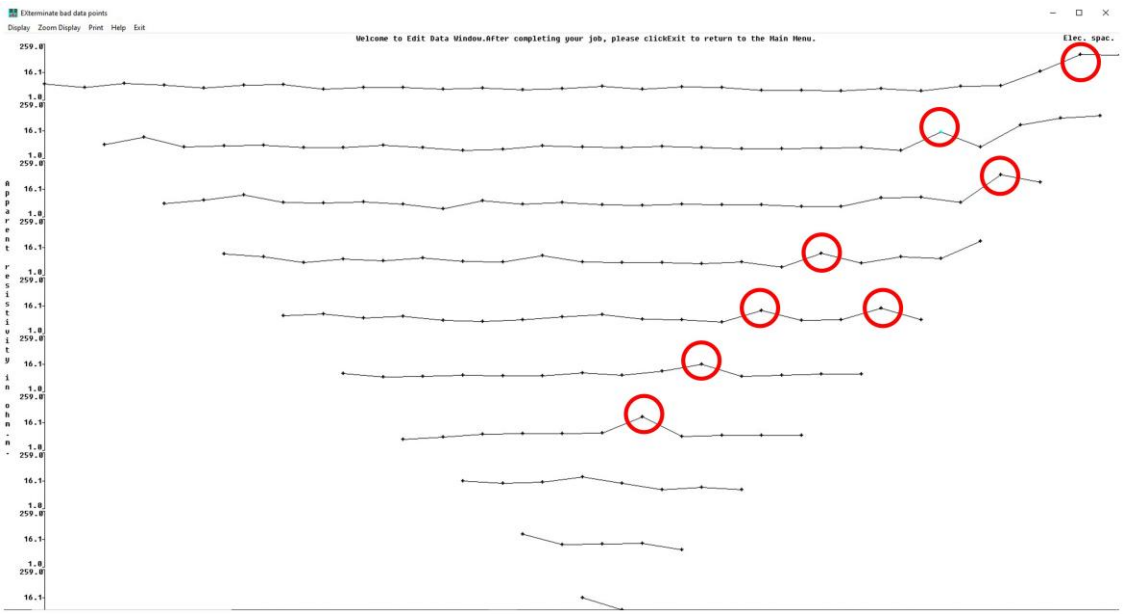

Figure 32: *A sample dataset with some bad data points in red circles.*

Once the bad data had been removed, a new modified file was created and saved with a different name. The default model used by the RES2DINV application has interior model blocks that are the same width as the unit electrode spacing. In most instances, this is effective. When there are significant resistivity fluctuations close to the ground surface, like in the case of Selmun, thinner model cells can produce better results. The width of the model cells can be decreased in one of two ways. The "Use model refinement" option under the "Inversion" menu is the first method. By default, the program will set the width of the model cells to be the same as the unit electrode spacing. If there are very large resistivity variations near the ground surface, it is possible to use a model with narrower model cells. This is particularly important for arrays such

as the pole-dipole and dipole-dipole which are more sensitive to near-surface variations. In general, using a model where the width of the cells is half the unit electrode spacing gives the optimum results. A model with narrower cells frequently results in 'ripples' in the near-surface region of the resistivity model (Loke, 2001).

At this step, it was possible to proceed with the inversion phase through RES2DINV code, the RMS error statistics, sensitivity and a two-dimensional model with topography for the two profiles as shown in the results chapter.

4.4.3 ERT results

The main results obtained by deploying two ERT arrays (S-T and U-V) in the area on Selmun promontory (Malta) are shown below. In particular, from the first array (S-T) we identify the contact between Blue Clay and Globigerina Limestone shown in figure 34. It was also possible to measure the thickness of the BC which varies from 2 m, on the SW front up to about 40 m moving in the NE direction as measured by the 3D model in Colica et al. (2021) and Iannucci et al. (2018). Given the high accuracy of vertical resolution that the Wenner configuration provides, the latter is considered the most suitable data to confirm the stratigraphic limits and thicknesses involved in the S-T profile (Fig. 34). Furthermore, the two-dimensional resistivity model was transposed under the investigated topographic surfaces using data taken with a differential GNSS system. The greatest resistivity values (about 150 Ω m) are observed around 50 m above sea level. and can be attributed to the formation of the Upper Coralline Limestone. Conversely, the portion described in blue (resistivity values of about 5-10 Ω · m) corresponds to the Blue Clay. The contact with the formation of the Globigerina Limestone is attested, as also emerged from the survey of the countryside, approximately in correspondence with the sea level.

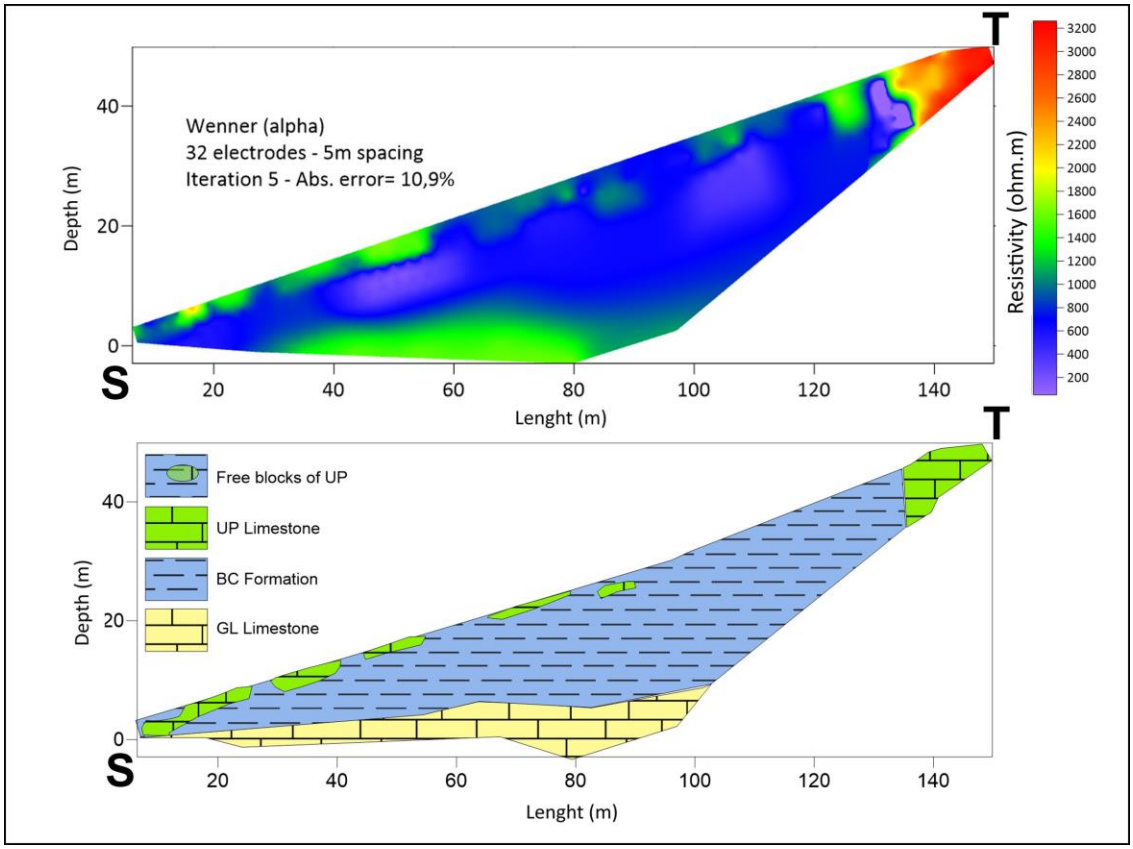

Figure 34: *ERT array (S-T) on the slope of Selmun promontory (Malta) and its geological interpretation.*

The second ERT profile (U-V) represented in figure 35 was acquired above the plateau formed by UCL with Wenner, Schlumberger and Dipole-Dipole configurations. The inverted models show areas with high resistivity which can be attributed to the presence of vertical fractures in the rock and areas with lower resistivity which show the contact between UCL and BL.

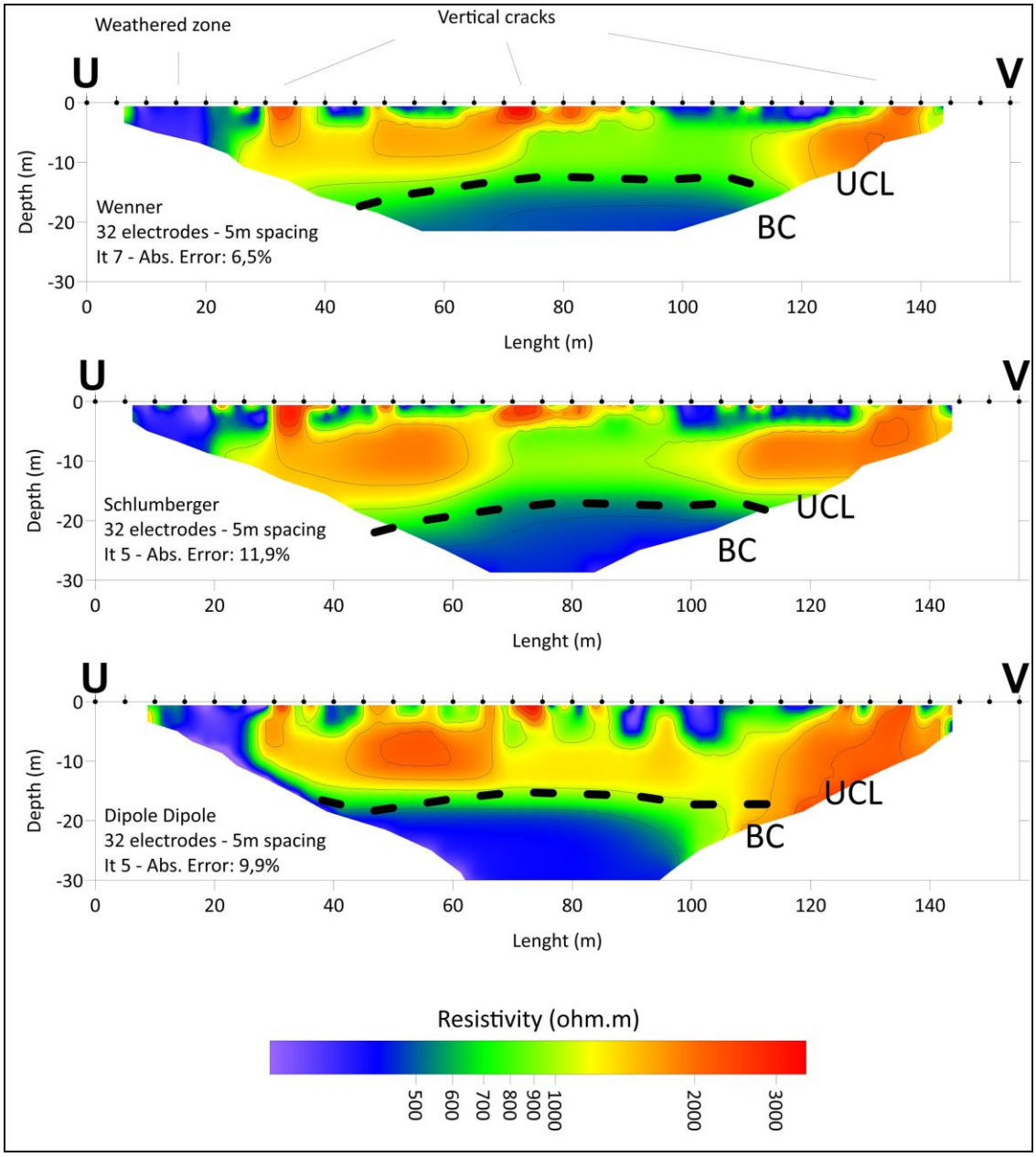

Figure 35: *ERT array on the plateau of Selmun promontory (Malta).*

4.5 Ground penetrating radar (GPR) investigations

Ground penetrating radar (GPR), one of the geophysical prospecting methods, uses high-frequency electromagnetic waves to get high-resolution images of shallow geologic structures, such as faults and fractures (Davis et al., 1989). The adoption of indirect geophysical prospecting methods, such as GPR, ensures repeatability and velocity of acquisition compared to drilling prospecting techniques, as shown in several types of research (Caselle et al., 2020; Colica et al., 2021; Persico et al., 2019). The uses of GPR in the Geological engineering filed have shown how useful this technology is for a variety of technical and environmental issues. In particular, GPR has been used for internal rock structures analysis (Shukla et al., 2013), stability assessment of sea natural arches (Leucci et al., 2021), faults and fractures detection (Ercoli et al., 2013; Grandjean et al., 1996), quarry characterization (Saponaro et al., 2021; Zanzi et al. 2019), tunnel-stability assessment (Cardarelli et al., 2003) and to locate and identify solid waste disposal deposits (Orlando et al., 2001). In this study, a focus has been placed on the use of GPR in the high-resolution characterization of bedrock cracks in order to investigate the presence of vertical fractures underneath the Selmun UCL plateau with additional measurements independent of the ERT.

4.5.1 GPR data acquisition

The GPR system used for data acquisitions is the Cobra Plug-In™ SUBECHO model (RadarTeam AB, Boden, Sweden) (Fig.36), with a central frequency of 70 Mhz. During the acquisition, the GPR system was connected to a topographic GNSS receiver allowing the positioning correction through the differential method (Schönemann et al., 2011). Using the GIS containing all the information collected on the Selmun promontory, four paths were identified to be surveyed with the georadar. The first profile follows the path detected with the ERT array in order to compare the results obtained. The other three profiles follow a trend perpendicular to the first, with the aim of intercepting possible fractures within the plateau. During the survey, various parameters were selected based on the objectives to be identified. For example, data were acquired with a sampling interval of 3.125 ns and 512 samples per trace over a time window of 600 ns, which

corresponds to an approximate depth of 30 m in limestone with electromagnetic wave propagation velocities of 0.1m / ns. (Davis & Annan, 1989). In addition, due to the altitude differences in the surveyed area, it was necessary to perform topographic corrections to the acquired B-scans. The georadar acquisition was performed in manual mode, as the antenna was transported manually by means of special support, along the four selected paths and with a height above the ground level of about 5cm. The acquisition was performed with the antenna oriented parallel to the direction of travel, at an average walking speed of about 1 m / s.

Figure 36: Photo acquired during the georadar survey. The photo shows the tripod and rod of the Differential GNSS, the Phantom 4 Pro UAV used for photogrammetric survey and the Cobra Subecho-70 georadar.

4.5.2 GPR data processing

The second phase of the work is data processing. A Georadar profile (B-scan) can be compared to an outcrop, containing characteristics relating to the genesis and natural and / or anthropic alteration of the rocks. Data were processed using the commercial software Prism2 Ⓡ (RadarTeam, v2.7) and the data processing sequence is illustrated below (fig. 37). Ground penetrating radar data processing must include zero time

correction. The zero point is a point where the time counting of the reflected signal starts (Yelf, 2004). According to Soldovieri et al. (2008) and Steinbeck et al. (2022) the zero time has to be placed at the early wavelet. In this case, the time depth was corrected with a value of -18ns. In order to eliminate background interference, or the direct signal from the transmitter antenna, as well as to lessen the severity of ringing and horizontal banding artefacts over the whole transmission, a background removal function was applied (Pipan et al., 2000). During propagation in the subsurface, electromagnetic waves are characterized by a faster amplitude decay of the signal with depth (Bianchini et al., 2019). The gain function is a digital amplification of the traces that allows increasing the signal while the depth is increasing too, highlighting any deep anomalies.

The Ormsby filter is a band-pass filter that includes the high-pass and low-pass filters and is a crucial filtering step in the processing of GPR data. Ground waves and other environmental noise sources can be eliminated using highpass, which applies a cut-off to low-frequency components across the entire frequency spectrum of a single trace. On the other hand, the high-frequency elements of each trace's frequency spectrum that are typically caused by additional electromagnetic interferences are blocked off by the low-pass filter (Pipan et al., 2000; Bianchini et al., 2019). The data depth was then calculated using the hyperbola fitting method (Persico 2014), obtaining a propagation velocity for electromagnetic waves of about 0.106 m / ns and a corresponding permittivity value of 8 which is plausible considering the mean value of the limestone dielectric constant (Martinez & Byrnes, 2001). The dielectric constant k and the propagation of electromagnetic waves in the subsurface are connected by the equation $v = \frac{c}{\sqrt{k}}$, where c is the velocity of the electromagnetic wave in free space, which is around 0.3 m/ns. After that, topographic data acquired with a differential GNSS were applied to the B-Scans to correct the altitude in the profiles and to recreate a GPR profile as closely as possible to the local terrain.

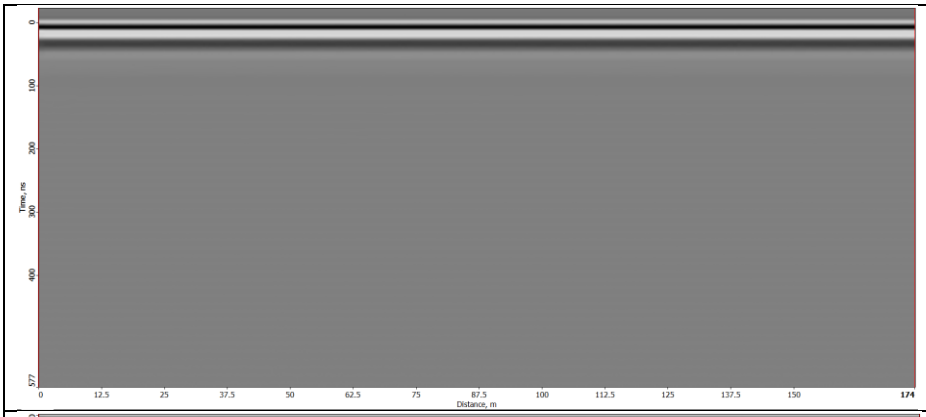	**Raw file**
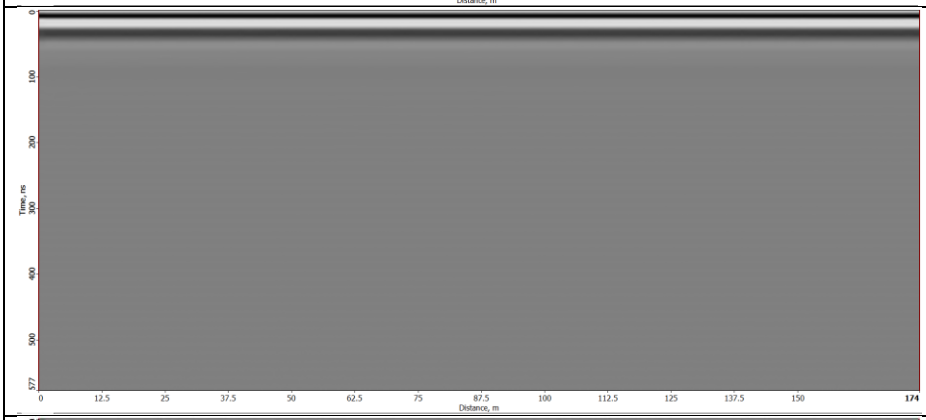	**Zero time correction** -18ns
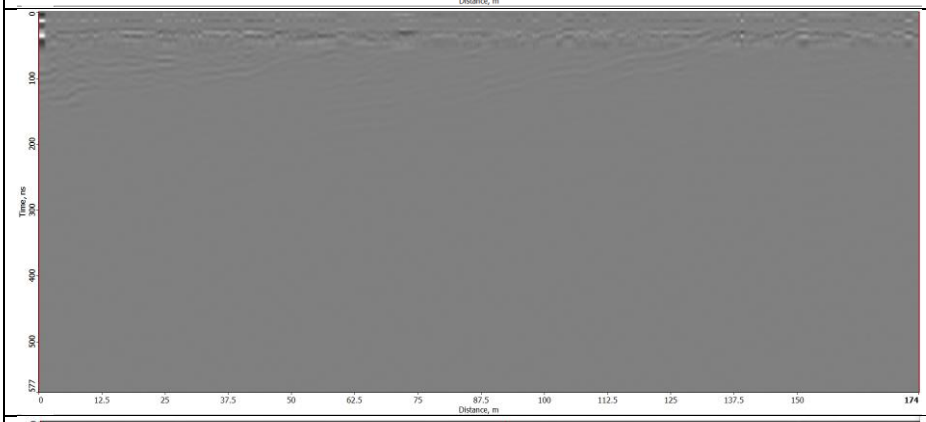	**Background removal**
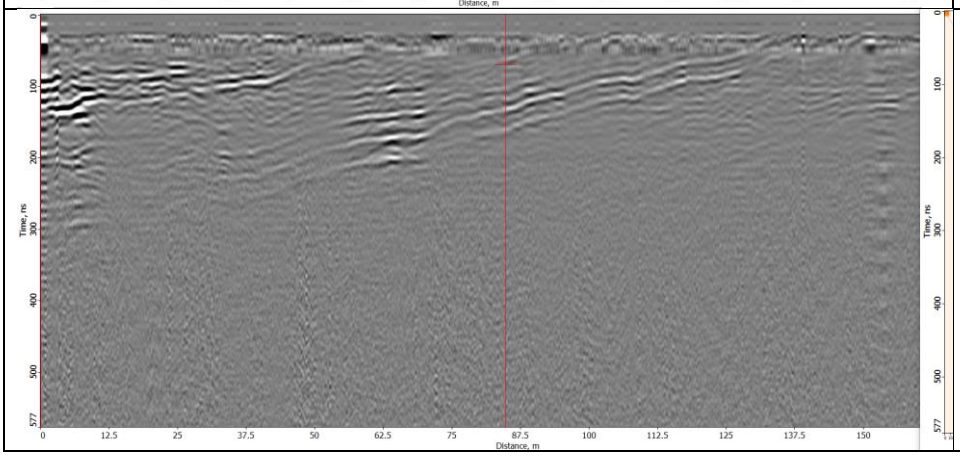	**Gain function**

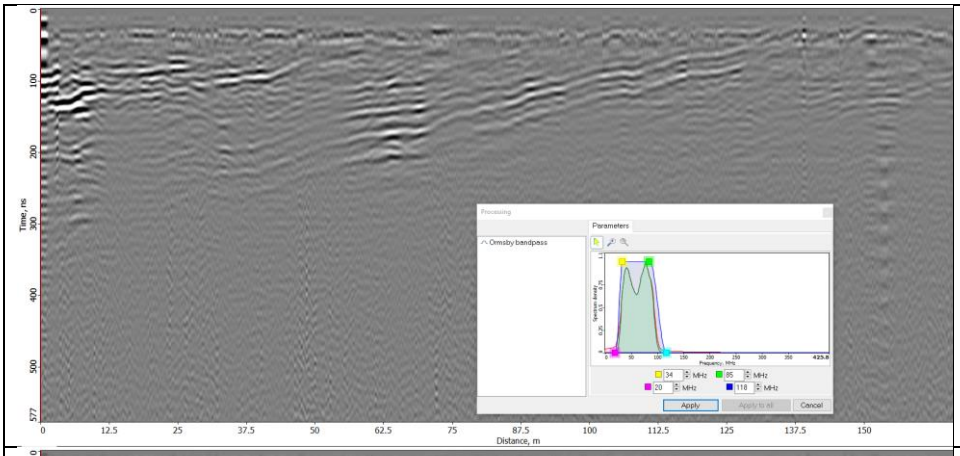	**Orsmby bandpass** Band-pass filters in the range of frequencies between 20 and 118 MHz
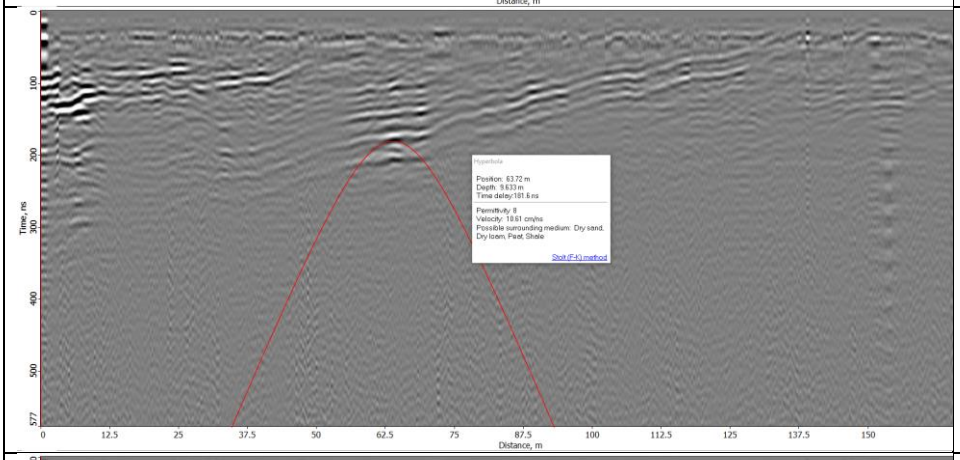	**Velocity Estimation** Permittivity 8, velocity 10.61 cm/ns
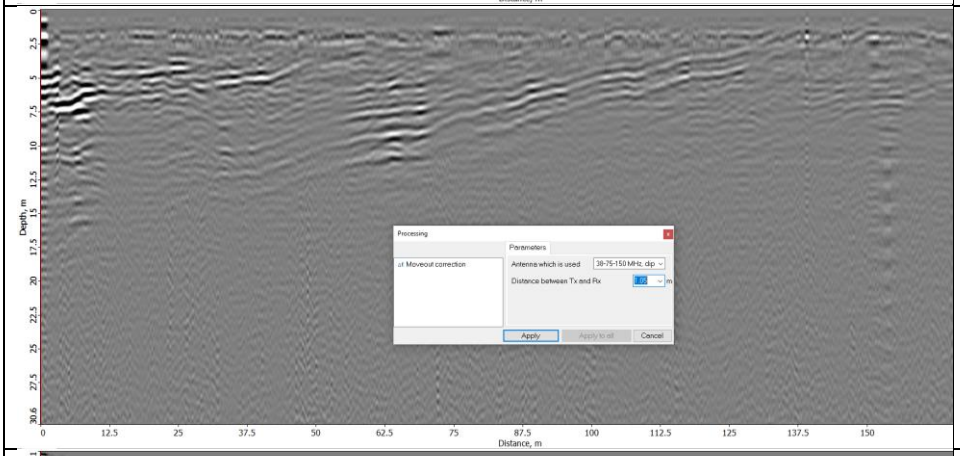	**Moveout correction and time - depth convertion** Distance between Tx and Rx antennas 1.05m
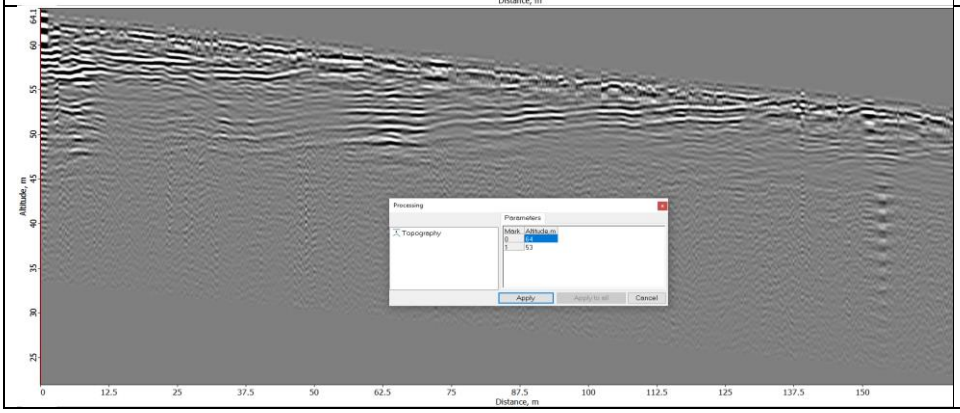	**Topographic correction**

Figure 37: *Schematic view of GPR data processing.*

4.5.3 GPR results

The GPR surveyed area on top of the Selmun's plateau is characterized by a topographic difference in altitude of about 20 metres from North-West to South-East (as visible in the DEM of figure 38) which has been corrected with GNSS data. All profiles were interpreted in order to identify potential anomalies associated with the presence of vertical discontinuities. The results of the four GPR profiles show different anomalies due to the cracks in the UCL as shown in figure 38. The four georadar profiles were overlayed on the DEM in the GIS project, in which the vertical fractures hypothesized by the interpretation of the georadar anomalies were traced. It is noted that along the edges of the cliff of the Selmun promontory, there is a correspondence between some GPR anomalies and the visible fractures on the surface mapped by Colica et al. (2021). The maximum depth reached by the electromagnetic waves is about 20 metres and corresponds to the stratigraphic contact between upper coralline limestone and blue clay. This result confirms the findings of the electrical tomography investigation and, thanks to the higher resolution of the data, offers a starting point for the hypothesis of the propagation of vertical fractures from bottom to top in gravity-induced lateral spreading processes as demonstrated by Bozzano (2008, 2010, 2013) and Alfaro (2019).

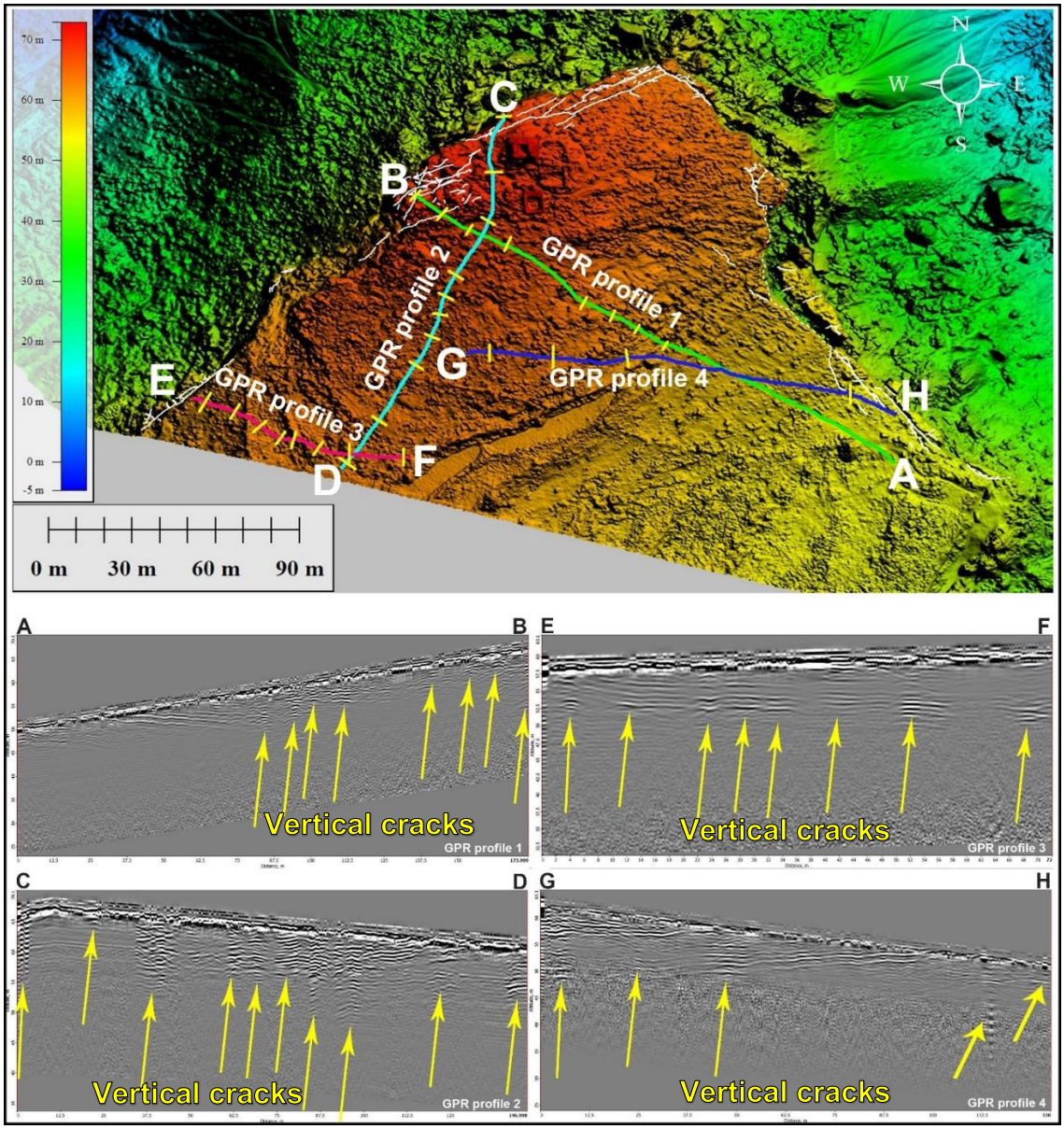

Figure 38: *On the top part of this figure is visible the GIS project with the DEM overlayed by the georeferenced paths of the four GPR profiles. The white polylines superimposed on the DEM are the visible fractures from the surface, while the yellow lines represent the georadar anomalies interpreted as vertical fractures. The second half of this figure shows the processed B-scans of the four GPR profiles and the yellow arrows indicate the vertical fractures.*

Finally, the georadar profile C-D and the electrical resistivity tomography profile U-V with topographic correction were compared as acquired along the same line. In light of the results obtained from this comparison (Fig. 39), it is clear that the GPR offers greater resolution for identifying fractures in rocks. Furthermore, the GPR data does not require an inversion process and interpretation of a model, whereby the results have greater reliability and less noise. The time and ease of data acquisition are other advantages of

the georadar method compared to the ERT, in fact, the four GPR profiles with GNSS positioning data were acquired in about 20 minutes by a single operator with raw data in real-time, while one ERT profile with 32 electrodes required about three hours for the electrode installation / removal and data acquisition in the different configurations and the involvement of a team of three operators. On the other hand, the ERT offers greater penetration into the different geological strata. In fact, with the ERT method, it is possible to penetrate beyond the UCL-BC interface, and this is limited by the length of the array, while the electromagnetic waves of the GPR penetrate up to the UCL-BC interface and are unable to penetrate the Blue Clay for physical limits related to their water content. Overall, both techniques are complementary and it is preferable to use them together to better constrain the results. Furthermore, for the interpretation of the outputs of these techniques, it is essential to know the local geology.

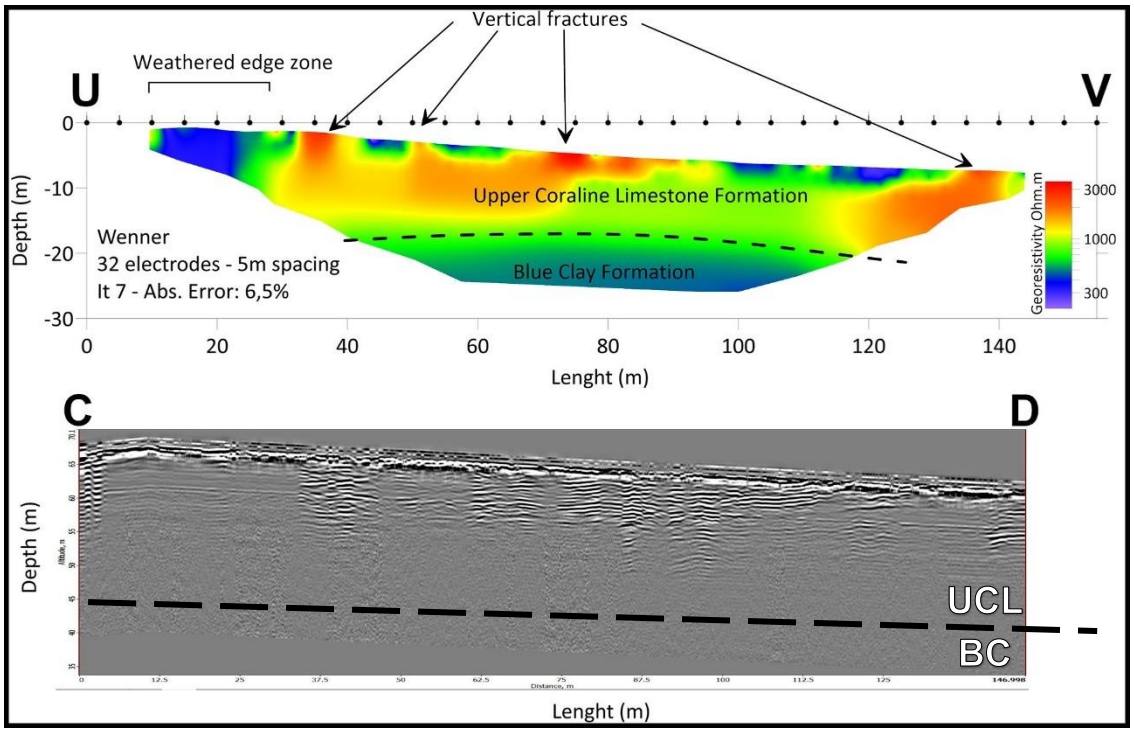

Figure 39: *Comparison between ERT and GPR results acquired along the same line on the Selmun plateau (Malta). The black dashed line indicates the stratigraphic contact between upper coralline and blue clay.*

Finally, by integrating the results of the geophysical surveys and the geological data into the 3D model from UAV-photogrammetry, the 3D geological model of the Selmun promontory was reconstructed. (Fig. 40).

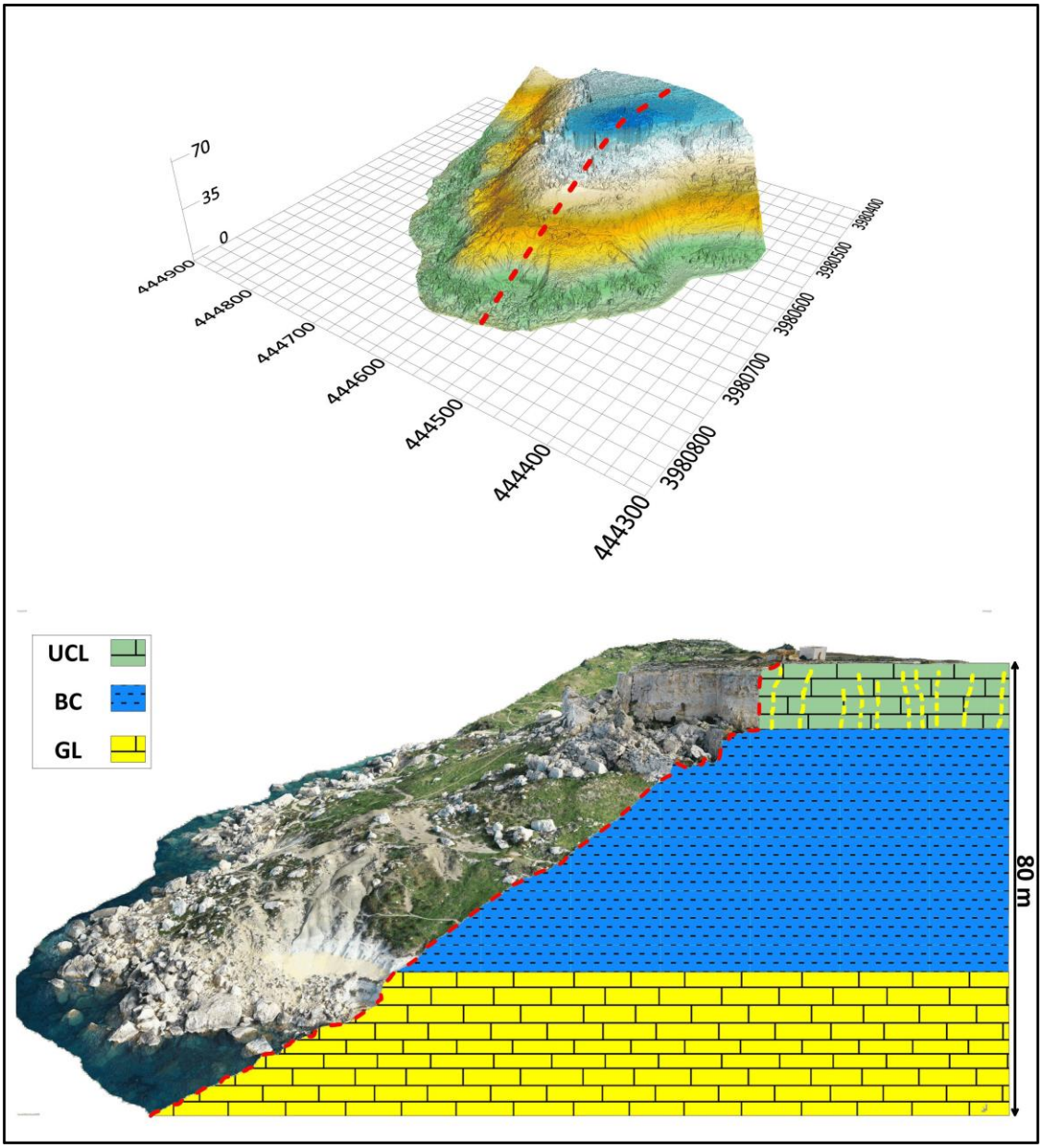

Figure 40: *At the top, there is a three-dimensional view of the DEM of the Selmun promontory (Malta) with the red dotted line indicating the line followed to section the 3D model. Below, in the sectioned profile of the three-dimensional model, the geology reconstructed from the geophysical surveys of ERT and GPR has been inserted. The yellow dashed lines on the UCL layer are a sketch (not to scale) of the anomalies detected with the two geophysical techniques.*

4.6 Time-lapse imagery analysis in GIS for the identification of blocks movement

The geophysical investigation highlights the current state of erosion of the Selmun cliff: gravitational processes of various types (lateral spread, topple and fall) affect the different portions of the slope depending on the nature of the rocks involved and the variable geometry of the slope. The set of these processes determines the progressive retreat of the cliff, in particular with detachments of isolated blocks or collapses of limited portions of rock starting from the top cliff edge constituted by the upper coralline limestone. The 3D digital model of Selmun promontory was used to map and measure important features such as fractures, joints, and large boulders. In addition to this, high-precision orthomosaic has been rendered and compared with aerial and satellite images captured between 1957 and 2021. All these data have been integrated into a common GIS database.

4.6.1 Multi-temporal image monitoring method

In this study, a temporal reconstruction of the detachments was made and the consequent reconstruction of the trajectories followed by the blocks of UCL detached from the Selmun cliff. The study area on which I focused is the east side of the Selmun promontory, as it is the most active side, from the point of view of the collapses, in the last sixty-four years. Historical aerial images were acquired starting from 1957 and subsequently integrated into a GIS together with satellite images starting from 2009 and UAV images from 2018 and 2021 (Tab. 4).

Table 4: *Summary table with image information used in this study.*

Date	Source	Specs
1957	Analogue aerial photo	Lens 6” 4,200 feet Scale 1:8000
1967	Analogue aerial photo	Lens 6” Scale 1:4000
1978	Analogue aerial photo	Lens 152.95mm Scale 1:10000
1988	Analogue aerial photo	Lens 153.23mm Scale 1:6000
1998	Analogue aerial photo	Lens 303.98mm Scale 1:10000
2008	Analogue aerial photo	Lens 303.55m Scale 1:4000
2009	Satellite image	N/A

	Maps data: Google, Image © 2022 Maxar Technologies	
2013	Satellite image Maps data: Google, Image © 2022 CNES / Airbus	N/A
2017	Satellite image Maps data: Google, Image © 2022 Maxar Technologies	N/A
2018	UAV Orthomosaic	Camera sensor: 1'' CMOS Effective pixels: 20M. Lens: FOV 84° 8.8 mm/24 mm (35 mm format equivalent) f/2.8 - f/11 auto focus at 1 m - ∞
2021	UAV Orthomosaic	Camera sensor: 1'' CMOS Effective pixels: 20M. Lens: FOV 84° 8.8 mm/24 mm (35 mm format equivalent) f/2.8 - f/11 auto focus at 1 m - ∞

The UAV orthomosaic reconstructed by photogrammetric processing (Colica et al., 2021) was used as a reference image for the geographical correction of aerial and satellite images. The image alignment tool, called “rectify imagery” in Global Mapper® GIS software (Global mapper, 2022), was used for the assignment of the geographical position and the scale of the non-georeferenced images. Georeferencing takes place through the use of Ground Control Points (GCPs) that can be entered manually (Fig. 41A) and it is common when working with paper maps that have been scanned and other non-geotagged images. After a file has been successfully georeferenced, it is displayed in the correct location within the Global Mapper. The initial adjustment can always be changed. Once the images were georeferenced, it was possible to qualitatively verify the level of overlap with the reference orthomosaic of 2021 using the "image swipe" tool in Global mapper. This tool allows you to easily view the superimposed layers interactively, allowing you to select a raster / image layer to move by holding down the left mouse button and dragging in a certain direction allowing you to easily locate and date the morphological variations of the area of interest occurred over time (Fig. 41B). Finally, polygons of a different colour for each year, corresponding to the edge of the

promontory cliff and to the detached blocks along the slope were traced within the GIS for each georeferenced image.

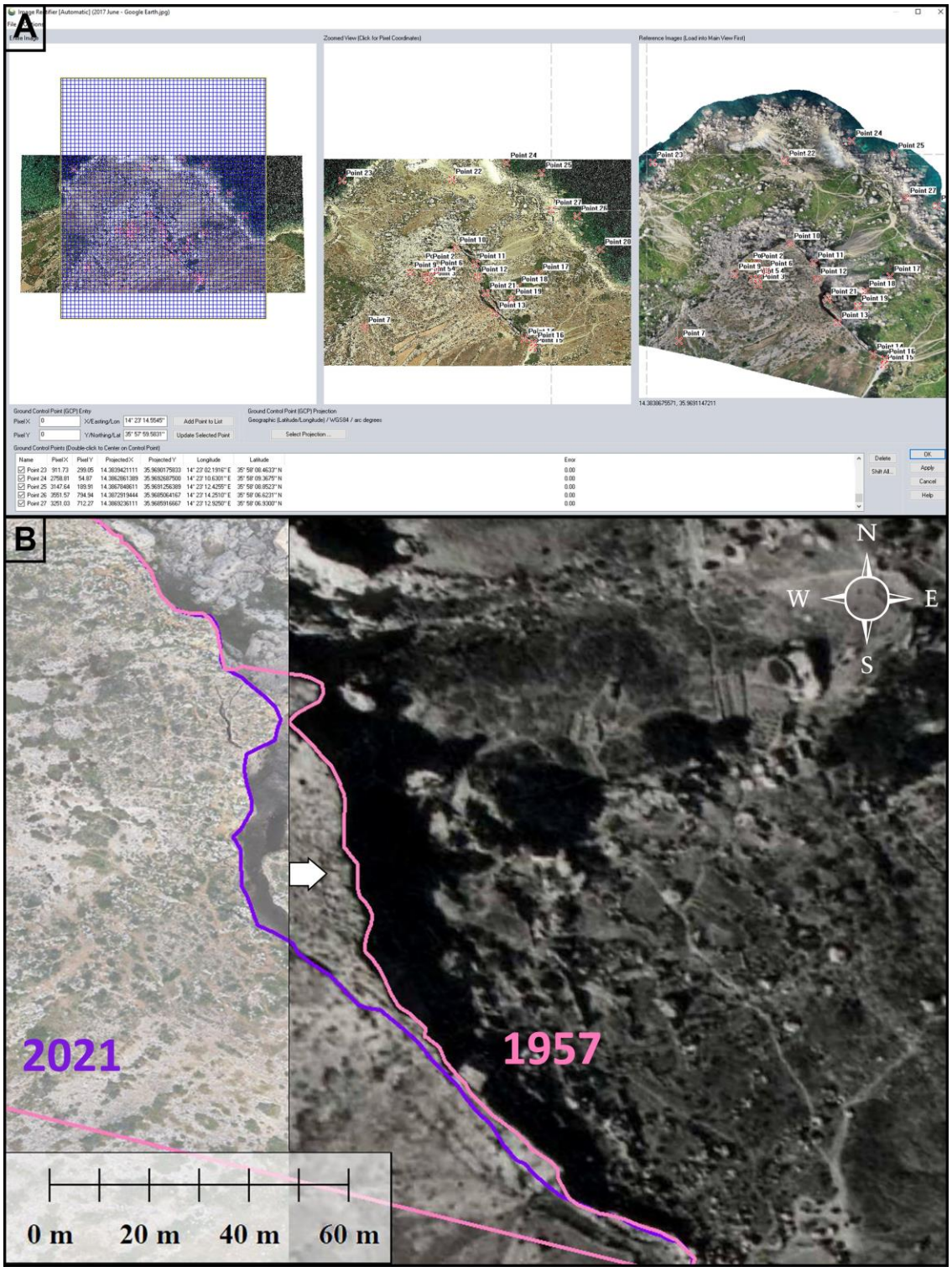

Figure 41: *(**A**) Screenshot of the georeferencing menu in the Global mapper software during the insertion of markers. (**B**) Comparison between the 1957 aerial orthophoto and the 2021 UAV-based orthomosaic using the GIS "image swipe" tool. The two pink and purple polygons respectively indicate the cliff's profile in the Selmun promontory's northeast area (Malta) in 1957 and 2021.*

4.6.2 Multi-temporal data analysis results

The results of the qualitative multi-temporal analysis in GIS are reported below and are divided between figure 42A, which highlights the blocks that detached in the time interval 1957-2021, and figure 42B, which maps the diffusion along the slope of the blocks collapsed. In addition, the area of the polygons representing the active blocks in the last sixty-four years was also measured.

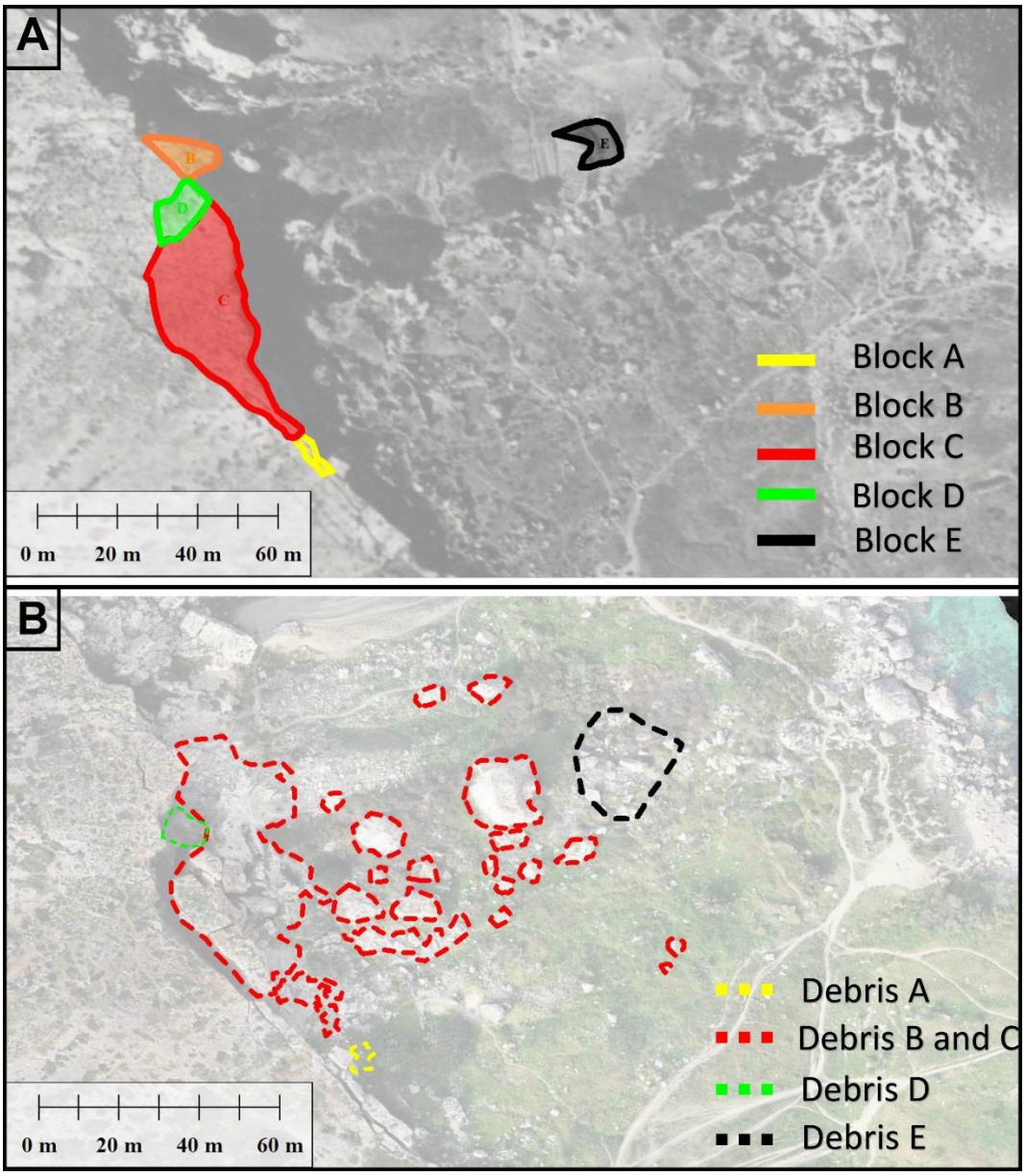

Figure 42: *Results obtained with the multitemporal analysis. (**A**) Aerial photo from 1957 in which the blocks that will move in the next sixty-four years have been mapped. (**B**) Orthomosaic obtained from UAVs (Colica et al., 2021) in which the areas covered by the debris of the blocks that detached between 1957 and 2021 are mapped. Block "E" lay on the slope in 1957 and that was shattered by the probable impact of rolling boulders from blocks "B" and "C" between 1988 and 1998.*

The collapse of block “A” (20,726 sq m) has been identified between 1957 and 1967 while between 1978 and 1988 the propagation of a fracture separating blocks “B” and “C” from the cliff is noted. In 1988 the resolution of the image is lower than the others used in this study, but, in spite of everything, it provides us with information on the widening of the fracture that separates block "C" from the cliff. Between 1988 and 1998 blocks “B” (84,695 sq m) and “C” (708 sq m) completely detach themselves from the cliff and are distributed along the blue clay slope. Finally, between 1998 and 2008 the last block to collapse is block "D" (92,519 sq m). It is also noted that block "E", already present along the slope in the first image of 1957, maintains its position and morphology until 1988 after which it appears shattered. It is therefore assumed that block “E” was found in the trajectory of one or more boulders ("B" and / or "C"), that detached between 1988 and 1998, and that during their rolling have impacted against it, shattering it. A summary of the temporal reconstruction of these events is available in Table 5.

Table 5: *Summary of the multitemporal analysis. E* is the boulder on the slope that fell apart between 1988 and 1998.*

Time-lapse	Collapsed block	Area in square metres	Height in metres measured in the 3D model	Estimated volume in cubic metres (Area*Height)	Polygon colour
1957-1967	A	21	5	105	Yellow
1988-1998	B and C	85 and 708	10 and 13	850 and 9204	Orange and Red
1998-2008	D	93	12	1116	Green
1988-1998	E*	77	N/A	N/A	Black

It should also be noted that due to the limited number of aerial images available, the time intervals in which the collapses occurred can be confined to the minimum range of ten years. In the decades this limit has been overtaken thanks to the new technologies of aerial drones and the availability of high-resolution satellite images updated on a daily basis and global coverage.

4.7 Rockfall dynamic simulations

Rockfall events can have a direct or indirect impact on territories, infrastructures and humans, so it is necessary to assess the risk in order to be able to adopt adequate protection measures to mitigate the effects caused (Sarro et al., 2014, 2018). In the Selmun cliff gravitational processes of various types such as lateral spreading, toppling and rockfall affect the different portions of the slope depending on the nature of the rocks involved and the variable geometry of the slope. The set of these processes determines the progressive retreat of the cliff, in particular with detachments of isolated blocks or collapses of limited portions of rock starting from the top cliff edge constituted by the upper coralline limestone. Landslides of this type are amply documented on the east side of the Selmun promontory by small recent detachment niches with yellowish-brown surfaces, clearly distinguishable from the rock mass with grey surfaces. Similarly, detachments of isolated blocks are evidenced by the limestone rock volumes present on the coast line, some of which are even below the mean sea level.

Within this thesis, the promontory of Selmun (Malta) was examined and some real events of rockfall identified and measured by multi-temporal GIS analysis were reconstructed. The Selmun rockfalls were simulated using a probabilistic analysis in RocPro3D software (Barnichon, 2022) which uses GIS technology to reproduce 3D rockfall trajectories followed by the detached blocks and estimate their speed, rebound heights, energy impacts and stopping points. The rockfall events chosen for these simulations are located in the north east of the Selmun promontory where rock detachments occurred in the last 64 years and have been identified through aerial and satellite photos (Table 4). Therefore, these rockfall events were reconstructed using a probabilistic approach and were calibrated using real observed and measured data. The measurements extracted from historical orthophotos were integrated into the GIS with the volumetric data of the blocks extracted from the 3D model derived from UAV-based photogrammetry (Colica et al., 2021). After that, the hazard posed by these rockfall events was assessed based on the simulation results.

4.7.1 Blocks volume estimation

Agisoft Metashape photogrammetry software was used in this study to calculate the volume of the blocks on the clay slope and those partially detached from the cliff. Starting from the 3D model, the UCL blocks present in the north east area of the Selmun promontory were chosen and mapped by using markers (fig.43A) to which an identification number, the calculated volume and the geographical coordinates were associated (table 6). To calculate the volume, each block was isolated from the model using the selection and clipping tool and then, using the "close holes" function of the mesh, it was possible to create a solid model and calculate the volume. It is important to note that the volume extracted from the blocks takes into account only the outcropping surface with respect to the surrounding ground (fig. 43B) so it could be slightly underestimated due to the sinking of the block in the clay.

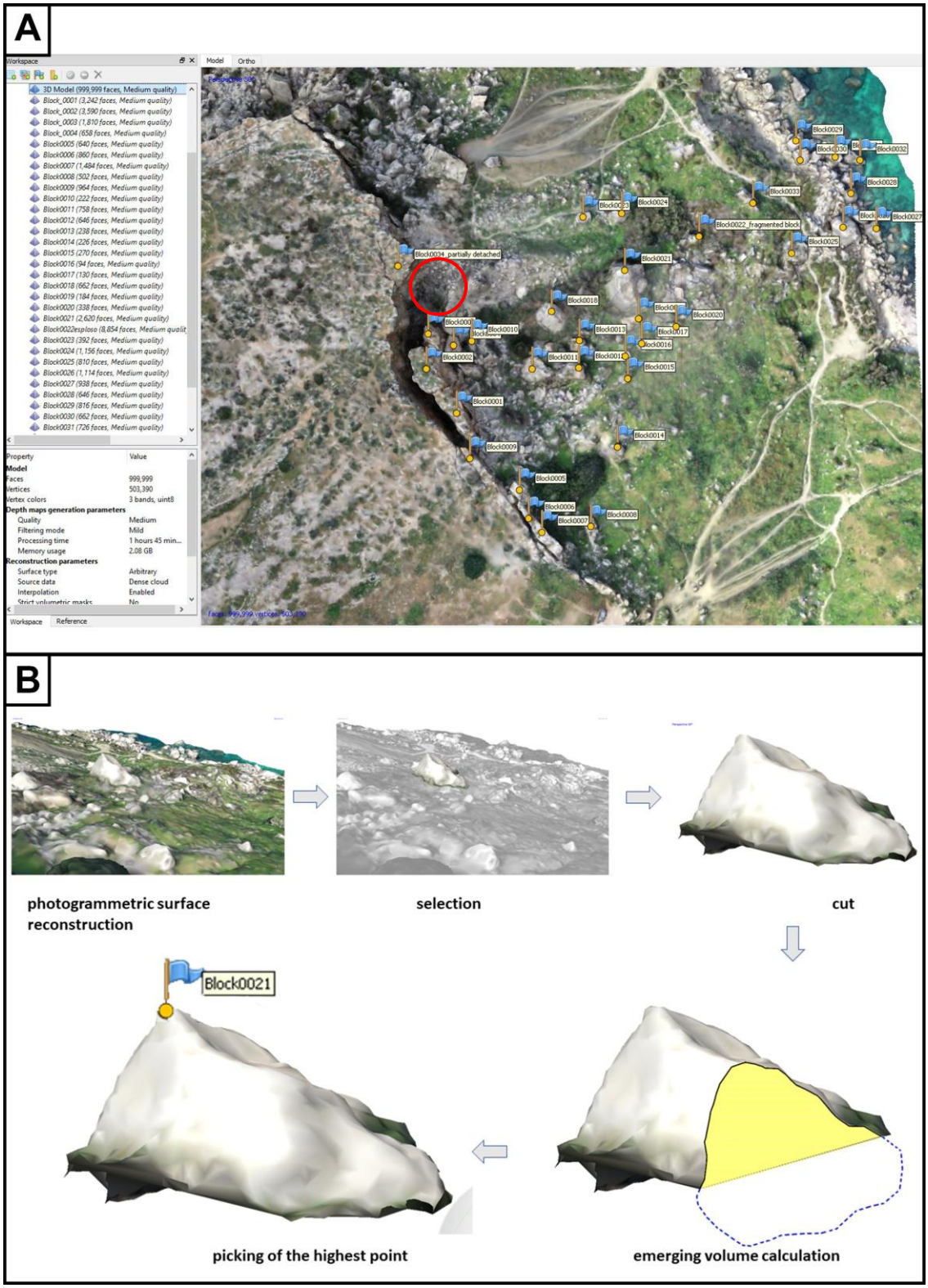

Figure 43: *(**A**) 3D model of the Selmun promontory with blue flags indicating the measured blocks. The red circle indicates a block partially detached from the cliff. (**B**) Workflow of the volume measurement process of a block.*

Table 6: *Summary of identification number, volumes, geographical coordinates and elevation in metres (AMSL) of mapped blocks. *Block partially detached from the cliff.*

Block ID	vol. m^3	X	Y	Z
0001	553	444648.107	3980487.732	55.127
0004	93	444645.643	3980508.837	47.752
0003	268	444639.713	3980512.445	56.579
0002	1022	444638.848	3980501.505	55.695
0005	71	444667.470	3980463.260	52.688
0006	36	444670.276	3980454.301	52.437
0007	92	444674.468	3980449.740	51.962
0008	29	444689.275	3980450.237	44.083
0009	109	444652.437	3980473.441	55.236
0010	9	444650.503	3980510.345	43.363
0011	58	444669.373	3980501.144	37.634
0012	107	444684.529	3980501.491	35.678
0013	17	444684.381	3980510.439	32.208
0014	16	444697.525	3980475.303	36.708
0015	13	444700.628	3980497.660	31.187
0016	4	444699.636	3980505.207	29.411
0017	9	444705.041	3980509.538	27.383
0018	96	444675.403	3980520.101	34.888
0019	1	444703.992	3980517.927	25.526
0020	41	444716.927	3980515.302	24.326
0021	865	444699.606	3980534.119	31.412
0022	107	444724.926	3980547.106	16.897
0023	26	444685.027	3980552.564	26.591
0024	52	444698.033	3980554.274	22.379
0025	81	444757.725	3980541.438	12.661
0026	201	444776.725	3980551.277	7.885
0027	125	444788.962	3980551.144	5.578
0028	59	444779.621	3980563.509	6.396
0029	77	444760.159	3980582.771	4.812
0030	67	444761.506	3980575.478	6.414
0031	56	444774.351	3980577.121	4.524
0032	37	444783.976	3980576.497	0.855
0033	46	444744.000	3980559.211	13.625
0034_*	1224	444631.4719	3980533.3188	60.976

Most of the blocks that emerge from the surface of the clayey slope are concentrated in the range of 1-200 m^3, while about 15% of the blocks measured have a volume between 200 and 1224 m^3. By plotting on the DEM the elevation relative to the mapped blocks (Fig. 44A), it is possible to note that the blocks with a smaller volume are evenly distributed along the slope, while those with a volume greater than 200 m^3 are located at an elevation above mean sea level (AMSL) in the range 30 - 60 m (Fig. 44B). The block with identification number 0034 is partially detached from the plateau and has a pseudo-sphere shape with a diameter of about 12 m (Fig. 43A). For the latter it was impossible to measure the volume using the mesh selection method because it is currently a body integral with the UCL plateau and with most of the sides hidden. Therefore, for this block, the volume was estimated by measuring the area of the planimetric surface (102 m2) and multiplying it by the height of 12 m visible from the 3D model.

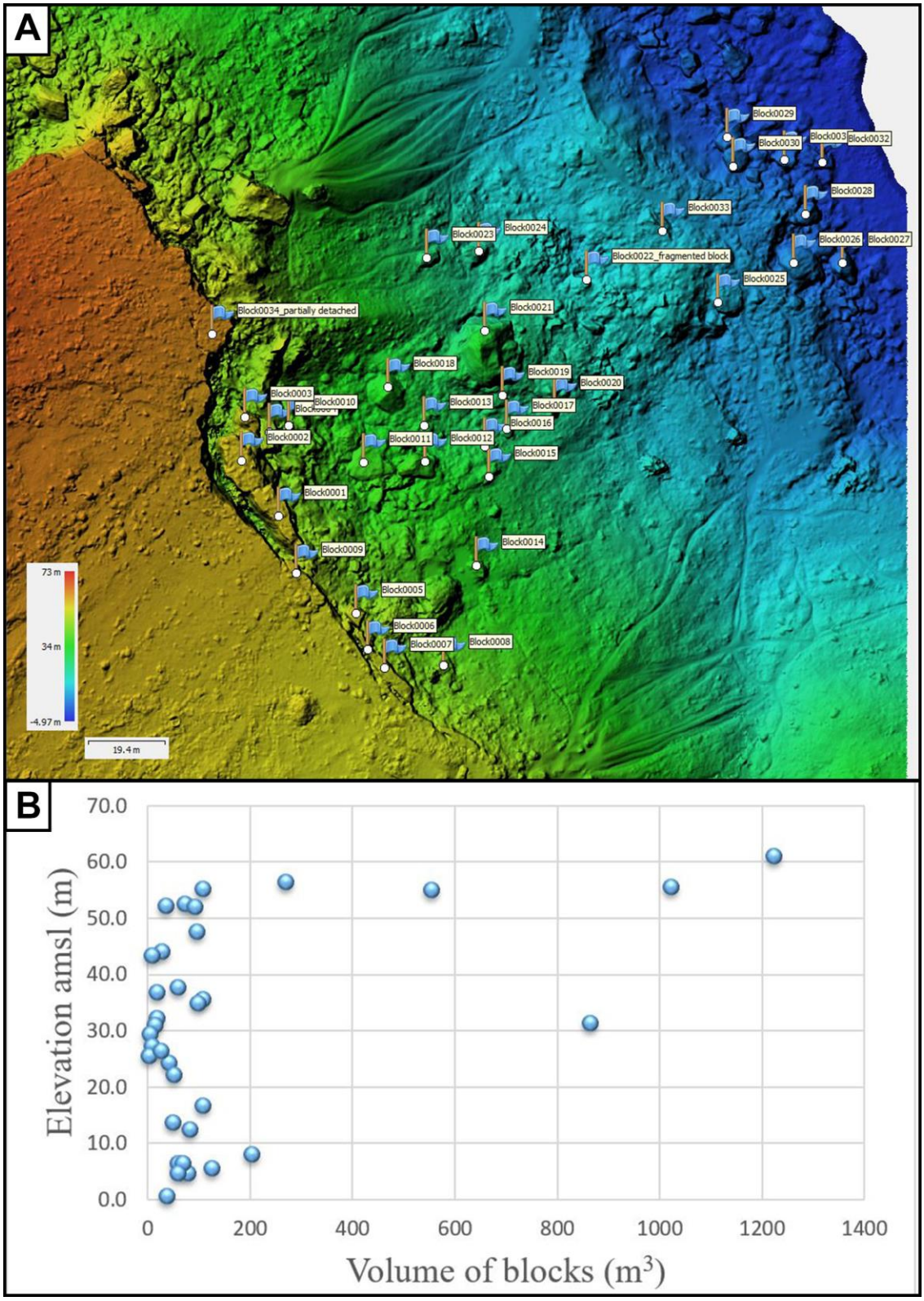

Figure 44: (A) *elevation model of the Selmun promontory with blue flags indicating the measured blocks. (B) Scatter plot of blocks elevation versus volume.*

4.7.2 Kinematic simulation and results

Once having reconstructed the movement of the blocks over time and having estimated their volumes, it was possible to move on to the simulation phase to reconstruct selected past events (Tab. 5) in order to calibrate the model and estimate the trajectories of future events.

For the input data of the kinematic simulation of the blocks were used the high-resolution DEM obtained UAV-photogrammetry, the orthomosaic and the 1: 2,500 scale geomorphological map of the Selmun promontory reconstructed by Colica et al., 2021. A high-quality DEM is essential for creating 3D simulations of trajectories even if it often includes vegetation and other elements in relief from the ground that can influence the trajectories of the simulated blocks as they are recognized by the software as irremovable and not fragmentable structures. For this reason, the original digital surface model (DSM) was modified to obtain a Digital Terrain Model (DTM) of the area of interest. In this regard, the vegetation and the rock blocks deposited along the slope of BC were manually removed from the 3D mesh which was finally smoothed. This operation was performed by means of the Agisoft Metashape software using the manual mesh selection tool and cutting the selected parts of disturbance to the simulation. The automatic mesh smoothing procedure present in the photogrammetry software was also used (Fig. 45).

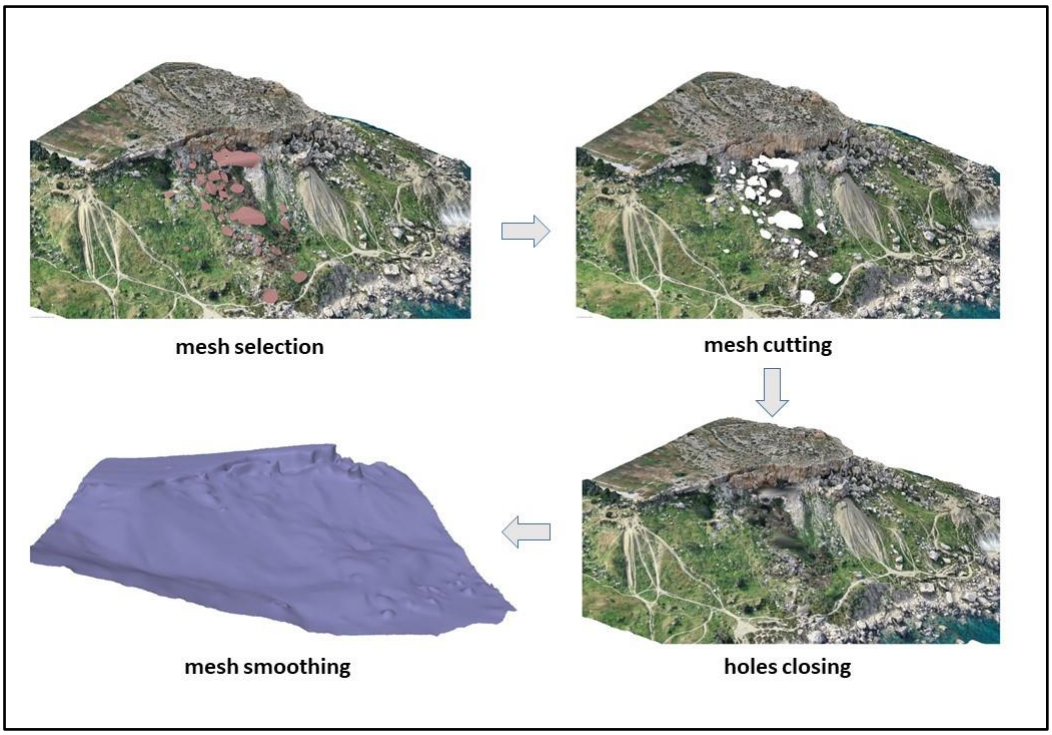

Figure 45: *Mesh cutting and smoothing process to transform DSM into DTM.*

Rockfall modelling was performed using RocPro3D software (RocPro3D, 2022) which includes a probabilistic component and allows for the definition of the characteristics of the soil as well as block parameters like starting position and mass in terms of probabilistic variables. Soil properties can be modelled using probabilistic uniform and Gaussian variables like dynamic friction coefficients, normal and tangential restitution coefficients, lateral deviation, and flattening of the rebound angle. The location of the probable source areas, a high-resolution DTM in raster format (the profile of the cliff was reconstructed using the historical data), the geometrical parameters of the unstable blocks, and the lithological properties are all needed as input data for the model. As mentioned above, the input DTM was obtained by treating the vegetation and debris blocks by directly cutting and smoothing the corresponding meshes. The potential areas of origin of the detachments of rock were identified by observing the presence of jointed rocks in precarious equilibrium along the slope through field surveys, aerial photographic interpretations and analysis of the three-dimensional photogrammetric model as well as the analysis of historical photos.

Regarding the geometric characteristics of the blocks whose collapse was simulated, they were considered to have a spherical shape by adopting a lumped-mass approach, thus assuming that the mass and shape of the blocks do not affect the dynamics of rockfall events (Li & Lan, 2015). Finally, the three different lithological units were selected from the DTM (Fig. 46) to which the values of the different restitution coefficients were assigned to quantify the energy loss caused by the impacts of the blocks on the slope (Sabatakakis et al., 2015; Gallo et al., 2021).

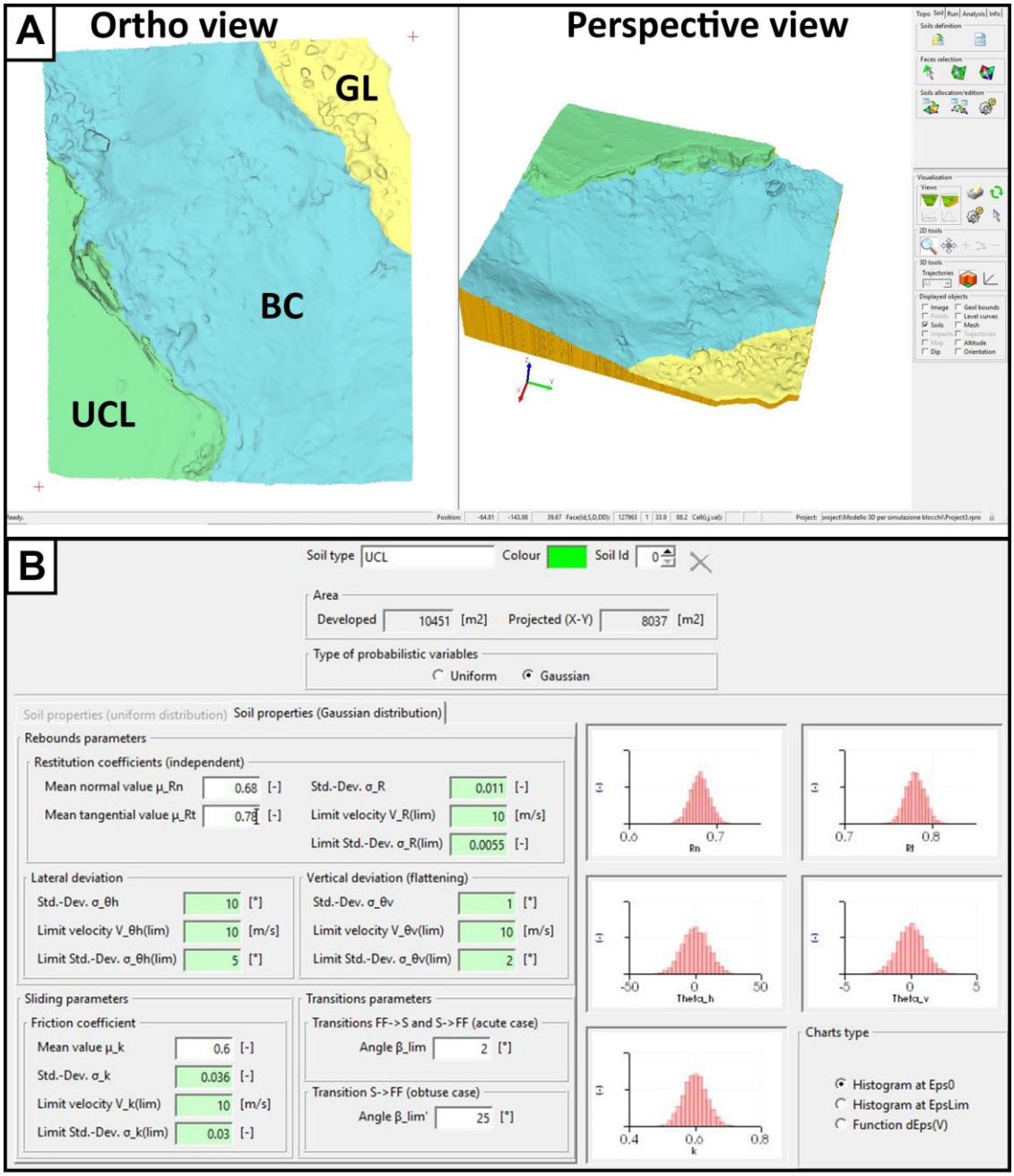

Figure 46: *(**A**) DTM in Rocpro3D with the types of soil defined by lithology. (**B**) The soil properties used during the simulation for the UCL.*

By using probabilistic functions, uncertainty and unpredictability in the choice of restitution parameters were introduced. The literature and research done in sites with comparable geological, structural, and geomorphological properties have been taken into consideration when defining these parameters (Hutchinson, 1988; Pfeiffer & Higgings, 1990; Budettaet al., 1994; Guzzetti et al., 2003; Mateos et al., 2016; Gallo et al., 2021). The properties of the three types of soil are expressed in terms of probabilistic variables as illustrated in table 7 (All parameters are explained in appendix II).

Table 7: *Soil parameters for Gaussian probabilistic variables used in the simulation.*

Parameters	UCL Mtarfa member	Blue clay	Globigerina Limestone
RESTITUTION COEFFICIENTS			
Mean normal value μ_Rn [-]	0,68	0,52	0.58
Mean tangential value μ_Rt [-]	0,78	0,61	0.65
Standard.-Deviation σ_R [-]	0.011	0.016	0.0125
Limit velocity V_R(lim) [m/s]	10	10	10
Limit Std.-Deviation σ_R(lim) [-]	0.0055	0.012	0.0075
LATERAL DEVIATION			
Standard.-Deviation σ_ θh [°]	10	7.5	8.75
Limit velocity V_θ h(lim) [m/s]	10	10	10
Limit Std.-Deviation σ_ θ h(lim) [°]	5	3.75	4.375
REBOUNDS FLATTENING			
Standard.-Deviation σ_ θv [°]	1	1	1
Limit velocity V_θ v(lim) [m/s]	10	10	10
Limit Std.-Deviation σ_ θ v(lim) [°]	2	2	2
FRICTION COEFFICIENT			
Mean value μ_k [-]	0.6	0.6	0.6
Standard.-Deviation σ_k [-]	0.036	0.045	0.045
Limit velocity V_k(lim) [m/s]	10	10	10
Limit Std.-Deviation σ_k(lim) [-]	0.03	0.03	0.03
TRANSITION PARAMETERS			
Angle β _lim (acute case) [°]	2	4	3
Angle β _lim' (obtuse case) [°]	25	35	30

The different areas of detachment have been identified on the DTM following the historical profile of the cliff. The latter was reconstructed by combining the digital model described by Colica et al. (2021) and information obtained from historical photos. The measures of the blocks associated with these collapses were selected considering the mapping made from the 3D model (see table 6) and the UCL density of 2146 kg m^{-3} was retrieved from Iannucci et al., (2018). Subsequently, the detachments of the blocks occurred in the time intervals 1957-1967 (A), 1988-1998 (B and C) and 1998-2008 (D) were simulated. The simulated results were compared with historical data and a good correlation between simulation and real data was obtained. Figure 47 shows the results of the simulations and the coloured dots represent the stopping points of the blocks after the collapse. It is noted that the distribution of these points is well correlated with the distribution of most of the boulders present in the area visible from the orthomosaic. A good correlation of the distribution is also obtained with the mapping of the historical events described in paragraph 4.6.2.

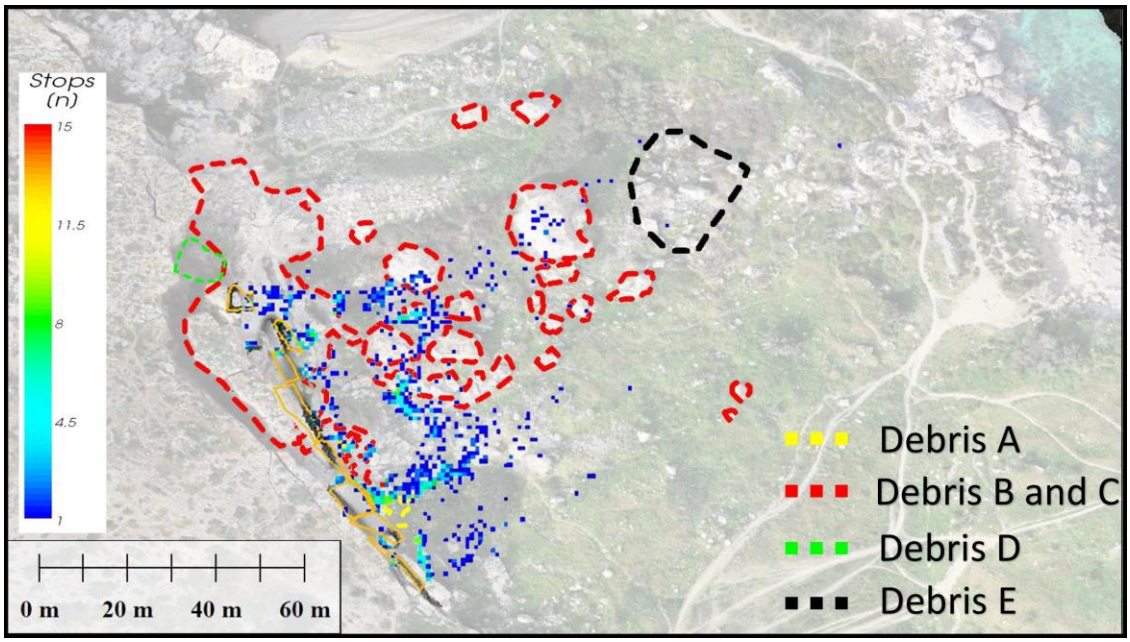

Figure 47: *Orthomosaic of the eastern area of the Selmun promontory with the following layers in GIS superimposed: (i) polygons in yellow indicate the selected detachment areas, (ii) dotted polygons delimit the areas where the collapsed blocks have been deposited in the last 64 years and refer to figure 42, (iii) the dots indicate the stop points of the boulders after the collapse obtained from the simulation in Rocpro3D. The Stops (n) in the legend on the left indicate the number of stopping points of the simulated trajectories.*

Furthermore, the energy, density, height, speed, stop points and impact points of each simulated trajectory were calculated with the rockfall simulation software (Figure 48). The preferential direction of the trajectory followed by the blocks is highlighted in the density map (Fig. 48A). The results obtained by simulating the detachment of blocks with a diameter from 8 metres to 18 metres showed a rebound height in the order of 5-8 metres with isolated peaks up to almost 20 metres (Fig. 48 B). The average speeds calculated are between 3 and 20 m / s with peaks of about 30 m / s (Fig. 48 C), while the kinetic energy developed at the moment of impact averages between 50,000 and 400,000 KJ and with energy peaks up to about 700,000 KJ (Fig. 48D).

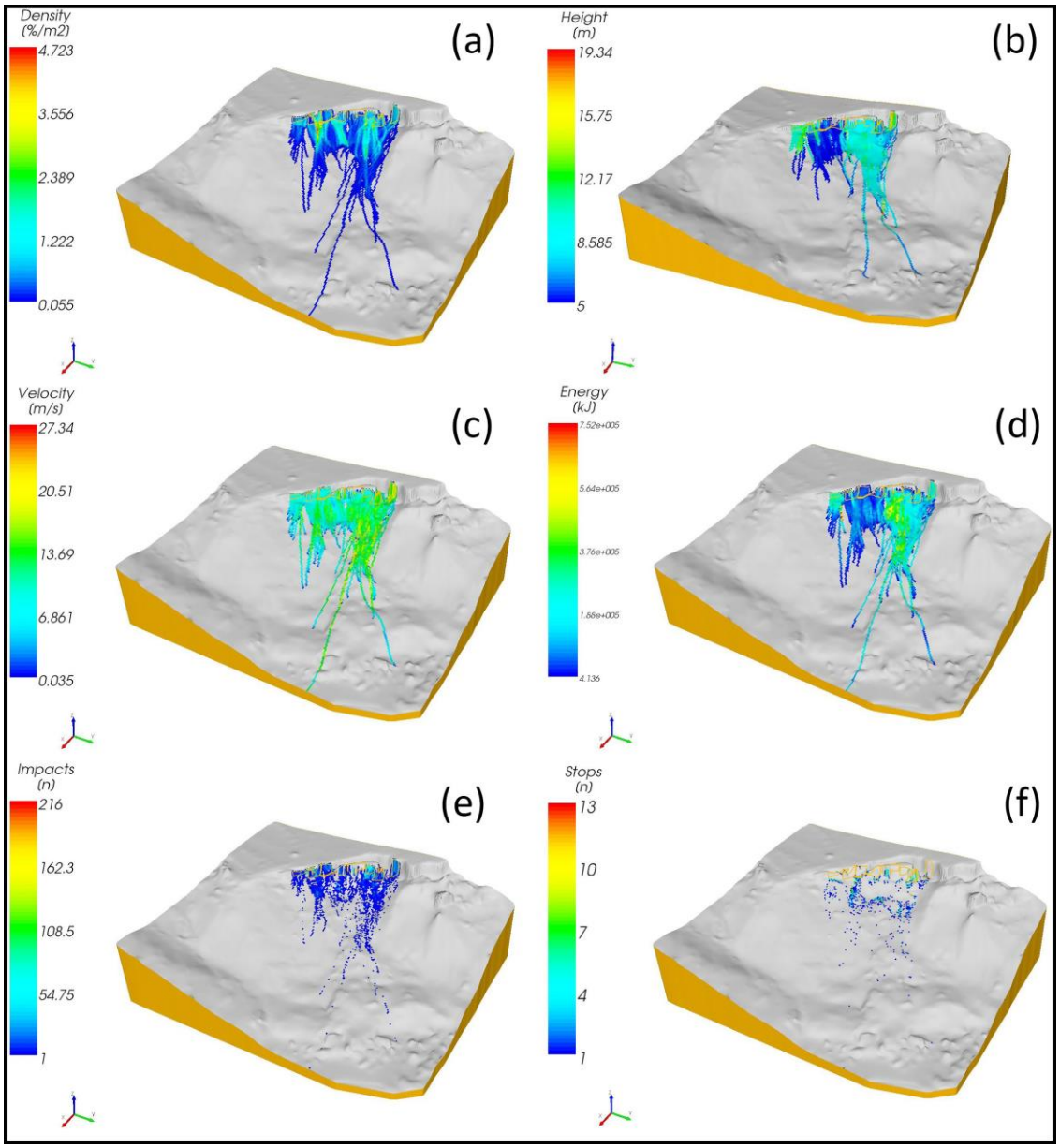

Figure 48: *3D simulation of historical rockfall events between 1957 and 2008: (a) density of simulated trajectories as a percentage per square metre (density map), (b) height map, (c) velocity map, (d) energy map, (e) impact points map, (f) stop points map.*

Finally, the same parameters have been used for the simulation of a partially-detached block (ID 0034, referred to table 6), with a diameter of 12 metres, measured by photogrammetric model. For this simulation, the previously smoothed DTM was used as the area affected by the mesh cleaning did not overlap the probable trajectories that this block could travel. It is also clear that the probable trajectories split into two paths due to the topography of the slope and the presence of large rock boulders on the slope at the base of the cliff. The results are summarized in figure 49. Average rebound heights have been estimated in the range between 6 and 9 m with peaks of 14 m, average speeds between 8 and 20 m / s with maximums up to 36 m / s and kinetic energies between 150,000 and 350,000 KJ up to a peak of 737000 KJ. Finally, it is noted that during the simulation some blocks reached the coast line and ended up in the sea.

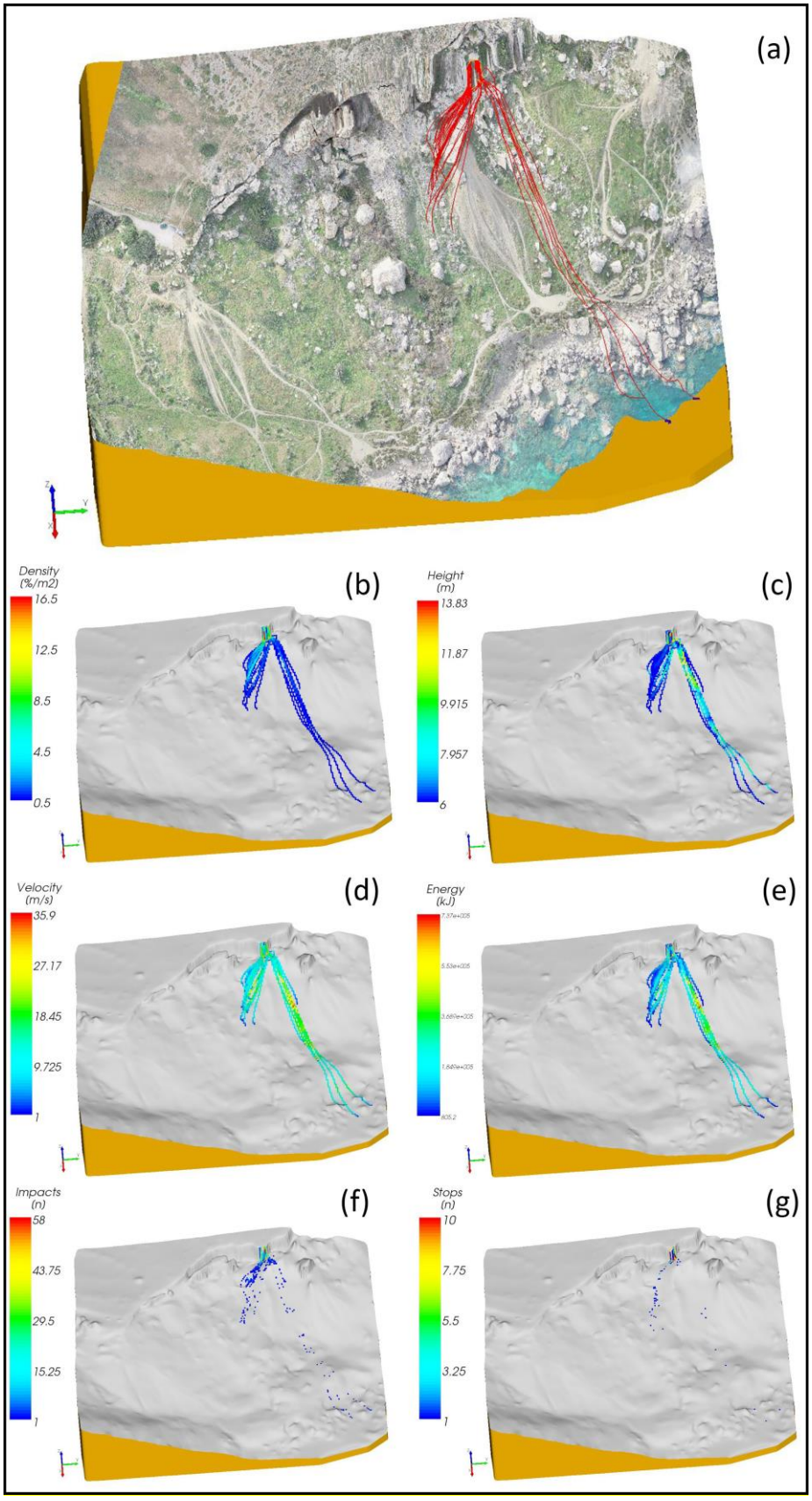

Figure 49: *3D rockfall simulation of semi-detached boulder ID 0034: (a) perspective view of the DTM with orthomosaic99 in which the estimated trajectories are indicated in red, (b) density map, (c) height map, (d) velocity map, (e) energy map, (f) impact points map, (g) stop points map.*

5. Discussion and Conclusion

This research aimed to develop an integrated method which combines geophysics and geomatics techniques with the main goal of studying and monitoring coastal hazards with particular regard to cliff failures. The area covered by this study is the Selmun promontory located in the north east of Malta. This site was chosen due to the high rate of erosive processes affecting the cliffs and also because the erosion process is similar to those occurring along the rest of the Maltese coasts. In addition, the lack of anthropization did not influence and compromise the observation of these erosive phenomena over a period of 64 years and furthermore contributed to have the data collection easier and not biased by human activities. A series of geospatial datasets captured by satellite, UAV equipped with remote sensors as well as in-situ measurements, have been integrated into a Geographic Information System (GIS). In particular, the photogrammetric drone survey performed during this research, combined with the high accuracy of the ground control points measured by differential GNSS, allowed the reconstruction of a three-dimensional model from which geostructural information was extracted for different areas of the promontory including the cliffs. These digitally extracted measurements were compared with the measurements acquired with the traditional manual survey in the field and the results were absolutely comparable. It should be emphasized that the digital survey method was found to be the most complete and safe as it made it possible to carry out a greater number of measurements along steep areas of the cliff that were not accessible to an operator without safety harnesses. The output extracted from the 3D model, such as the orthomosaic and the DEM, were fundamental for the planning of subsequent geophysical measurements. In the GIS environment, all the fractures visible from the orthomosaic were mapped and measured, while the thicknesses of the UCL and BC were measured from the 3D model. Furthermore, a geophysical survey was performed as part of this research in the Selmun study area, where two ERT profiles and four low-frequency ground penetrating radar profiles were acquired which allowed to measure the thicknesses of the UCL and the BC and then validate the measurements estimated from the analysis of the 3D model. From these geophysical investigations, possible fractures have been identified that propagate from the UCL-BC contact upwards and therefore not visible from the surface. In addition, other investigations were carried out

using the UAV-derived orthomosaic as a reference for georeferencing historical aerial photos and integrated into the GIS database together with satellite images for a total temporal coverage of 64 years. This multi-temporal analysis made it possible to reconstruct the historical profile of the cliff and identify and date the various collapses that have occurred, estimating the volumes of rock involved. Subsequently, the 3D model was used to measure directly from the mesh the volume of the blocks deposited along the slope of BC and to extract the volume of a block partially detached from the cliff facing north-east and about to fall. At this point, the RocPro3D software was used to simulate the collapses that occurred in the past and estimate the possible trajectories and energies that will affect future events. For these simulations, the high-resolution DTM derived from UAV-derived DEM and the physical and geomechanical parameters obtained from the literature were used. The three-dimensional model was very useful in identifying potential areas of detachment and together with the multi-temporal analysis of the images provided useful data about the trajectories followed by the blocks during past collapses. Through a posteriori analysis of the rockfall event, it was possible to calibrate the simulation parameters based on the real trajectories followed by the boulders. Energy levels and speeds were also assessed in this way. The validation was carried out by superimposing the stopping points obtained from the historical orthophotos and the simulation results. At a later stage, potential areas of origin were assessed by combining field surveys and digital model analysis. The three-dimensional model was very useful in identifying potential areas of detachment and together with the multi-temporal analysis of the images provided useful data about the trajectories followed by the blocks during past collapses.

The new methodology implemented in this thesis can be integrated with other methodologies already applied in the coastal areas in the north-west of the Maltese archipelago, such as for example the satellite SAR interferometry method and the monitoring of the movement of the blocks through the installation of GNSS sensors and fissurimeters (Mantovani et al., 2013, 2016). The great advantage of this new methodology, compared to satellite data, is offered by the high spatial resolution of the data acquired via UAVs, which makes it possible to observe and monitor landslide phenomena on a sub-centimetric scale with greater economic and logistical accessibility compared to other methods such as Terrestrial Laser Scanning (TLS) and terrestrial SAR.

Furthermore, the multidisciplinary nature of the method elaborated in this thesis required the development of an open GIS platform that is able to easily integrate other techniques and measurements that will be made in the future. This will improve the degree of accuracy of the results together with the growing technological evolution of the sensors that have been used in this study. One of the future implementations that could be done in this study area could be the installation of topographic nails in the areas of the promontory delimited by superficial and buried fractures, therefore prone to movement, also including other nails in the areas identified as stable. Using a total station installed in the points identified as stable, it will be possible to monitor movements of unstable areas in the order of millimetres and these same topographic nails can be used as ground control points for the construction of future 3D photogrammetry models, thus reducing intrinsic errors to GNSS measurements. At the moment a limitation related to this methodology is the need to acquire data on-site, but also in this case technological progress will fill this limitation. In fact, in recent years work has been done on fixed base stations that can host UAVs (Liu et al., 2018; Malyuta et al., 2020; Niu et al., 2021), and the sensors associated with them, equipped with photovoltaic panels for energy independence and ability to offer coverage and protection from foul weather and theft or vandalism. Furthermore, these bases act as ground stations and servers, so all the data referring to the flight controls of the UAV and to the sensors it transports can be transferred to another server that can potentially be found anywhere in the globe using the 5G network. This will make it possible to remotely monitor areas that are difficult to reach by an operator and furthermore, this automation in data acquisition will make it possible to reduce errors in measurements due to the human factor. Moreover, in the near future, this methodology will be applied in areas in the south of the Maltese archipelago, more urbanized and characterized by cliffs of Globigerina limestone, which due to its physical-chemical characteristics is exposed to frequent collapses along the cliffs.In conclusion, aerial photogrammetry ensures the safety of the operator in the field, especially in difficult or hostile geological environments that could pose a risk to human life, such as in the Selmun cliff areas. The 3D model and its output produced during this study are published as open-access data, on the public repositories of high-resolution topographic data OpenTopography (Crosby et al. 2013) and it is available at the following link:

https://portal.opentopography.org/dataspace/dataset?opentopoID=OTDS.112021.32633.1.

The results obtained from the geophysical methods are useful for indirectly mapping and monitoring the evolution of fractures over time and therefore allow for a broader view of the dynamics of the erosive processes affecting the high coasts. Monitoring of unstable cliff areas could provide an important contribution to hazard and risk assessment, and a vital tool for coastal zone management and civil protection. The great advantage of the approach presented in this thesis is given by the possibility of integrating into a GIS environment the output obtained from geomatics and geophysical investigations as well as simulation results in order to obtain results that can have enormous relevance for the design of rockfall mitigation measures hazard.

This, in principle, can represent a critical point for the Civil Protection authorities and decision makers also because routes for emergency responders or rescue teams could be completely blocked and in this type of site are not easily accessible. For example, this kind of study can also help in planning potential procedures of intervention taking into account that the site, in certain instances, could be reached only by sea vessels and/or using helicopters. Overall, the designed GIS platform (duly extended and implemented along the Maltese coasts) could allow authorities to better address social, economic and environmental issues which are of pressing importance in our modern and growing society.

6. Acknowledgement

The scientific investigations and studies carried out at the Selmun promontory were supported by the project “NEWS-Nearshore hazard monitoring and Early Warning System” (code C1-3.2-60) part-financed by the European Union under the Italia-Malta Cross-Border Cooperation Programmes, 2014–2020.

Appendix I: Problem statement of geological instability

Environmental risk can be defined as the likelihood that a specific event, that might be natural or caused by human intervention in the natural environment, takes place in a specific area at a specific time interval. The territorial vulnerability has to be considered when assessing the factors that could impact the territory and the environmental hazard considers all the factors that pose a risk to the environment (Villegas-González et al., 2017). The seismic and volcanic activities as well as hydrogeological instability might be the cause of geological hazards. Furthermore, the sources of the hydrogeological instability are commonly identified as floods, subsidence, erosions, avalanches and retreat of the coast. It is imperative to conduct an analysis and apply adequate measures of prevention, following an investigation to establish the probability that a certain phenomenon could materialize, assessing the level of vulnerability of that territory (Monteleone & Sabatino, 2014). The continuous analysis of geographical, environmental and geological data would be essential to conduct necessary research to apply the prevention measures to limit the effect of the events, and where possible to avoid the materialization of such events. The hydrogeological instability causes an increase in economic costs, due to the higher costs of the infrastructure and the maintenance of the services, and furthermore the cost of human lives when such disasters occur (Lai et al., 2021). It is important to highlight that the hydrogeological instability events are recurrent and for this reason, they occurred previously in the same area and will likely happen again with varying severity. For instance, landslides are extremely dangerous events and it is essential to investigate the movements of the slope. It is imperative to conduct a hazard assessment of the landslide, not limited to the necessity to establish the level of vulnerabilities in the specific area, but also to monitor continuously the evolution of the slope and its movements. Storms could trigger these events and nowadays we are experiencing an increase in the frequency and impact of these events due to climate change. The heavy precipitation events and the consequent damage are the main components of the damaging hydrogeological event (DHE). The massive urbanization might lead to an increase in flood vulnerability of the territory, given that the urbanization of the area would result in a change in the natural environment and weaken the natural harmony of the territory (Petrucci & Pasqua, 2008). An Italian study

suggested a methodology for the determination and classification of damaging hydrogeological events using historical data (Petrucci & Polemio, 2003). The study is assessing the specific hazard of the DHEs analysing the frequency, level of severity and level of damage to the specific area. The research has been conducted using the geographic information system (GIS) and collecting the historical data of the climate, the geomorphology and hydrogeology features of the affected areas, together with the information on the frequency of the DHEs and duration of such events (Petrucci & Polemio, 2003). The importance of the analysis of such events together with adequate infrastructure and prevention could reduce the impact on the environment and avoid the dangerous consequences for people affected by these events. In situations of heavy flood waves, the material that collapsed from the slope could power the exceptional transport of solids. When a riverbed narrows, rock and vegetative debris can create temporary barricades, which can be followed by flooding and / or sudden collapse of natural barricades. The instability of the slope, linked to important flows in the riverbed, could be caused by an extensive erosion activity on the bottom and on the bank of the river (APAT, 2006). In the case of coastal slopes, the main causes of erosion are attributable to the action of the wind and the sea. Most of these landslides are active and quiescent processes, mainly depending on the geolithological and morphological characteristics. These processes appear as collapses, as topples or, at most as articulations of these and other movements in a space-time sequence and therefore, as complex landslides (Vallejo, 1977; Sunamura, 1992; Edil, 2013). Additionally, it is important to understand the typology of materials and the state of activity of the instability phenomenon. The materials analysed are specifically:

• rock: it is a solid mass or aggregate of minerals.

• debris: it is an accumulation of fragments, and debris flows are formed by a mixture that includes materials such as sand and clay, together with pebbles and rocks, with an amount of water that may vary.

• soil: it is an unconsolidated mineral or organic material, that has a size usually lower than 2 mm, not amalgamated or might be damaged with moderate stresses or agitated by the water (Amanti et al., 1996).

When describing the state of activity of a gravitational phenomenon, the information regarding the frequency and timing of when the event occurred can be useful for research providing additional information on the estimation of the evolution's typology (Alexander, 1992). The state of activity of the phenomenon can be as follows:

- Active: whether the phenomenon is currently active or materialized recently in the last season; It can be further described as active, when the phenomenon is in movement, suspended, when the phenomenon materialized in the previous season's cycles but is not actually occurring and reactivated when the phenomenon is active after being inactive (Hadji et al., 2017).
- Dormant: the phenomenon is not actually occurring but it can materialize caused by the same previous causes of the movement (Giani, 1992).
- Stabilized: the phenomenon cannot be reactivated as it was naturally stabilized when the causes have been naturally removed and these causes are not influencing anymore the movement, or it was artificially stabilized when the human intervention avoids the occurrence, or it becomes a relict when the geomorphology that caused the movement has changed and therefore the event cannot occur anymore (Amanti et al., 1996).

Figure A1 describes the state of activity of the slope failure phenomenon.

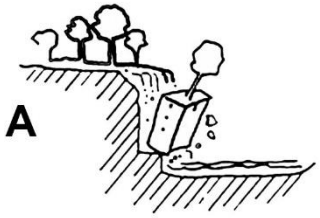

A. Active: The block topples are caused by erosion at the slope toe.

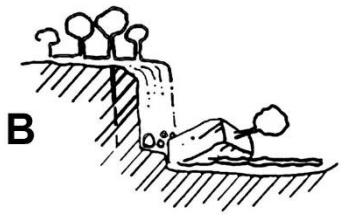

B. Suspended: there is a local crack in the crowning of the toppling.

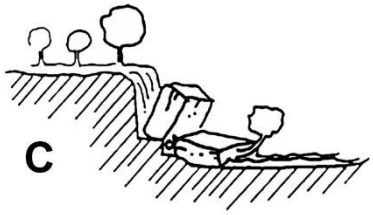

C. Reactivated: another block topples, disturbing the previously moved material.

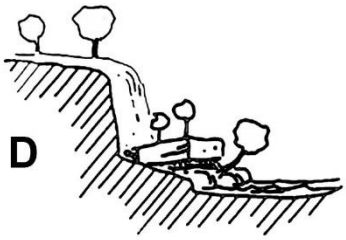

D. Dormant: the displaced mass resumes its vegetation cover; the slopes are modified by weathering.

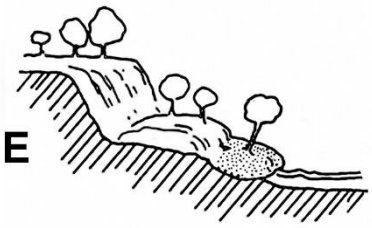

E. Naturally stabilized: the fluvial deposition has protected the toe of the slope and the escarpment resumes its vegetation cover.

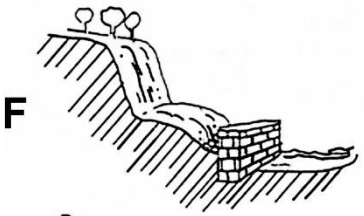

Artificially stabilized: a human intervention, a wall, protects the toe of the slope.

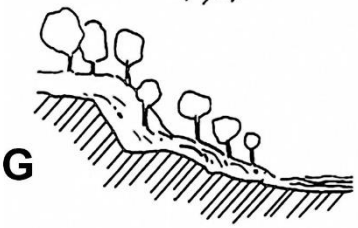

Relict: a uniform vegetation cover has been established.

A1: *The various states of activity of landslides (Adapted from Amanti et al., 1996).*

When forces operating on a slope are greater than the materials' resistance, a certain aggregate of rock is moved under the influence of gravity. The following factors all contribute to slope instability:

- a rise in tangential stresses caused by modifications to the slope's morphology (such as erosion, the building of monuments, etc.) and seismic activity.
- reduction in shear strength, which might be affected by changes in neutral or interstitial pressures, increase in apparent specific weight, enhancement in load and acclivity, reduction of the friction's angle, and decrease in cohesion as a consequence of changes in ranges of the soil resistance (Brunsden & Prior, 1984).

The causes of instability may be broken down into two categories:

1) structural or predisposing elements, which function primarily continuously over time.
2) triggering factors, which provide an external stimulus, even in a little period, causing the modification of natural proportions.

Intense meteorological events, quick melting of snow, increased erosion processes, earthquakes, etc. are the most common natural triggering variables (Loncke et al., 2009). As a result, one of the primary causes or triggers of gravitational events is due to meteorological circumstances. The triggering of the phenomenon is particularly favoured by the sequence of protracted dry spells and exceptionally potent and concentrated meteorological occurrences (Fiorucci et al., 2017). The various types of instability by gravitational phenomena are the following:

- Landslides: this phenomenon happens when the slope's stability conditions are altered, due to an increment in the load placed on the slope or by a reduction in the strength of the material that formed the slope. They entail a massive downhill movement of earth material caused by gravity. In order to create effective corrective procedures, it is crucial to identify the causes of the landslides. Determining the causes of a landslide in a particular location will also aid in defining the areas that are more likely to have landslides. Some examples of external causes might be earthquake vibrations, the load of buildings and reduction of the slope because of erosion or artificial excavations to build roads.

Examples of internal causes might be the growth of pore water pressure or the presence of faults (Prasad, 1995).

- Falls and topples: The movement of any size and kind of material (rocks, rubble, and soil) falling into open space is referred to as collapse. It is quick to highly rapid phenomenon that is exclusive to extremely steep slopes that protrude outward (overhanging slope). The toppling involves a rigid frontal rotation or an inflexion of a mass around a point or axis located below the centre of gravity of the mass itself. Some discontinuities, such as tectonic fracturing or contact surfaces between materials with different geotechnical characteristics, might cause the movement (Parise, 2002).
- Rotational slides: it happens when a rotary motion around a point or an axis located above the displaced mass's centre of gravity and away from the slope happens. Typically, the breaking surface is shaped like an arch with a concavity above (Fuchu & Sijing, 1999).
- Translational slides: it occurs with a planar motion over the smooth surface of pre-existing, quite smooth discontinuities, in the direction of the maximum slope (Eid, 2010).
- Flows: they are gradual deformations that occur inside the landslide body as a result of a strong differential plastic deformation. The saturating of the substance brought on by a rise in the water content is often what causes the movement (Cui et al., 2010).
- Rapid flows of debris and mud: They form like a torrent of sediments, typical of steeper mountain slopes, and spread downstream at often extremely high rates until stopping in flat regions or at substantial slope decreases (Coussot & Meunier,1996).
- Lateral spreads: they often happen when hard rocks overlying rocks and soil with a plastic behaviour (Arosio et al., 2019).
- Complex slope movements: The movement of the slope is characterized by a combination of various typologies of movements mentioned above (Barboux et al., 2014).
- Deep-seated gravitational slope deformations: It involves plastic, differential, and spatially continuous deformations along discontinuous surfaces, with very

gradual displacements—even on the scale of millimetres per year. In this manner, the moving rock mass is split into several sections that maintain a degree of structural coherence within them and go through processes of expanding and folding (Crosta et al., 2013).

- Slow superficial movements: phenomena caused by the constant and gradual movement of the layer of surface debris placed on slopes that take place without a clearly defined sliding surface because of the interaction of gravity and the other variables mentioned below. Solifluction and soil creeps are two categories of slow superficial movements (Kuhn & Mitchell,1993). The solifluction is a gradual mass loss caused by freezing (Matsuoka, 2001). The soil creeps are the consequence of an accumulated displacement of individual particles brought about by a series of minor partial movements brought by the continuous action of several sources in addition to the gravitational pull of gravity, such as the flow of water in the ground (Pawlik & Šamonil, 2018).
- Sinkholes: Both the bedrock and the soil include voids and cavities that are relevant as possible collapse locations. So, before beginning construction, it is necessary to examine the risk of sinking caused by them (Gongyu & Wanfang,1999).

One of the significant morphological factors is rainwater, which has enormous geomorphological impacts associated with both its direct effect on the soil, or raindrop erosion, and the movement of water on the surface, or runoff (Kinnell, 2005). Rainwater can partially stream on the surface if it is mildly sloped, creating a clear surface flow depending on the maximum slope, and partially penetrate deeply into the soil and subsoil when it comes to the surface. This process allows granules, such as soil and rock, to be removed from the soil level and transported down the slope, where the eroded particles can build up and create masses known as colluvial deposits (colluvium) (Mücher et al., 2018).

1. Splash erosion: it is the first step of soil erosion by water and is caused by raindrops acting damagingly on soil surface particles (Zambon et al., 2021). It occurs uniformly in every direction when raindrops fall directly on a horizontal plane. More sediment is splashed downhill during a wind-driven downpour than

upwards due to slopes, and splash movement is influenced by both wind direction and slope steepness (Warren, 2010).

2. Sheet erosion: without penetrating the soil, rainwater reaches the surface in a dispersed manner, forming a thick network of water lines that are disseminated differently from one rainfall event to the next on the slope. Throughout this instance, the rainfall is arranged into threads that cause area-wide erosion on the slopes, with differing intensity depending on the slope's gradient and the existence of obstacles in its route (Morin & Van Winkel, 1996).
3. Rill erosion: the water's thin layer gravitates toward narrow channels known as rills" as it travels below. These rills, which bend and pierce the ground, resemble little rivers.
4. Raindrops are still disintegrating the ground at this time, but runoff has also gained enough speed to rip loose soil fragments. Moreover, rills are quite effective in moving soil debris. Depending on the slope's length and steepness, running water can cause varying amounts of damage (Warren, 2010).
5. Gully erosion: in a short amount of time, surface water removes the soil surface and the underlying undistributed rock substrate, resulting in the formation of a sharp channel with a consistent depth, called gullies, and multiple levels in the channel thalweg (Rădoane & Rădoane, 2017).

Sedimentation occurs when the soil is depositing. Ponds form whenever the drainage water flow is disrupted. Additionally, soil fragments in the water sink to the soil as ponds form (Warren, 2010).

In torrential streams, which often constitute the hydrographic network of mountainous regions and are characterized by a steep slope, rapid and severe pulsations of floods might take place in conjunction with extreme weather conditions or the abrupt melting of snow. Such floods have the potential to significantly alter the torrential courses and the fan areas at the entrances of the major valleys, potentially having very negative impacts on the buildings and infrastructures that are caught in their passage (Bezak et al., 2019). Debris torrents are determined as quick, channelled streams of saturated, insufficiently patterned non-plastic soil and detritus. The main difference with the debris avalanches is because they are not channelled (Slaymaker,1988). Due to the fast spread and short corrosion times, which are often caused by the small size of the hydrographic

regions occupied by the waterways, these phenomena evolve quickly. Floods outside the riverbed can also result in severe lateral erosion, eroding the slope's foundation and setting off landslides (Huebl et al., 2017).

Snowfalls that swiftly drop steep slopes are known as snow avalanches. They may be made of ice, vegetation, sediment, or rocks. There are two different typologies:

- Slab avalanches: a section in a generally reduced-cohesion topsoil from dry or wet snow is where loose snow avalanches begin (Schweizer et al., 2003).
- Loose snow avalanches: similar to the linear collapse of rock slopes rather than the rotational fall of soil slopes, snow slab avalanches entail the release of a homogeneous block along a long plane of weakness (Schweizer et al., 2003).

One of the most devastating events that occur in mountainous regions is the fall of snow avalanches; in fact, it is one of the most significant geological-hydraulic instability events in these regions. The passage of an avalanche up a slope, results in the removal of everything it comes into contact with (debris, vegetation, etc.), the digging of an avalanche corridor, and eventually the dispersal of the mass at the slope's base, where conoids or elongated and asymmetrical lumps are formed. In the absence of snow, the cleaning water or the detritus that lands on the ground by gravity emphasizes and/or remodels these features (Luckman, 1977). Avalanches are able to absorb all the material they come into contact with along their journey, which accounts for the remarkable variability of the detritus deposit they generate at the bottom of slopes. In fact, the avalanche-generated debris accumulations are constituted of irregularly deposited materials that lack any sedimentary structure where blocks of gigantic proportions, fine clay, or silty might coexist (Mellor, 1968).

Appendix II: Rebound, sliding/rolling and transition parameters (information retrieved from from RocPro3D v. 5.7.7 - User's guide - Copyright © 2020 ROCPRO3D)

The rebound parameters are divided in three sets: the coefficients and variables of velocity restitution (Restitution coefficients box), the variables related to lateral deviation of the

rebound (Lateral deviation box) and the variables related to flattening of the rebound angle (Rebounds flattening box).

- In the restitution coefficients box there are:

· Normal value Rn (uniform) or Mean normal value μ _Rn (Gaussian) = restitution coefficient (0 to 1) applied to the normal velocity component.

· Tangential value Rt (uniform) or Mean tangential value μ_Rt (Gaussian) = restitution coefficient (0 to 1) applied to the tangential velocity component.

· Variability Δ_R (uniform, expressed in %) or Standard deviation σ_R (Gaussian, dimensionless) = probabilistic component affecting the restitution coefficients as long as velocity is lower than V_R. It depends on velocity, and tends progressively towards the limit variability (or standard deviation) when the velocity tends towards the limit velocity V_R.

· Limit velocity V_R = limit velocity, expressed in metre per second, above which the applied variability is the limit variability (or standard deviation).

· Limit variability Δ_R(lim) (uniform, expressed in %) or Limit standard deviation σ_R(lim) (Gaussian, dimensionless) = probabilistic component affecting the restitution coefficients as long as velocity is higher than V_R. Its value is fixed as it does not depend on velocity anymore. It is generally lower than Δ _R or σ_R, to reflect the fact that a block is more sensitive to uncertainties (terrain heterogeneities, block shape irregularity...) at low velocities than at larger ones.

- In the lateral deviation box there are:

· Variability Δ _θh (uniform) or Standard deviation σ_θh (Gaussian) = probabilistic component (in degrees) affecting the lateral deviation as long as velocity is lower than V_θh. It depends on velocity, and tends progressively towards the limit variability (or standard deviation) when the velocity tends towards the limit velocity V_θh.

· Limit velocity V_θh = limit velocity, expressed in metre per second, above which the applied variability is the limit variability (or standard deviation).

· Limit variability Δ_θh(lim) (uniform) or Limit Standard deviation σ_θh(lim) (Gaussian) = probabilistic component (in degrees) affecting the lateral deviation as long as velocity is higher than V_θh. Its value is fixed as it does not depend on velocity anymore. It is generally lower than Δ_θh or σ_θh, to reflect the fact that a block is more sensitive to uncertainties (terrain heterogeneities, block shape irregularity...) at low velocities than at larger ones.

- In the Rebounds flattening box there are:

· Variability Δ_θv (uniform) or Standard deviation σ_θv (Gaussian) = probabilistic component (in degrees) affecting the rebounds flattening as long as velocity is lower than V_θv. It depends on velocity, and tends progressively towards the limit variability (or standard deviation) when the velocity tends towards the limit velocity V_θv.

· Limit velocity V_θv = limit velocity, expressed in metre per second, above which the applied variability is the limit variability (or standard deviation).

· Limit variability Δ_θv(lim) (uniform) or Limit Standard deviation σ_θv(lim) (Gaussian) = probabilistic component (in degrees) affecting the rebounds flattening as long as velocity is higher than V_θv. Its value is fixed as it does not depend on velocity anymore. It is generally lower than Δ_θv or σ_θv, to reflect the fact that a block is more sensitive to uncertainties (terrain heterogeneities, block shape irregularity...) at low velocities than at larger ones.

Frictional sliding (lumped mass formulation) or frictional rolling (rigid block formulation) equations are used in RocPro3D to model the block moving onto the terrain without rebound. The parameters consist of the coefficients and variables defined in the Friction coefficient box.

- In the friction coefficient box there are:

· Friction k = dynamic friction coefficient, corresponding to the tangent of the dynamic friction angle.

· Variability Δ_k (uniform, expressed in %) or Standard deviation σ_k (Gaussian, dimensionless) = probabilistic component affecting the restitution coefficients as long as velocity is lower than V_k. It depends on velocity, and tends progressively towards

the limit variability (or standard deviation) when the velocity tends towards the limit velocity V_k.

· Limit velocity V_k = limit velocity, expressed in metre per second, above which the applied variability is the limit variability (or standard deviation).

· Limit variability Δ_k(lim) (uniform, expressed in %) or Limit standard deviation σ_k(lim) (Gaussian, dimensionless) = probabilistic component affecting the friction coefficient as long as velocity is higher than V_k. Its value is fixed as it does not depend on velocity anymore. It is generally lower than Δ_k or σ_k, to reflect the fact that a block is more sensitive to uncertainties (terrain heterogeneities, block shape irregularity...) at low velocities than at larger ones.

The transitions parameters consist of the limit angles defining the transitions between free fall and rolling/sliding trajectories portions.

- They are defined in the Transitions parameters box.

Transitions FF->R and R->FF (acute case) box

This box allows defining the limit Angle β_lim, expressed in degrees, which is used to manage transitions in the two following cases:

· Free fall (FF) -> Sliding/Rolling (R) : after impact, if the angle between the trajectory and the terrain (the face) is lower than Angle β_lim, the block enters in a sliding/rolling kinematic portion (see Transitions between free fall and sliding/rolling, cases a and b).

· Sliding/Rolling (R) -> Free fall (FF) in the case where the topography is flat or convex: starting from sliding/rolling, if the angle between the trajectory and the terrain (the face) is larger than angle β_lim the block enters a free fall kinematic portion (see Transitions between free fall and sliding/rolling, case c).

Transition R->FF (obtuse case) box

This box allows defining the limit Angle β_lim', expressed in degrees, which is used to manage the transition Sliding/Rolling (R) -> Free fall (FF) in the case where the topography is concave: starting from sliding/rolling, if the angle between the trajectory and the terrain (the face) is larger than Angle β_lim', the block rebounds and enters a free fall kinematic portion. In other words, the terrain acts here as a barrier (see Transitions between free fall and sliding/rolling,

case e).

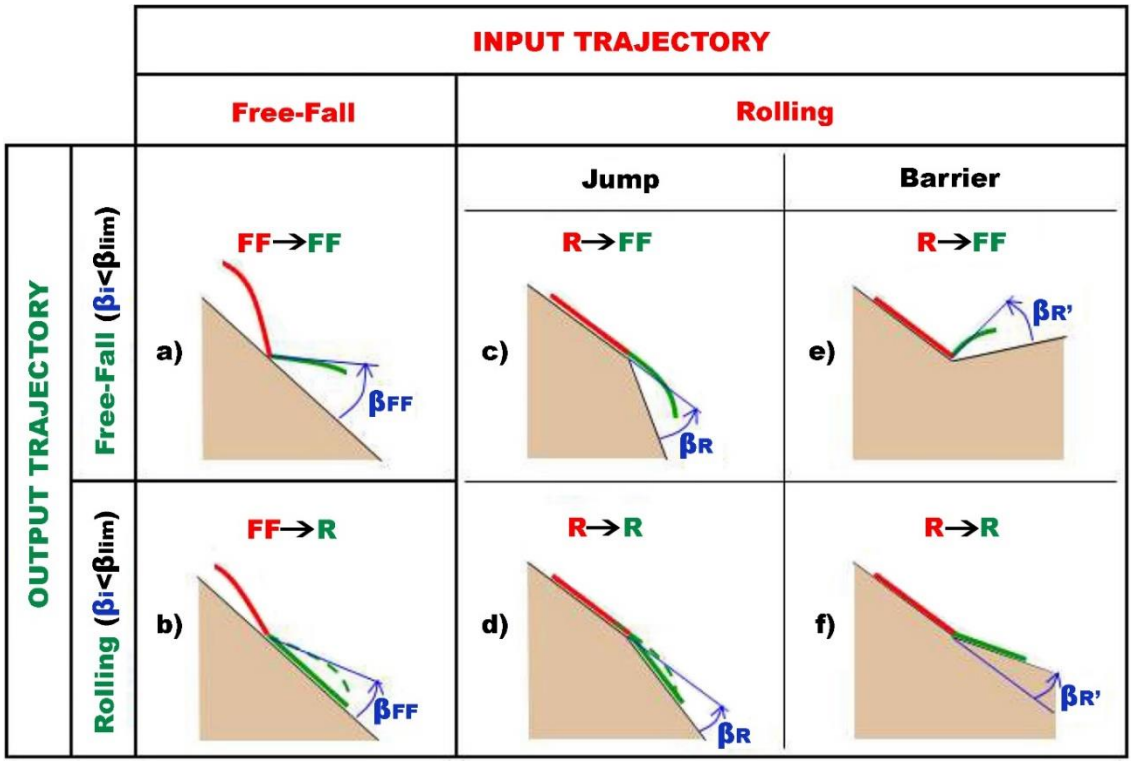

A2: Scheme defining the transitions between free fall and rolling/sliding trajectories (Retrieved from RocPro3D v. 5.7.7 User's guide - Copyright © 2020 ROCPRO3D).

References

3DFlow (2021), retrieved from: https://www.3dflow.net/. Accessed 20 July 2021.

Agisoft LLC, St Petersburg R (2021) Agisoft metashape professional Edition, retrieved from: https://www.agisoft.com/. Accessed on 18 September 2022.

Agliardi, F., Crosta, G. B., & Frattini, P. (2009). Integrating rockfall risk assessment and countermeasure design by 3D modelling techniques. Natural Hazards and Earth System Sciences, 9(4), 1059-1073.

Ahmed, Mohammed. (2014). Fundamental of Applied Geophysics. 10.13140/2.1.4322.3364.

Alexander, D. (1992). On the causes of landslides: Human activities, perception, and natural processes. *Environmental geology and water sciences*, *20*(3), 165-179.

Alfaro, P., Delgado, J., Esposito, C., Tortosa, F. G., Marmoni, G. M., & Martino, S. (2019). Time-dependent modelling of a mountain front retreat due to a fold-to-fault controlled lateral spreading. Tectonophysics, 773, 228233.

Ali, J., Abdullah, N., Ismail, M. Y., Mohd, E., & Shah, S. M. (2017). Ultra-wideband antenna design for GPR applications: A review. *International Journal of Advanced Computer Science and Applications*, 8(7).

Ali, E. (2020). Geographic Information System (GIS): Definition, Development, Applications & Components. *Department of Geography, Ananda Chandra College. India*.

Alisiobi, A. R., & Ako, B. D. (2012, April). Groundwater investigation using combined geophysical methods. In *AAPG annual convention poster presentation*.

Amanti, Marco & Casagli, Nicola & Catani, Filippo & DOrefice, Maurizio & G., Motteran. (1996). Guida al censimento dei fenomeni franosi ed alla loro archiviazione. *Miscellanea Servizio Geologico d'Italia*. 7. 109.

Annan, A. P. (2002). GPR—History, trends, and future developments. Subsurface sensing technologies and applications, 3(4), 253-270.

Annan, P. (2003). Ground penetrating radar principles, procedures and applications. *Sensors and software*, *278*.

Annan, A. P. (2005). Ground-penetrating radar. In Near-surface geophysics (pp. 357-438). *Society of Exploration Geophysicists*.

APAT, (2006). Fenomeni di dissesto geologico – idraulico sui versanti. Classificazione e simbologia. *Agenzia per la protezione dell'ambiente e per i servizi tecnici. Manuali e Linee Guida 39/2006*.

Arfaoui, A. (2017). Unmanned aerial vehicle: Review of onboard sensors, application fields, open problems and research issues. *Int. J. Image Process, 11(1), 12-24.*

Arosio, D., Longoni, L., Papini, M., Bièvre, G., & Zanzi, L. (2019). Geological and geophysical investigations to analyse a lateral spreading phenomenon: the case study of Torrioni di Rialba, northern Italy. *Landslides*, *16*(7), 1257-1271.

Autodesk ReCap Photo, 2021 Autodesk Knowledge Network: Recap Photo https://knowledge.autodesk.com/support/recap/. Accessed on 18 September 2022.

Baldassini, N., Mazzei, R., Foresi, L. M., & Riforgiato, F. (2013). Calcareous plankton bio-chronostratigraphy of the Maltese Lower Globigerina Limestone member. *Acta Geologica Polonica*, *63*(1), 105-135.

Balestrieri, E., Daponte, P., De Vito, L., & Lamonaca, F. (2021). Sensors and measurements for unmanned systems: An overview. Sensors, 21(4), 1518.

Bard, P.Y., 2005. Guidelines for the implementation of the H/V spectral ratio technique on ambient vibrations: measurements, processing, and interpretations, *SESAME European Research Project.* WP12, deliverable D23.12, 2004.

Barnichon, J. D. RocPro3D v5.7.11 x64 (2022). http://www.rocpro3d.com/download_en.php Accessed on 18 September 2022.

Barton, N. (1978). Suggested methods for the quantitative description of discontinuities in rock masses. ISRM, *International Journal of Rock Mechanics and Mining Sciences & Geomechanics Abstracts,* 15(6), 319-368.

Baker, G. S., Jordan, T. E., & Pardy, J. (2007). An introduction to ground penetrating radar (GPR). *Special Papers-Geological Society of America, 432, 1.*

Barboux, C., Delaloye, R., & Lambiel, C. (2014). Inventorying slope movements in an Alpine environment using DInSAR. *Earth surface processes and landforms*, *39*(15), 2087-2099.

Bento, M. D. F. (2008). Unmanned aerial vehicles: an overview. *Inside GNSS, 3(1), 54-61*.

Berge, M. A., & Drahor, M. G. (2011). Electrical resistivity tomography investigations of multilayered archaeological settlements: part I–modelling. *Archaeological Prospection, 18(3), 159-171.*

Bezak, N., Sodnik, J., & Mikoš, M. (2019). Impact of a random sequence of debris flows on torrential fan formation. *Geosciences*, *9*(2), 64.

Bianchini Ciampoli, L., Tosti, F., Economou, N., & Benedetto, F. (2019). Signal processing of GPR data for road surveys. *Geosciences, 9(2), 96.*

Biolchi, S., Furlani, S., Devoto, S., Gauci, R., Castaldini, D., & Soldati, M. (2016). Geomorphological identification, classification and spatial distribution of coastal landforms of Malta (Mediterranean Sea). *Journal of Maps*, *12*(1), 87-99.

Bird, E. (2008). Coastal Geomorphology: an Introduction. *John Wiley, Chichester, U*.

Bozzano, F., Bretschneider, A., & Martino, S. (2008). Stress–strain history from the geological evolution of the Orvieto and Radicofani cliff slopes (Italy). Landslides, 5(4), 351-366.

Bozzano, F., Martino, S., & Prestininzi, A. (2010). Ruolo dell'assetto geologico sulle condizioni di stabilità della collina di Gerace (Reggio Calabria, Italia). Italian journal of geosciences, 129(2), 280-296.

Bozzano, F., Bretschneider, A., Esposito, C., Martino, S., Prestininzi, A., & Mugnozza, G. S. (2013). Lateral spreading processes in mountain ranges: Insights from an analogue modelling experiment. Tectonophysics, 605, 88-95.

Brunsden, D., & Prior, D. B. (1984). Slope instability.

Budetta, P., & Santo, A. (1994). Morphostructural evolution and related kinematics of rockfalls in Campania (southern Italy): A case study. Engineering Geology, 36(3-4), 197-210.

Budhathoki, N. R., & Nedovic-Budic, Z. (2008). Reconceptualizing the role of the user of spatial data infrastructure. *GeoJournal*, 72(3-4), 149-160.

Buyer, A., Aichinger, S., & Schubert, W. (2020). Applying photogrammetry and semi-automated joint mapping for rock mass characterization. Engineering Geology, 264, 105332.

Cardarelli, E., Marrone, C., & Orlando, L. (2003). Evaluation of tunnel stability using integrated geophysical methods. *Journal of Applied Geophysics*, *52*(2-3), 93-102.

Carrière, S. D., Chalikakis, K., Sénéchal, G., Danquigny, C., & Emblanch, C. (2013). Combining electrical resistivity tomography and ground penetrating radar to study geological structuring of karst unsaturated zone. *Journal of Applied Geophysics*, *94*, 31-41.

Casella E, Collin A, Harris D, Ferse S, Bejarano S, Parravicini V, Rovere A (2017) Mapping coral reefs using consumer-grade drones and structure from motion photogrammetry techniques. *Coral Reefs* 36(1):269–275

Caselle, C., Bonetto, S., Comina, C., & Stocco, S. (2020). GPR surveys for the prevention of karst risk in underground gypsum quarries. *Tunnelling and Underground Space Technology, 95, 103137.*

Chandler, J. (1999). Effective application of automated digital photogrammetry for geomorphological research. *Earth surface processes and landforms*, 24(1), 51-63.

Chen, S., F Laefer, D., & Mangina, E. (2016). State of technology review of civilian UAVs. *Recent Patents on Engineering, 10(3), 160-174.*

CloudCompare (version 2.10) [GPL software] (2018) Retrieved from: http://www.cloudcompare.org/. Accessed on 18 September 2022

Colica, E., Micallef, A., D'Amico, S., Cassar, L. F., & Galdies, C. (2017). Investigating the use of UAV systems for photogrammetric applications: a case study of Ramla Bay (Gozo, Malta).

Colica, E., Antonazzo, A., Auriemma, R., Coluccia, L., Catapano, I., Ludeno, G., ... & Persico, R. (2021). GPR investigation at the archaeological site of Le Cesine, Lecce, Italy. *Information*, *12*(10), 412.

Colica, E., D'Amico, S., Iannucci, R., Martino, S., Gauci, A., Galone, L., ... & Paciello, A. (2021). Using unmanned aerial vehicle photogrammetry for digital geological surveys: case study of Selmun promontory, northern of Malta. *Environmental Earth Sciences*, *80*(17), 1-14.

Collischonn, W., & Pilar, J. V. (2000). A direction dependent least-cost-path algorithm for roads and canals. *International Journal of Geographical Information Science*, *14*(4), 397-406.

Corominas, J., Mavrouli, O., & Ruiz-Carulla, R. (2017, May). Rockfall occurrence and fragmentation. In Workshop on world landslide forum (pp. 75-97). Springer, Cham.

Coussot, P., & Meunier, M. (1996). Recognition, classification and mechanical description of debris flows. *Earth-Science Reviews*, *40*(3-4), 209-227.

Crosby C, Nandigam V, Baru C, Arrowsmith JR. (2013). Opentopography: enabling online access to high-resolution lidar topography data and processing tools. In: *EGU general assembly conference abstracts* (p 13326).

Crosta, G. B., Frattini, P., & Agliardi, F. (2013). Deep seated gravitational slope deformations in the European Alps. *Tectonophysics*, *605*, 13-33.

Cui, P., Dang, C., Cheng, Z., & Scott, K. M. (2010). Debris flows resulting from glacial-lake outburst floods in Tibet, China. *Physical Geography*, *31*(6), 508-527.

D'Amico S., Lombardo G., Panzera F. (2013). Seismicity of the Mediterranean Region and mitigation of earthquake losses. *Physics and Chemistry of the Earth*, 63, 1-2, doi:10.1016/j.pce.2013.07.001

D'Amico S, Saccone M, Persico R, Venuti V, Spagnolo G, Crupi V, Majolino D (2017) 3D survey and GPR for cultural heritage. The case study of SS. Pietro and Paolo Church in Casalvecchio Siculo. *Kermes* 107:11–15

Daniels, J. J., & Dyck, A. V. (1984). Borehole resistivity and electromagnetic methods applied to mineral exploration. *IEEE Transactions on Geoscience and Remote Sensing*, (1), 80-87.

Daniels, J. J. (2000). Ground penetrating radar fundamentals. *Prepared as an appendix to a Report to the US EPA, Region V, 1-21*.

Davis, J. L., & Annan, A. P. (1989). Ground-penetrating radar for high-resolution mapping of soil and rock stratigraphy 1. *Geophysical prospecting, 37(5), 531-551*.

Deidun, A., Azzopardi, M., Saliba, S., & Schembri, P. J. (2003). Low faunal diversity on Maltese sandy beaches: fact or artefact? *Estuarine, coastal and shelf science*, *58*, 83-92.

Devoto, S., Biolchi, S., Bruschi, V. M., Furlani, S., Mantovani, M., Piacentini, D., ... & Soldati, M. (2012). Geomorphological map of the NW Coast of the Island of Malta (Mediterranean Sea). *Journal of Maps*, *8*(1), 33-40.

Devoto S, Biolchi S, Bruschi VM, Díez AG, Mantovani M, Pasuto A, Soldati M. (2013). Landslides along the north-west coast of the Island of Malta. In: Margottini C, Canuti P, Sassa K (eds) *Landslide science and practice*. Springer, Berlin

Edil, T. B. (2013). Erosion of Coastal Slopes and Landslides. In *Geo-Congress 2013: Stability and Performance of Slopes and Embankments III* (pp. 1320-1334).

Eid, H. T. (2010). Two-and three-dimensional analyses of translational slides in soils with nonlinear failure envelopes. *Canadian Geotechnical Journal*, *47*(4), 388-399.

El Gamal A., Eltoukhy H. (2005). CMOS image sensors. *Engineering, IEEE Circuits and Devices Magazine.* 21, 6-20. DOI:10.1109/MCD.2005.1438751Corpus ID: 8813059

Eltner, A., & Sofia, G. (2020). Structure from motion photogrammetric technique. In Developments in Earth surface processes (Vol. 23, pp. 1-24). *Elsevier.*

Ercoli, M., Pauselli, C., Frigeri, A., Forte, E., & Federico, C. (2013). "Geophysical paleoseismology" through high resolution GPR data: A case of shallow faulting imaging in Central Italy. *Journal of Applied Geophysics, 90, 27-40.*

Farrugia D., Paolucci E., D'Amico S., Galea P. (2016). Inversion of surface-wave data for subsurface shear-wave velocity profiles characterised by a thick buried low-velocity layer. *Geophysical Journal International*, 206, 1221-1231, doi:10.1093/gji/ggw204

Felix, R. (1973). Oligo-miocene stratigraphy of Malta and Gozo (No. 73-20). *Veenman.*

Fernández, O. (2005). Obtaining a best fitting plane through 3D georeferenced data. *Journal of Structural Geology*, *27*(5), 855-858.

Fiorucci, M., Iannucci, R., Lenti, L., Martino, S., Paciello, A., Prestininzi, A., & Rivellino, S. (2017). Nanoseismic monitoring of gravity-induced slope instabilities for the risk management of an aqueduct infrastructure in Central Apennines (Italy). *Natural Hazards*, *86*(2), 345-362.

Fonstad MA, Dietrich JT, Courville BC, Jensen JL, Carbonneau PE (2013) Topographic structure from motion: a new development in photogrammetric measurement. *Earth Surf Process Landf 38*(4):421–430

Formosa, S. (2017). Sensing the SIntegraM: a two-decadal endeavour for spatial data harmonisation and governance. In S. Formosa (Ed.), *Emergent realities for social wellbeing: environmental, spatial and social pathways* (pp. 75-94). Malta: University of Malta. Department of Criminology.

Francioni M, Salvini R, Stead D, Litrico S (2014) A case study integrating remote sensing and distinct element analysis to quarry slope stability assessment in the Monte Altissimo area, Italy. *Eng Geol* 183:290–302

Fuchu, D., Lee, C. F., & Sijing, W. (1999). Analysis of rainstorm-induced slide-debris flows on natural terrain of Lantau Island, Hong Kong. *Engineering Geology*, *51*(4), 279-290.

Furlani, S., Pappalardo, M., Gomez-Pujol, L., & Chelli, A. (2014). The rock coast of the mediterranean and black seas. In D. M. Kennedy, W. J. Stephenson, & L. Naylor (Eds.), Rock coast geomorphology: A global synthesis (Vol. 40, pp. 89–122). *Avon: Geological Society Memoirs, published by Geological Society Publishing House.*

Galea, P., D'Amico, S., & Farrugia, D. (2014). Dynamic characteristics of an active coastal spreading area using ambient noise measurements—Anchor Bay, Malta. *Geophysical Journal International*, *199*(2), 1166-1175.

Galea P., Bozionelos G., D'Amico S., Drago A., Colica E. (2018) Seismic Signature of the Azure Window Collapse, Gozo, Central Mediterranean. *Seismological Research Letters*, 89, 3 May/June 2018, doi: 10.1785/0220170115

Galea P, Bozionelos G, D'Amico S, Drago A, Colica E (2018) Seismic signature of the azure window collapse, Gozo, Central Mediterranean. *Seismol Res Lett* 89(3):1108–1117.

Gallo, I. G., Martínez-Corbella, M., Sarro, R., Iovine, G., López-Vinielles, J., Hérnandez, M., ... & García-Davalillo, J. C. (2021). An Integration of UAV-Based Photogrammetry and 3D Modelling for Rockfall Hazard Assessment: The Cárcavos Case in 2018 (Spain). Remote Sensing, 13(17), 3450.

Gauci, R., & Scerri, S. (2019). A synthesis of different geomorphological landscapes on the Maltese Islands. In *Landscapes and Landforms of the Maltese Islands* (pp. 49-65). Springer, Cham.

Giani, G. P. (1992). Rock slope stability analysis. *CRC Press.*

Gigli, G., Frodella, W., Mugnai, F., Tapete, D., Cigna, F., Fanti, R., ... & Lombardi, L. (2012). Instability mechanisms affecting cultural heritage sites in the Maltese Archipelago. *Natural hazards and earth system sciences*, *12*(6), 1883-1903.

Girardeau-Montaut D (2015) Cloud compare—3d point cloud and mesh processing software. Open Source Project.

Global Mapper®, blue marble geographics (2022), retrieved from: https://www.bluemarblegeo.com/global-mapper/. Accessed on 18 September 2022.

Gomarasca, M. A. (2010). Basics of geomatics. *Applied Geomatics, 2(3),* 137-146.

Gonçalves JA, Henriques R (2015) UAV photogrammetry for topographic monitoring of coastal areas. ISPRS J *Photogramm Remote Sens* 104:101–111

Goudie A. (2004). Encyclopedia of geomorphology. Routledge

Gongyu, L., & Wanfang, Z. (1999). Sinkholes in karst mining areas in China and some methods of prevention. *Engineering Geology*, *52*(1-2), 45-50.

Grandjean, G., & Gourry, J. C. (1996). GPR data processing for 3D fracture mapping in a marble quarry (Thassos, Greece). *Journal of Applied Geophysics*, *36*(1), 19-30.

Grosse P, van de Vries WB, Euillades PA, Kervyn M, Petrinovic IA (2012) Systematic morphometric characterization of volcanic edifices using digital elevation models. *Geomorphology 136*(1):114–131

Günther, A., Reichenbach, P., Malet, J. P., Van Den Eeckhaut, M., Hervás, J., Dashwood, C., & Guzzetti, F. (2013). Tier-based approaches for landslide susceptibility assessment in Europe. *Landslides*, *10*(5), 529-546.

Guzzetti, F., Carrara, A., Cardinali, M., & Reichenbach, P. (1999). Landslide hazard evaluation: a review of current techniques and their application in a multi-scale study, Central Italy. *Geomorphology*, *31*(1-4), 181-216.

Guzzetti, F., Reichenbach, P., & Wieczorek, G. F. (2003). Rockfall hazard and risk assessment in the Yosemite Valley, California, USA. Natural Hazards and Earth System Sciences, 3(6), 491-503.

Hadji, R., Rais, K., Gadri, L., Chouabi, A., & Hamed, Y. (2017). Slope failure characteristics and slope movement susceptibility assessment using GIS in a medium scale: a case study from Ouled Driss and Machroha municipalities, Northeast Algeria. *Arabian Journal for Science and Engineering*, *42*(1), 281-300.

Halliday, D., Resnick, R., & Walker, J. (2013). *Fundamentals of physics*. John Wiley & Sons.

Harris, R., & Browning, R. (2003). Global monitoring for environment and security: Data policy considerations. *Space Policy, 19(4),* 265-276.

Heng BCP, Chandler JH, Armstrong A (2010) Applying close range digital photogrammetry in soil erosion studies. *Photogramm Record 25*(131):240–265

Huebl, J., Nagl, G., Suda, J., & Rudolf-Miklau, F. (2017). Standardized stress model for design of torrential barriers under impact by debris flow (according to Austrian Standard Regulation 24801). *International Journal of Erosion Control Engineering*, *10*(1), 47-55.

Hunt, C. O. (1997). Quaternary deposits in the Maltese Islands: a microcosm of environmental change in Mediterranean lands. *GeoJournal*, *41*(2), 101-109.

Hunt, C. O., & Schembri, P. J. (1999). Quaternary environments and biogeography of the Maltese Islands.

Hutchinson J.N. (1988). General report: morphological and geotechnical parameters of landslides in relation to geology and hydrogeology. In: *proceedings of fifth international symposium on landslides, vol 1,* p 3–35

Hyde HPT (1955) Geology of the Maltese Islands. *Lux Press,* Montreal.

Iannucci R, Martino S, Paciello A, D'Amico S (2017) Rock mass characterization coupled with seismic noise measurements to analyze the unstable cliff slope of the Selmun promontory (Malta). *Proced Eng* 191:263–269

Iannucci, R., Martino, S., Paciello, A., D'Amico, S., & Galea, P. (2018). Engineering geological zonation of a complex landslide system through seismic ambient noise measurements at the Selmun Promontory (Malta). *Geophysical Journal International*, *213*(2), 1146-1161.

Iannucci, R., Martino, S., Paciello, A., D'Amico, S., & Galea, P. (2020). Investigation of cliff instability at Għajn Ħadid Tower (Selmun Promontory, Malta) by integrated passive seismic techniques. *Journal of Seismology*, *24*(4), 897-916.

Imam, E. (2018). Aerial Photography and Photogrammetary. Remote Sensing and GIS.

IRIS instruments, Prosys III Resistivity data management, updated for 3D acquisition, version 2.02, retrieved from http://www.iris-instruments.com/download.html. Accessed on 18 September 2022

Jaboyedoff, M., Oppikofer, T., Abellán, A., Derron, M. H., Loye, A., Metzger, R., & Pedrazzini, A. (2012). Use of LIDAR in landslide investigations: a review. *Natural hazards*, *61*(1), 5-28.

James, M. R., & Robson, S. (2014). Mitigating systematic error in topographic models derived from UAV and ground-based image networks. *Earth Surface Processes and Landforms*, *39*(10), 1413-1420.

Jeler, G. E. (2020). Brief historical milestones on the evolution of UAV systems: 1914-1939. *Bulletin of" Carol I" National Defence University (EN), (03),* 137-143.

Jeremic, A., Thornton, M., & Duncan, P. (2016). Ambient passive seismic imaging with noise analysis. *In 2016 SEG International Exposition and Annual Meeting. OnePetro*.

Jol, H. M. (Ed.). (2008). Ground penetrating radar theory and applications. *Elsevier.*

Jongmans, D., & Garambois, S. (2007). Geophysical investigation of landslides: a review. *Bulletin de la Société géologique de France*, *178*(2), 101-112.

Kana, J. D., Djongyang, N., Raïdandi, D., Nouck, P. N., & Dadjé, A. (2015). A review of geophysical methods for geothermal exploration. *Renewable and Sustainable Energy Reviews*, *44*, 87-95.

Kinnell, P. I. A. (2005). Raindrop-impact-induced erosion processes and prediction: a review. *Hydrological Processes: An International Journal*, *19*(14), 2815-2844.

Koppenjan, S. (2009). Ground penetrating radar systems and design. *Ground penetrating radar: Theory and applications*, *1*.

Kuhn, M. R., & Mitchell, J. K. (1993). New perspectives on soil creep. *Journal of Geotechnical Engineering*, *119*(3), 507-524.

Kukko, A. (2013). Mobile Laser Scanning–System development, performance and applications. *Finnish Geodetic Institute.*

Lai, S., Isola, F., Leone, F., & Zoppi, C. (2021). Assessing the potential of green infrastructure to mitigate hydro-geological hazard. *TeMA-Journal of Land Use, Mobility and Environment*, 109-133.

Lane SN (2000) The measurement of river channel morphology using digital photogrammetry. *Photogramm Rec 16*(96):937–961

Laribi A, Walstra J, Ougrine M, Seridi A, Dechemi N (2015) Use of digital photogrammetry for the study of unstable slopes in urban areas: case study of the El Biar landslide, Algiers. *Eng Geol* 187:73–83

Leachtenauer JC, Driggers RG (2001) Surveillance and reconnaissance imaging systems: modeling and performance prediction. *Artech House.*

Leucci, G., Persico, R., De Giorgi, L., Lazzari, M., Colica, E., Martino, S., ... & D'Amico, S. (2021). Stability Assessment and Geomorphological Evolution of Sea Natural Arches by Geophysical Measurement: The Case Study of Wied Il-Mielah Window (Gozo, Malta). *Sustainability, 13(22), 12538.*

Li R, Di K, Ma R (2003) 3-D shoreline extraction from IKONOS satellite imagery. *Mar Geodesy 26*(1–2):107–115

Li, L., & Lan, H. (2015). Probabilistic modeling of rockfall trajectories: a review. Bulletin of Engineering Geology and the Environment, 74(4), 1163-1176.

Li, X., Chen, Z., Chen, J., & Zhu, H. (2019). Automatic characterization of rock mass discontinuities using 3D point clouds. *Engineering Geology*, *259*, 105131.

Liu, Z. N., Liu, X. Q., Yang, L. J., Leo, D., & Zhao, H. W. (2018). An autonomous dock and battery swapping system for multirotor UAV. Unpublished, https://www. researchgate. net/publication/325077351, 10.

Loncke, L., Gaullier, V., Droz, L., Ducassou, E., Migeon, S., & Mascle, J. (2009). Multi-scale slope instabilities along the Nile deep-sea fan, Egyptian margin: A general overview. *Marine and Petroleum Geology*, *26*(5), 633-646.

Loke, M. H., & Barker, R. D. (1996). Rapid least-squares inversion of apparent resistivity pseudosections by a quasi-Newton method1. Geophysical prospecting, 44(1), 131-152.

Loke, M. H. (2000). RES2DINV version 3.44 for windows 95/98 and NT: rapid 2D resistivity and IP inversion using the least squares method. Adv. Geosci., Austin, TX.

Loke, M. H. (2001). Electrical imaging surveys for environmental and engineering studies. A practical guide to 2-D and 3-D surveys, RES2DINV Manual. IRIS Instruments. www. iris-instruments. com.

Loke, M. H., (2018). General Public License, RES2DINVx64 ver. 4,8.10 date 2-5-2018, Copyright (2018) M.H.Loke. Retrieved from https://www.geotomosoft.com/downloads.php Accessed on 18 September 2022

Luckman, B. H. (1977). The geomorphic activity of snow avalanches. *Geografiska Annaler: Series A, Physical Geography*, *59*(1-2), 31-48.

Ma Y, Soatto S, Kosecka J, Sastry SS (2012) *An invitation to 3-d vision: from images to geometric models, vol 26*. Springer, Berlin

Magri, O. (2006). A geological and geomorphological review of the Maltese Islands with special reference to the coastal zone. *Territoris*, *6*, 7-26.

Magri, O., Mantovani, M., Pasuto, A., & Soldati, M. (2008). Geomorphological investigation and monitoring of lateral spreading along the north-west coast of Malta. *Geografia Fisica e Dinamica Quaternaria*, *31*(2), 171-180.

Malyuta, D.; Brommer, C.; Hentzen, D.; Stastny, T.; Siegwart, R.; Brockers, R. Long-duration fully autonomous operation of rotorcraft unmanned aerial systems for remote-sensing data acquisition. J. Field Robot. 2020, 37, 137–157.

Mantovani, M., Devoto, S., Forte, E., Mocnik, A., Pasuto, A., Piacentini, D., & Soldati, M. (2013). A multidisciplinary approach for rock spreading and block sliding investigation in the north-western coast of Malta. *Landslides*, *10*(5), 611-622.

Mantovani, M., Devoto, S., Piacentini, D., Prampolini, M., Soldati, M., & Pasuto, A. (2016). Advanced SAR interferometric analysis to support geomorphological interpretation of slow-moving coastal landslides (Malta, Mediterranean Sea). Remote Sensing, 8(6), 443.

Martinez, A., & Byrnes, A. P. (2001). Modeling dielectric-constant values of geologic materials: An aid to ground-penetrating radar data collection and interpretation. *Current Research in Earth Sciences, 1-16.*

Martínez-Espejo Zaragoza, I., Caroti, G., Piemonte, A., Riedel, B., Tengen, D., & Niemeier, W. (2017). Structure from motion (SfM) processing of UAV images and combination with terrestrial laser scanning, applied for a 3D-documentation in a hazardous situation. *Geomatics, Natural Hazards and Risk, 8(2),* 1492-1504.

Martino S, Mazzanti P (2014) Integrating geomechanical surveys and remote sensing for sea cliff slope stability analysis: the Mt. Pucci case study (Italy). *Nat Hazards Earth Syst Sci* 14(4):831–848

Mateos, R. M., García-Moreno, I., Reichenbach, P., Herrera, G., Sarro, R., Rius, J., ... & Fiorucci, F. (2016). Calibration and validation of rockfall modelling at regional scale: application along a roadway in Mallorca (Spain) and organization of its management. Landslides, 13(4), 751-763.

Matsuoka, N. (2001). Solifluction rates, processes and landforms: a global review. *Earth-Science Reviews*, *55*(1-2), 107-134.

Matthew, N. S. (2015). Elements of electromagnetics*. Oxford University Press.*

Mátyás, P., & Máté, N. (2019). Brief history of uav development. *Repüléstudományi Közlemények,* 31(1), 155-166.

Meles, G. A., Van der Kruk, J., Greenhalgh, S. A., Ernst, J. R., Maurer, H., & Green, A. G. (2010). A new vector waveform inversion algorithm for simultaneous updating of conductivity and permittivity parameters from combination crosshole/borehole-to-surface GPR data. *IEEE Transactions on geoscience and remote sensing, 48(9),* 3391-3407.

Mellor, M. (1968). Avalanches. *US Army Materiel Command, Cold Regions Research & Engineering Laboratory.*

Menegoni N, Giordan D, Perotti C, Tannant DD (2019) Detection and geometric characterization of rock mass discontinuities using a 3D high-resolution digital outcrop model generated from RPAS imagery–Ormea rock slope, Italy. *Eng Geol* 252:145–163

Meyerhoff, S. B., Maxwell, R. M., Revil, A., Martin, J. B., Karaoulis, M., & Graham, W. D. (2014). Characterization of groundwater and surface water mixing in a semiconfined karst aquifer using time-lapse electrical resistivity tomography. *Water Resources Research, 50(3),* 2566-2585.

Mogili, U. R., & Deepak, B. B. V. L. (2018). Review on application of drone systems in precision agriculture. *Procedia computer science, 133*, 502-509.

Monteleone, S., & Sabatino, M. (2014). Hydrogeological hazards and weather events: triggering and evolution of shallow landslides. *International Soil and Water Conservation Research*, *2*(2), 23-29.

Morin, J., & Van Winkel, J. (1996). The effect of raindrop impact and sheet erosion on infiltration rate and crust formation. *Soil Science Society of America Journal*, *60*(4), 1223-1227.

Mücher, H., van Steijn, H., & Kwaad, F. (2018). Colluvial and mass wasting deposits. In *Interpretation of micromorphological features of soils and regoliths* (pp. 21-36). Elsevier.

Mulet-Forteza, C., Socias Salvá, A., Monserrat, S., & Amores, A. (2020). 80th anniversary of pure and applied geophysics: a bibliometric overview. *Pure and Applied Geophysics, 177(2),* 531-570.

Mussett, A. E., & Khan, M. A. (2000). Looking into the earth: an introduction to geological geophysics. *Cambridge University Press.*

Musset, A. E., & Khan, M. A. (2003). Esplorazione del sottosuolo. Una introduzione alla geofisica applicata. *Ed. Zanichelli,* 169-172.

Niu, G., Yang, Q., Gao, Y., & Pun, M. O. (2021). Vision-Based Autonomous Landing for Unmanned Aerial and Ground Vehicles Cooperative Systems. IEEE Robotics and Automation Letters, 7(3), 6234-6241.

Orlando, L., & Marchesi, E. (2001). Georadar as a tool to identify and characterise solid waste dump deposits. *Journal of applied geophysics, 48(3),* 163-174.

Panzera, F., D'Amico, S., Lotteri, A., Galea, P., & Lombardo, G. (2012). Seismic site response of unstable steep slope using noise measurements: the case study of Xemxija Bay area, Malta. *Natural Hazards and Earth System Sciences*, *12*(11), 3421-3431.

Panzera, F., D'Amico, S., Galea, P., Lombardo, G., Gallipoli, M. R., & Pace, S. (2013). Geophysical measurements for site response investigation: preliminary results on the island of Malta.

Parise, M. (2002). Landslide hazard zonation of slopes susceptible to rock falls and topples. *Natural Hazards and Earth System Sciences*, *2*(1/2), 37-49.

Parsekian, A. D., Claes, N., Singha, K., Minsley, B. J., Carr, B., Voytek, E., ... & Flinchum, B. (2017). Comparing measurement response and inverted results of electrical resistivity tomography instruments. *Journal of Environmental and Engineering Geophysics, 22(3),* 249-266.

Paskoff, R., & Sanlaville, P. (1978). Geomorphologic observations on Maltese archipelago coasts. *Z. Geomorph. NF,(22),* 310-328.

Pawlik, Ł., & Šamonil, P. (2018). Soil creep: the driving factors, evidence and significance for biogeomorphic and pedogenic domains and systems–a critical literature review. *Earth-Science Reviews*, *178*, 257-278.

Pedley, H. M., House, M. R., & Waugh, B. (1976). The geology of Malta and Gozo. *Proceedings of the Geologists' Association*, *87*(3), 325-341.

Pedley, H. M., House, M. R., & Waugh, B. (1978). The geology of the Pelagian block: the Maltese Islands. In *The ocean basins and margins* (pp. 417-433). Springer, Boston, MA.

Pedley, M., Clarke, M. H., & Galea, P. (2002). Limestone isles in a crystal sea. *The Geology of the Maltese Islands, Publishers Enterprises Group, Malta*.

Pedley M (2011) The Calabrian stage, pleistocene highstand in Malta: a new marker for unravelling the late neogene and quaternary history of the islands. *J Geol Soc 168(4):*913–926

Perrone, A., Lapenna, V., & Piscitelli, S. (2014). Electrical resistivity tomography technique for landslide investigation: A review. *Earth-Science Reviews, 135*, 65-82.

Persico, R. (2014). Introduction to ground penetrating radar: inverse scattering and data processing. *John Wiley & Sons.*

Persico, R., D'Amico, S., Matera, L., Colica, E., De Giorgio, C., Alescio, A., ... & Galea, P. (2019). GPR Investigations at St John's Co-Cathedral in Valletta. Near Surface Geophysics, 17(3-GPR in *Civil and Environmental Engineering: Recent Methodological Advances),* 213-229.

Peterson, E. B., Klein, M., & Stewart, R. L. (2015). Whitepaper on Structure from Motion (SfM) photogrammetry: constructing three dimensional models from photography. *US Department of the Interior Bureau of Reclamation Research and Development Office, USA.*

Petrucci, O., & Polemio, M. (2003). The use of historical data for the characterisation of multiple damaging hydrogeological events. *Natural Hazards and Earth System Sciences*, *3*(1/2), 17-30.

Petrucci, O., & Pasqua, A. A. (2008). The study of past damaging hydrogeological events for damage susceptibility zonation. *Natural Hazards and Earth System Sciences*, *8*(4), 881-892.

Pfeiffer, T. J., & Higgins, J. D. (1990). Rockfall hazard analysis using the Colorado rockfall simulation program. Transportation Research Record, (1288).

Pipan, M., Baradello, L., Forte, E., & Prizzon, A. (2000, April). GPR study of bedding planes, fractures, and cavities in limestone. In *Eighth International Conference on Ground Penetrating Radar (Vol. 4084, pp. 682-687). SPIE.*

Pix4Dcapture (2018). Retrieved from: https://www.pix4d.com/product/pix4dcapture. Accessed on 18 September 2022

Pix4Dmapper, (2021). Pix4D SA. www.pix4d.com. Accessed on 20 July 2021

Prasad, N. B. (1995). Landslides-Causes & Mitigation. *Centre for Water Resources Development, Kerala, India*, *21*, 48-54.

RadarTeam Prism2 ® user manual, version 2.7, retrieved from: https://www.radsys.lv/userfiles/files/prism2manual.pdf. Accessed on 18 September 2022.

Rădoane, M., & Rădoane, N. (2017). Gully erosion. In *Landform Dynamics and Evolution in Romania* (pp. 371-396). Springer, Cham.

Remondino F, Barazzetti L, Nex F, Scaioni M, Sarazzi D (2011) UAV photogrammetry for mapping and 3d modeling–current status and future perspectives. *Int Arch Photogramm Remote Sens Spatial Inf Sci* 38(1):C22

Rial, F. I., Lorenzo, H., Novo, A., & Pereira, M. (2011). Checking the signal stability in GPR systems and antennas. *IEEE Journal of Selected Topics in Applied Earth Observations and Remote Sensing, 4(4)*, 785-790.

Riwayat, A. I., Nazri, M. A. A., & Abidin, M. H. Z. (2018, April). Application of electrical resistivity method (ERM) in groundwater exploration. In *Journal of Physics: Conference Series* (Vol. 995, No. 1, p. 012094). IOP Publishing.

RocPro3D, version 5.7, retrieved from: http://www.rocpro3d.com/download_en.php. Accessed on 18 September 2022.

RocPro3D v. 5.7.7 User's guide - Copyright © 2020 ROCPRO3D, retrieved from: http://www.rocpro3d.com/help/en/Index.htm. Accessed on 18 September 2022.

Ruiz-Carulla, R.; Corominas, J.; Mavrouli, O. A Fractal Fragmentation Model for Rockfalls. Landslides 2017, 14, 875–889.

Sabatakakis, N., Depountis, N., & Vagenas, N. (2015). Evaluation of rockfall restitution coefficients. In Engineering Geology for Society and Territory-Volume 2 (pp. 2023-2026). Springer, Cham.

Said, G., & Schembri, J. (2010). Malta. In E.C.F. Bird (Eds.), Encyclopedia of the World's Coastal landforms – Volume 1 (pp. 751– 759). Dordrecht: Springer Science+Business Media B.V

Saponaro, A., Dipierro, G., Cannella, E., Panarese, A., Galiano, A. M., & Massaro, A. (2021). A UAV-GPR Fusion Approach for the Characterization of a Quarry Excavation Area in Falconara Albanese, Southern Italy. *Drones, 5(2), 40*.

Sarro, R., Mateos, R. M., García-Moreno, I., Herrera, G., Reichenbach, P., Laín, L., & Paredes, C. (2014). The Son Poc rockfall (Mallorca, Spain) on the 6th of March 2013: 3D simulation. Landslides, 11(3), 493-503.

Sarro, R., Mateos, R. M., García-Moreno, I., Herrera, G., Reichenbach, P., Laín, L., & Paredes, C. (2014). The Son Poc rockfall (Mallorca, Spain) on the 6th of March 2013: 3D simulation. Landslides, 11(3), 493-503.

Sarro, R., Riquelme, A., García-Davalillo, J. C., Mateos, R. M., Tomás, R., Pastor, J. L., ... & Herrera, G. (2018). Rockfall simulation based on UAV photogrammetry data obtained during an emergency declaration: Application at a cultural heritage site. Remote Sensing, 10(12), 1923.

Shukla, S. B., Chowksey, V. M., Prizomwala, S. P., Ukey, V. M., Bhatt, N. P., & Maurya, D. M. (2013). Internal sedimentary architecture and coastal dynamics as revealed by ground penetrating radar, Kachchh coast, western India. *Acta Geophysica, 61(5),* 1196-1210.

Scerri S (2019) Sedimentary evolution and resultant geological landscapes. In: Gauci R, Schembri JA (eds) Landscapes and landforms of the Maltese Islands. *Springer, Cham,* pp 31–47

Schenk, T. (2005). Introduction to photogrammetry. *The Ohio State University, Columbus*, *106*.

Schönemann, E., Becker, M., & Springer, T. (2011). A new approach for GNSS analysis in a multi-GNSS and multi-signal environment. *Journal of Geodetic Science, 1(3),* 204-214.

Schulz, W. H. (2007). Landslide susceptibility revealed by LIDAR imagery and historical records, Seattle, Washington. *Engineering Geology*, *89*(1-2), 67-87.

Schweizer, J., Bruce Jamieson, J., & Schneebeli, M. (2003). Snow avalanche formation. *Reviews of Geophysics*, *41*(4).

Shapiro, N. M., & Campillo, M. (2004). Emergence of broadband Rayleigh waves from correlations of the ambient seismic noise. *Geophysical Research Letters, 31(7).*

Sharma, P. V. (1985). Geophysical methods in geology.

Slaymaker, O. (1988). The distinctive attributes of debris torrents. *Hydrological Sciences Journal*, *33*(6), 567-573.

Soldovieri, F., Prisco, G., & Persico, R. (2008). Application of microwave tomography in hydrogeophysics: Some examples. *Vadose Zone Journal, 7(1),* 160-170.

Solla, M., Lorenzo, H., & Pérez-Gracia, V. (2016). Ground penetrating radar: Fundamentals, methodologies and applications in structures and infrastructure. *Non-Destructive Techniques for the Evaluation of Structures and Infrastructure, 11, 89.*

Spetsakis, M., & Aloimonos, J. Y. (1991). A multi-frame approach to visual motion perception. *International Journal of Computer Vision*, *6*(3), 245-255.

Steinbeck, L., Mester, A., Zimmermann, E., Klotzsche, A., & van Waasen, S. (2022). In situ time-zero correction for a ground penetrating radar monitoring system with 3000 antennas. *Measurement Science and Technology, 33(7),* 075904.

Sturzenegger, M., & Stead, D. (2009). Close-range terrestrial digital photogrammetry and terrestrial laser scanning for discontinuity characterization on rock cuts. *Engineering Geology*, *106*(3-4), 163-182.

Sudha, K., Israil, M., Mittal, S., & Rai, J. (2009). Soil characterization using electrical resistivity tomography and geotechnical investigations. *Journal of Applied Geophysics, 67(1),* 74-79.

Šulyová, j. v. d. (2021). Benefits and limitations of using UAVs in different areas with a focus on the environment.

Sunamura, T. (1992). Geomorphology of rocky coasts (Vol. 3). *Wiley.*

Syukri, M., Taib, A. M., & Fadhli, Z. (2021). Bedrock identification using resistivity method at campus II of Universitas Syiah Kuala, Banda Aceh. In *IOP Conference Series: Materials Science and Engineering* (Vol. 1087, No. 1, p. 012070). IOP Publishing.

Szeliski R. (2010). Computer vision: algorithms and applications. Springer, Berlin

Thiele ST, Grose L, Samsu A, Micklethwaite S, Vollgger SA, Cruden AR (2017) Rapid, semi-automatic fracture and contact mapping for point clouds, images and geophysical data. *Solid Earth Discuss.*

Trasviña-Moreno, C. A., Blasco, R., Marco, Á., Casas, R., & Trasviña-Castro, A. (2017). Unmanned aerial vehicle based wireless sensor network for marine-coastal environment monitoring. *Sensors, 17(3),* 460.

Trechmann, C. T. (1938). A Skeleton of Elk (Cervus alces) From Neasham Near Darlington. *Proceedings of the Yorkshire Geological Society*, *24*(2), 100-102.

Tso, C. H. M., Kuras, O., Wilkinson, P. B., Uhlemann, S., Chambers, J. E., Meldrum, P. I., ... & Binley, A. (2017). Improved characterisation and modelling of measurement errors in electrical resistivity tomography (ERT) surveys. *Journal of Applied Geophysics, 146,* 103-119.

Tsourlos, P., Ogilvy, R., Papazachos, C., & Meldrum, P. (2011). Measurement and inversion schemes for single borehole-to-surface electrical resistivity tomography surveys. *Journal of Geophysics and Engineering, 8(4),* 487.

Uhlenbrook, S., & Wenninger, J. (2006). Identification of flow pathways along hillslopes using electrical resistivity tomography (ERT). *Predictions in ungauged basins: promise and progress, 303*, 15-20.

Upreti, S., & Kumar, M. (2008, March). Perspectives of Global Positioning System (GPS) Applications. *In Seminar cum Workshop.*

Vallejo, L.E. 1977. Mechanics of the stability and development of the Great Lakes coastal bluffs. *Ph.D. dissertation, University of Wisconsin-Madison, Madison, Wisconsin*.

Van Westen, C. J., Castellanos, E., & Kuriakose, S. L. (2008). Spatial data for landslide susceptibility, hazard, and vulnerability assessment: An overview. *Engineering geology*, *102*(3-4), 112-131.

Varnes D.J. (1978). Slope movement types and processes. In: Schuster RL, Krizek RJ (eds) *Landslides analysis and control, special report 176*. National Academy of Science, Washington, DC, pp 11–33

Vella, A., Galea, P., & D'Amico, S. (2013). Site frequency response characterisation of the Maltese islands based on ambient noise H/V ratios. *Engineering Geology*, *163*, 89-100.

Vermeer, M. (2019). Geodesy: The science underneath.

Vessia, G., Parise, M., & Tromba, G. (2013). A strategy to address the task of seismic micro-zoning in landslide-prone areas. *Advances in Geosciences*, *35*, 23-35.

Villegas-González, P. A., Ramos-Cañón, A. M., González-Méndez, M., González-Salazar, R. E., & De Plaza-Solórzano, J. S. (2017). Territorial vulnerability assessment frame in Colombia: Disaster risk management. *International journal of disaster risk reduction*, *21*, 384-395.

Warren, J. (2010). Raindrops and bombs: The erosion process. *Oklahoma Cooperative Extension Service.*

Wenzel K, Rothermel M, Fritsch D, Haala N (2013) Image acquisition and model selection for multi-view stereo. *Int Arch Photogramm Remote Sens Spatial Inf Sci* 40:251–258

Westoby, M. J., Brasington, J., Glasser, N. F., Hambrey, M. J., & Reynolds, J. M. (2012). 'Structure-from-Motion'photogrammetry: A low-cost, effective tool for geoscience applications. *Geomorphology, 179*, 300-314.

Williams P. (2003). Dolines. In: Gunn J (ed) Encyclopedia of caves and karst science. *Routledge,* pp 304–310

Wu, C., (2011). VisualSFM: A visual structure from motion system. Retrieved from: http://ccwu.me/vsfm. Accessed on 18 September 2022.

Wu JH, Lin WK, Hu HT (2018) Post-failure simulations of a large slope failure using 3DEC: the Hsien-du-shan slope. *Eng Geol* 242:92–107

Xu, T., & McMechan, G. A. (1997). GPR attenuation and its numerical simulation in 2.5 dimensions. *Geophysics, 62(2),* 403-414.

Yelf, R. (2004). Where is true time zero? In Proceedings of the Tenth International Conference on Grounds Penetrating Radar, 2004. *GPR 2004.* (Vol. 1, pp. 279-282). IEEE.

Žabota, B., & Kobal, M. (2021). Accuracy assessment of uav-photogrammetric-derived products using PPK and GCPs in challenging terrains: In search of optimized rockfall mapping. Remote Sensing, 13(19), 3812.

Zanzi, L., Hojat, A., Ranjbar, H., Karimi-Nasab, S., Azadi, A., & Arosio, D. (2019). GPR measurements to detect major discontinuities at Cheshmeh-Shirdoosh limestone quarry, Iran. *Bulletin of Engineering Geology and the Environment, 78(2)*, 743-752.

Zambon, N., Johannsen, L. L., Strauss, P., Dostal, T., Zumr, D., Cochrane, T. A., & Klik, A. (2021). Splash erosion affected by initial soil moisture and surface conditions under simulated rainfall. *Catena*, *196*, 104827.

Zhou, W., Beck, B. F., & Adams, A. L. (2002). Effective electrode array in mapping karst hazards in electrical resistivity tomography. *Environmental geology, 42(8),* 922-928.

List of acronyms

AMSL	Above Mean Sea Level
ASV	Autonomous Surface Vehicle
AUV	Autonomous Underwater Vehicle
BC	Blue Clay
CS	Control Station
CV	Computer Vision
DEM	Digital Elevation Model
DGNSS	Differential Global Navigation Satellite System
DHE	Damaging Hydrogeological Event
DOM	Digital Outcrop Model
DSM	Digital Surface Model
DSS	Decision Support System
DTM	Digital Terrain Model
EM	Electromagnetic
ERI	Electrical Resistivity Imaging
ERT	Electrical Resistivity Tomography
ESC	Electronic Speed Control
FAA	Federal Aviation Administration
FC	Flight Controller
GCP	Ground Control Point
GHz	GigaHertz
GIS	Geographic Information System
GL	Globigerina Limestone
GMES	Global Monitoring for Environment and Security
GNSS	Global Navigation Satellite System
GPR	Ground Penetrating Radar
GPS	Global Positioning System

GS	Greensand
GSD	Ground Sample Distance
H/V	Horizontal to Vertical
HVSR	Horizontal to Vertical Spectral Ratio
IMU	Inertial Measurement Unit
LCL	Lower Coralline Limestone
MASW	Multichannel Analysis of Surface Waves
MHz	MegaHertz
MVS	Multi-View Stereo Reconstruction
NDVI	Normalized Difference Vegetation Index
PBs	Pocket beaches
RC	Radio Control System
RGB	Red Green Blue spectral bands
RMSE	Root Mean Square Error
ROV	Remotely Operated Vehicle
SAR	Synthetic Aperture Radar
SDI	Spatial Data Infrastructure
SFM	Structure-From-Motion
TLS	Terrestrial Laser Scanning
TWT	Two Way Travel Time
UAV	Unmanned Aerial Vehicle
UCL	Upper Coraline Limestone
USV	Unmanned Surface Vehicle